INFORMATION TO USERS

This manuscript has been reproduced from the microfilm master. UMI films the text directly from the original or copy submitted. Thus, some thesis and dissertation copies are in typewriter face, while others may be from any type of computer printer.

The quality of this reproduction is dependent upon the quality of the copy submitted. Broken or indistinct print, colored or poor quality illustrations and photographs, print bleedthrough, substandard margins, and improper alignment can adversely affect reproduction.

In the unlikely event that the author did not send UMI a complete manuscript and there are missing pages, these will be noted. Also, if unauthorized copyright material had to be removed, a note will indicate the deletion.

Oversize materials (e.g., maps, drawings, charts) are reproduced by sectioning the original, beginning at the upper left-hand corner and continuing from left to right in equal sections with small overlaps. Each original is also photographed in one exposure and is included in reduced form at the back of the book.

Photographs included in the original manuscript have been reproduced xerographically in this copy. Higher quality 6" x 9" black and white photographic prints are available for any photographs or illustrations appearing in this copy for an additional charge. Contact UMI directly to order.

UMI

A Bell & Howell Information Company
300 North Zeeb Road, Ann Arbor MI 48106-1346 USA
313/761-4700 800/521-0600

COMPOSITIONAL ORDER AND STRUCTURE OF EPITAXIAL THIN FILM SEMICONDUCTORS BY X-RAY DIFFRACTION

BY

KEVIN LLOYD WHITEAKER

B.S., Oregon State University, 1991
M.S., University of Illinois at Urbana-Champaign, 1993

THESIS

Submitted in partial fulfillment of the requirements
for the degree of Doctor of Philosophy in Physics
in the Graduate College of the
University of Illinois at Urbana-Champaign, 1997

Urbana, Illinois

UMI Number: 9812807

UMI Microform 9812807
Copyright 1998, by UMI Company. All rights reserved.

This microform edition is protected against unauthorized
copying under Title 17, United States Code.

UMI
300 North Zeeb Road
Ann Arbor, MI 48103

© Copyright by Kevin Lloyd Whiteaker, 1997

UNIVERSITY OF ILLINOIS AT URBANA-CHAMPAIGN

THE GRADUATE COLLEGE

JULY 1997
(date)

WE HEREBY RECOMMEND THAT THE THESIS BY

KEVIN LLOYD WHITEAKER

ENTITLED COMPOSITIONAL ORDER AND STRUCTURE OF EPITAXIAL THIN FILM SEMICONDUCTORS BY X-RAY DIFFRACTION

BE ACCEPTED IN PARTIAL FULFILLMENT OF THE REQUIREMENTS FOR

THE DEGREE OF DOCTOR OF PHILOSOPHY

Director of Thesis Research

Head of Department

Committee on Final Examination†

Chairperson

† Required for doctor's degree but not for master's.

0-517

COMPOSITIONAL ORDER AND STRUCTURE OF EPITAXIAL THIN FILM SEMICONDUCTORS BY X-RAY DIFFRACTION

Kevin Lloyd Whiteaker, Ph.D.
Department of Physics
University of Illinois at Urbana-Champaign, 1997
Ian K. Robinson, Advisor

Here two experiments using x-ray diffraction on thin films grown by molecular beam epitaxy are described. One concerns the compositional ordering of $Si_xGe_{1-x}(001)$ alloy films. The other reports the defect cubic structure of epitaxial Fe_xSi films on Si(111). The thesis also describes our newly assembled surface x-ray diffractometer and vacuum chamber, used in one of the experiments, and the calculation of the integrated intensity of surface rod θ-scans, to give the Lorentz factor used for the data reduction to structure factors.

Understanding compositional long range order in $Si_{1-x}Ge_x(001)$ films is an important problem in the molecular beam epitaxial growth of semiconductor alloys, for which a background of the bulk SiGe alloy and its film growth conditions is presented. Previous experiments pointed to the growth surface as the focus, for which two ordering mechanisms have been proposed to explain the evidence so far. Both are directly related to the known (2×1) reconstruction at the growth surface. We therefore performed surface x-ray diffraction experiments on $Si_{0.5}Ge_{0.5}$ films grown on Ge(001) substrates. The results for our thinnest film (8 monolayers) show the compositional order at the initial stages of growth. This ordering is observed underneath the surface (2×1) dimer reconstruction, and was previously predicted by calculations on the equilibrium alloy surface. This initial surface compositional ordering is also consistent with the ultimate structure for the bulk of these films. Measurements from thicker alloy films show an increase in the average order parameter with increasing thickness, but then a decrease with the thickest film of 1000 Å.

X-ray diffraction also has been used to analyze a series of thin film samples of Fe_xSi grown by MBE as a function of thickness and the composition variable, x. Unannealed samples

were found to be composed entirely of CsCl-type structure not present in the bulk phase diagram. A careful crystallographic analysis was used to show that the variable composition is accommodated by vacancies on the Fe sites. The unit cells of the film were nearly lattice-matched to the substrate, which results in a rhombohedral distortion; this lateral strain is compressive for samples near FeSi composition and tensile for samples near $Fe_{0.5}Si$ composition.

Acknowledgments

I would like to express my deepest gratitude to Professor Ian K. Robinson, my thesis advisor and mentor. I have benefited greatly from his scientific expertise and intellect. Prof. Robinson is a generous and fair person, and I have very much enjoyed working with him. Part of the credit for success of the experiments present in this thesis goes to Prof. Robinson. I also wish to thank Prof. Robinson for his support, encouragement, and confidence. My fellow graduate students in Prof. Robinson's groups also have provided intellectual and moral support. Yong Chu, Don Walko, David Fanning, Chinkyo Kim, and John Pitney, all have been great help and good friends.

I also wish to thank Professor David Cahill. His expertise on the growth and morphologies of SiGe thin film was very important. Our discussion were always of value and helped in the intellectual development of this thesis. Prof. Cahill's support of the experiments, the Silicon MBE chamber, and the overall support of the Epi Center was essential. One of Prof. Cahill's students, Joseph Van Nostrand, was another important person in the SiGe experiments. I am very thankful to Joe for his time and efforts in preparing several of the thin film samples, and then training me to operate the MBE chamber to prepare my own samples. Joe's expertise was very important in the technical details of growth processes and operations of the equipment. Dr. Van Nostrand also provide additional analysis of the SiGe films by STM.

Doug Jeffers is another expert in the Epi Center who helped me many times. As the

Technician, Coordinator, Vacuum Engineer and Safety Officer for the Epi Center. Doug has many responsibilities and also deserves some credit the my experiment's success and many others in the Epi Center. Without the excellent condition and operation of the UHV transfer systems, I could not have done my experiments. Doug also helped with the maintenance of both the x-ray analysis and Silicon MBE chambers. I enjoyed learning many of hands-on details and tricks of UHV equipment from Doug.

Curtis Benson, a former fellow graduate student with Prof. Robinson, was another person who help in the assembly of the x-ray diffractometer and analysis chamber. The best example of his contribution is the ingenious motorized screw jack system inside the diffractometer for the vertical stage motion, critical for the transfer of samples in and out of the x-ray chamber. Curtis also designed and assembly the separated stage for the rotating anode and its pumping system. He also assembled the monochromator stage and did some the initial characterization of the focusing HO graphite monochromator. The credit for success of the instrument must go partly to Curtis, beside Ian for its overall design. Curtis was also performed some of the initial experiments for iron silicide chapter.

Another important colleague (fellow graduate student) and friend is Kenneth Ritley. His many discussions, his extra hands, and his expertise on MBE were a great help to me and the SiGe experiments. I enjoyed all our lively discussion in the Epi Center. Ken was the leader in the community within the Epi Center graduate students. Ken worked with me in preparing refractory metal thin film samples for preliminary experiments. Although not documented in this thesis, these experiments were successful and is now continuing with another student in Prof. Robinson's group, John Pitney.

I also must acknowledge several other fellow graduate students here at the University of Illinois. Osman Gurdal, a student of Joe Greene group, provided several Ge(001) sample for initial experiments using the x-ray instrument. This work and further cooperation in the Epi Center was a great help. Another fellow student inside the Epi Center, Zhonghui

Wang, provided XPS analysis of one SiGe sample. Richard D. Aburano provided many intellectual discussions and encouragement, as a fellow x-ray experimenter. Richard also provided a C_{60}/Ge(001) (2×1) interface sample, which was a great help in the initial experiments/adjustments of the new x-ray instrument.

There are a number of other individuals that I have learned from, whom held post-doctoral position with Prof. Robinson. Dr. Detlef M. Smilgies performed some initial experiments on the iron silicide films. Dr. Peter J. Eng and Dr. Rölf Schuster were helpful in techniques of diffraction and surface science, as well as the operations at the NSLS. Dr. Jeff L. Libbert also was helpful in discussions of diffraction and x-ray generators.

Additional thanks goes to Dr. H. von Känel and Dr. Nico Onda for the providing the iron silicide thin film samples. Another thanks goes to Prof. T. C. Chiang for his discussion on these experiments, as well as the collaboration with his student R. Aburano. I wish to thank professors Peter Flynn, Joe Greene, and Angus Rockett for their support of Epi Center and the collaborations with their respective students, K. Ritley, O. Gurdal, and Z. Wang.

This work not have been possible without the support, encouragement, and understanding of my wife, Mikka.

I acknowledge the support from the U. S. Department of Education and its Graduate Assistances in Area of National Need (GAANN) Fellowship awarded through the University of Illinois, Department of Physics, under contact No. DE-P200-A40532. I also acknowledge the support from the U. S. Department of Energy under contract No. DEFG02-96ER45439 to the Materials Research Laboratory. The National Synchrotron Light Source is supported by Department of Energy, contract No. DE-AC012-76CH00016.

Table of Contents

Chapter

1 Introduction 1

1.1 X-ray Diffraction 1

1.1.1 Background and 3D diffraction 1

1.1.2 2D and surface x-ray diffraction 5

1.2 Si_xGe_{1-x}: Background and Motivation 8

1.2.1 The Bulk and Thermodynamics 10

1.2.2 Compositional Ordered Structures 11

1.2.3 Growth Surface and Conditions. 13

1.2.4 Proposed Mechanisms 15

2 Experimental Methods 20

2.1 Introduction 20

2.2 Surface X-ray Diffractometer 21

2.3 Diffractometer Alignment 26

2.4 Integrated Intensity Calculation 30

2.4.1 Introduction 30

2.4.2 Integrated Intensity 31

2.4.3 Integrations 33

2.4.4 Results 41

2.4.5 Discussion 41

2.5 Second harmonic correction 46

3 SiGe alloy surface and thin films 49

3.1 Introduction 49

3.2 Experiment 50

3.2.1 Sample Growth 51

3.2.2 X-ray diffraction measurements 52

3.3 Results 56

3.3.1 Ge(001) buffer layer surface 56

3.3.2 $Si_{0.5}Ge_{0.5}(001)$ very thin film 61

3.3.3 Electron Density and Difference Map 65

3.3.4 Thicker alloy films and their degree of order 69

3.4 Conclusion 75

4 Disordered Structure of Cubic Iron Silicide Films on Si(111) 78

4.1 Introduction 78

4.2 Method 81

4.3 Crystal Symmetry of the Films 82

4.4 Structure Factors 84

4.5 Strain 89

4.6 Thickness and Uniformity of the Films 93

4.7 Conclusions 94

References 99

Vita 103

List of Tables

2.1 Incident and exit beam parameters for Lorentz factor plot 45

3.1 Atomic positions for models to Ge(001) 2×1 reconstruction 60

3.2 Dimer bond parameters 60

3.3 Average film order parameters of $Si_{0.5}Ge_{0.5}(001)$ versus thickness 73

3.4 Average film order parameters of $Si_{0.5}Ge_{0.5}(001)$ versus temperature 74

4.1 List of results for Fe_xSi thin films 90

List of Figures

1.1 STM image of example Si(001) (2×1) reconstructed surface 9

1.2 $Si_{0.5}Ge_{0.5}$ compositional order structure RS2 12

1.3 Proposed ordering mechanism by LeGoues *et al.* 16

1.4 Proposed growth and ordering mechanism by Jesson *et al.* 18

2.1 Photograph of x-ray diffractometer and UHV analysis chamber 22

2.2 Floor sketch of the Epi Center laboratory 23

2.3 Surface x-ray diffractometer 24

2.4 Horizontal view of monochromator's focusing x-ray optics 28

2.5 Real space divergence and acceptance angle variables for integrated intensity calculation 34

2.6 Orthogonal coordinate frames of the diffractometer 35

2.7 Lorentz factor plot along three Ge(001) (2×1) surface diffraction rods 43

2.8 Polarization factor plot along three Ge(001) (2×1) surface diffraction rods . 44

2.9 Detector discrimination of primary and second harmonic x-rays 47

3.1 Reciprocal space of Si_xGe_{1-x} 54

3.2 Measured Ge(001) structure factors and model comparisons 57

3.3 Structural model of Ge(001) (2×1) reconstruction 59

3.4 $Si_{0.5}Ge_{0.5}$ 8 ML film data compared to Ge(001) 62

3.5 $Si_{0.5}Ge_{0.5}$ 8 ML film data compared to model fit 63

3.6 Model of $Si_{0.5}Ge_{0.5}(001)$ 8 ML thick film structure 66

3.7 Electron density map of Ge(001) (2×1) 68

3.8 Electron difference density map of $Si_{0.5}Ge_{0.5}(001)$ (2×1) 70

3.9 Rods ($\frac{1}{2}1L$) for various films $Si_{0.5}Ge_{0.5}(001)$ of increasing thickness 71

4.1 Related cubic structures 79

4.2 Structure Factors of 1:1 composition film 85

4.3 Structure Factors of 1:2 composition film 86

4.4 Rhombohedral distortion of silicide films vs. film thickness 92

4.5 Thin film Bragg peak 95

4.6 Fe_xSi (CsCl) structures 97

Chapter 1

Introduction

1.1 X-ray Diffraction

1.1.1 Background and 3D diffraction

X-rays are electromagnetic radiation with a wavelength near 1 Å. This makes x-rays an excellent probe of the structure of matter in its variety of forms. The reason being that the spacings between the elemental parts of matter, atoms, are also on the order of the wavelength of x-rays. Therefore, diffraction by these electromagnetic waves has become an important tool for determining the structure of materials. Here, I will present a brief outline of x-ray scattering and diffraction, leading to a discussion of surface x-ray diffraction. Further detail on this subject can be found in Ref. [1]

The elastic x-ray scattering amplitude from an single classical electron by an incident wave A_o is given by the Thompson scattering equation,

$$A = A_o \frac{e^2}{mc^2 R} \,. \tag{1.1}$$

This is for the scattering of x-rays polarized perpendicular to the plane of scattering, and R is the distance to the detector. For the opposite polarization there is an additional factor of

$\cos\theta$, the scattering angle. The detected quantity is the intensity, which is the time averaged squared magnitude of the wave-field amplitude, which gives

$$I = I_o \frac{e^4}{m^2 c^4 R^2} P(\theta) \ . \tag{1.2}$$

The factor $P(\theta)$ is the polarization factor from the average over both polarizations, which for a random polarization source, becomes $(1+\cos^2\theta)/2$. Beyond here, this term will be ignored. The second term is usually combined to $(r_e/R)^2$ where r_e is the classical radius of an electron.

For a solid, which has many electrons within it, the total x-ray scattering is the superposition of all the waves scattered by each electron. The interference between these waves is determined by the position and/or arrangement of the electrons, which is related by the phase of each wave. The equation for the scattered amplitude is then,

$$A = \sum_n A_o \left(\frac{r_e}{R}\right) e^{i\vec{q}\cdot\vec{r}_n} \ , \tag{1.3}$$

where $\vec{q} = \vec{k}_f - \vec{k}_i$ defines the momentum transfer between the final scattered and incident wavevectors. This sum over all electrons is then broken down into the periodic and repeating units of the solid. First, are all the electrons within each atom. Second, each atom within the unit cell volume is added. The unit cell can be defined as having the minimum number of independent atoms (in the solid) and is repeated in all 3 dimensions of space to fill the volume taken by the solid. A solid with this specific periodic structure of a unit cell is defined as a crystal. The position for each electron can then be written as

$$\vec{r}_n = \vec{r}_Z + \vec{r}_i + \vec{R}_j \ . \tag{1.4}$$

The summation is also broken into these parts is give for the scattering amplitude

$$A = A_o\left(\frac{r_e}{R}\right) \sum_j \sum_i \sum_Z e^{i\vec{q}\cdot(\vec{r}_Z + \vec{r}_i + \vec{R}_j)} \ , \tag{1.5}$$

where the first sum is over the Z electrons in an atom, the next sum j is over the atoms in the unit cell, and the final summation is over all space. The first sum, Z, can be grouped together to give what is called the atomic scattering factor

$$f(\vec{q}) = \sum_{Z} e^{i\vec{q}\cdot\vec{r}_Z} \ . \tag{1.6}$$

Here the classical approach can no longer be used, but the quantum mechanical scattering is used to calculate resulting atomic scattering factors. The quantum mechanical scattering is covered in Sakurai [2], while the conventional analytic formulae for the scattering factors are found in Ref. [3].

Next, in the Equation (1.5), is the sum over the atoms within the unit cell, which can be grouped as

$$F(\vec{q}) = \sum_{i} f_i(\vec{q}) e^{i\vec{q}\cdot\vec{r}_i} \ . \tag{1.7}$$

Here f_i is the atomic scattering factor for the i atom at position $\vec{r}_i$. This result for the unit cell is called the structure factor. Alternatively, the structure factor function is viewed as the Fourier transformation of the electron density within the unit cell.

The new equation for the scattering amplitude is then

$$A = A_o \left(\frac{r_e}{R}\right) F(\vec{q}) \sum_{j} e^{i\vec{q}\cdot\vec{R}_j} \ , \tag{1.8}$$

where the summation over full volume of the crystal is in units of direction given by the bases vectors of the unit cell, $\vec{a}_1$, $\vec{a}_2$, and $\vec{a}_3$, giving

$$\vec{R} = n_1\vec{a}_1 + n_2\vec{a}_2 + n_3\vec{a}_3 \ . \tag{1.9}$$

The n's are integers from 0 to N, where Na_1 is the size of the crystal in the corresponding basis direction. The summation is then distributed in the three directions to give

$$\sum_{n_1,n_2,n_3} e^{i\vec{q}\cdot(n_1\vec{a}_1+n_2\vec{a}_2+n_3\vec{a}_3)} = \sum_{n_1} e^{in_1\vec{q}\cdot\vec{a}_1} \sum_{n_2} e^{in_2\vec{q}\cdot\vec{a}_2} \sum_{n_3} e^{in_3\vec{q}\cdot\vec{a}_3} \ . \tag{1.10}$$

This brings one to introduce the bases for $\vec{q}$, called reciprocal space, where

$$\vec{q} = h\vec{b}_1 + k\vec{b}_2 + l\vec{b}_3 \tag{1.11}$$

where

$$\vec{b}_1 = 2\pi \frac{\vec{a}_2 \times \vec{a}_3}{\vec{a}_1 \cdot \vec{a}_2 \times \vec{a}_3}, \text{ etc.} \tag{1.12}$$

so that

$$\vec{q} \cdot \vec{a}_1 = 2\pi h \tag{1.13}$$

$$\vec{q} \cdot \vec{a}_2 = 2\pi k \tag{1.14}$$

$$\vec{q} \cdot \vec{a}_3 = 2\pi l \tag{1.15}$$

These are called the Laue conditions. More details of reciprocal space and it relationship the physical periodic space of real crystals is covered in Ref. [1] and [4]. The variables h, k, and l at integer positions correspond to the Miller indices, which describe the vectors normal to planes of atoms within the crystal. (These planes and their separation d_{hkl} are the same used in the alternative derivation of x-ray diffraction to give Bragg's Law, $2d_{hkl}\sin\theta = \lambda$.) The summation, for example of n_1, becomes

$$\left| \sum_{n_1=0}^{N_1} e^{2\pi i h n_1} \right|^2 = \left| \frac{1 - e^{2\pi i h N_1}}{1 - e^{2\pi i h}} \right|^2 = S_{N_1}(h) \tag{1.16}$$

which is a δ-like function as $N \to \infty$ at integer values of h when squared for the intensity.

The intensity becomes

$$I = I_o \left(\frac{r_e}{R}\right)^2 |F(hkl)|^2 S_{N_1}(h) S_{N_2}(k) S_{N_3}(l) \tag{1.17}$$

which gives the result that the diffraction is concentrated at points in reciprocal space where hkl are integers. These points are often called Bragg peaks. The angles of these beams of diffracted x-rays are determined by the relationship between hkl to $\vec{q}$ which is defined in terms of the final wavevector. The final intensity result above can be also viewed the Fourier

transformation for the whole crystal, which the crystal well defined periodicity results in sharply defined peaks in reciprocal space. The structure factors $F(h,k,l)$ relate the strength of these peaks to each other. By measuring the strength of the Bragg peaks, and quantifying the structure factor from a material of interest, its atomic structure within the unit cell can be determined. The intensity in the form above is not as useful in these measurement for reasons to be discussed in Chapter 2. The experiments measure the quantity (integrated intensities), which is the angular and volume integration in reciprocal space. This results in the equation [1]

$$I_{int} = I_o r_e^2 \frac{\lambda^3 V}{\omega v_a^2 \sin 2\theta} |F(h,k,l)|^2 \ . \qquad (1.18)$$

The experimental parameters are: V, the crystal volume; ω, the angular speed of integration; v_a, the unit cell volume; and $\sin 2\theta$ is called the Lorentz factor (to be discussed in Chapter 2).

One final detail is that once the structure factors are measured, the inverse transformation to the atomic structure is not directly possible because one lacks the structure factors' complex phases. This is called the phase problem, and is usually solve by the indirect method of least squares refinement to a proposed model. The atoms and/or their positions are then parameters to calculated model structure factors, which are then compared to the measured structure factor by the χ^2 distribution function,

$$\chi^2 = \frac{1}{N-p} \sum_{i=1}^{N} \frac{\left|F_i - F_i^{model}\right|^2}{\sigma^2} \ . \qquad (1.19)$$

The measurement uncertainties, σ, and the number of parameters, p, are normalization factors of the refinement to the N data points.

1.1.2 2D and surface x-ray diffraction

This thesis focuses on experiments on surfaces and thin films of crystalline materials. The x-ray diffraction from these structures are based on the same principles as 3D diffraction, but a number of details and assumptions change. This leads to different forms of intensities,

instead of just Bragg peaks. For example, the surface can be viewed as a defect of a crystal, where the periodicity is stopped in one direction . This boundary, or sharp discontinuity, will cause the Fourier transformation to give a continuous distribution of diffraction intensity. This distribution, in reciprocal space, is perpendicular to the surface, i.e. in the stopped direction of periodicity.

Another example is an ideal 2D crystal. Here there is no periodicity in the third direction. A similar unit cell can be defined for the 2D crystal, but it will now have only two basis vectors. The summation over all space will be distributed in only two directions. Reciprocal space is still in 3-dimensions, so a third real space direction is freely defined to be perpendicular to 2D plane. The reciprocal space bases directions are then; h and k are in the 2D plane and l is perpendicular, out of plane. The intensity result is [5]

$$I = I_o \left(\frac{r_e}{R}\right)^2 |F(hkl)|^2 S_{N_1}(h) S_{N_2}(k) \,, \tag{1.20}$$

which does not have a Laue condition in l. With respect to this direction, the only dependence is in the structure factor function, which is a continuous function because it is defined for a single unit cell. In the other two directions the h and k Laue conditions still apply because of the 2D periodicity. The resulting intensity pattern is in the form of rods, periodic with δ-functions at integer position in variables h and k, but continuous in l.

Returning to a real crystal surface, one way to derive the diffraction result is to use the 2D result above to build a crystal in one half-space. The perpendicular summation can then be written as

$$\sum_{n_3=0}^{-\infty} e^{2\pi i l n_3} = \frac{1}{1 - e^{-i2\pi l}} \,, \tag{1.21}$$

which squared for the intensity becomes,

$$I_{CTR} = I_o \left(\frac{r_e}{R}\right)^2 |F(hkl)|^2 S_{N_1}(h) S_{N_2}(k) \frac{1}{2\sin^2(\frac{2\pi l}{2})} \,. \tag{1.22}$$

The $1/\sin^2$ function still gives a continuous line of diffraction intensity, but now the function is peaked again at integer values of l. This result gives what are called crystal

truncation rods (CTR) which are rods of intensity which decay as $1/q^2$ away from the Bragg peaks in the direction perpendicular to the surface [7, 6]. This result is for the simplest ideally terminated crystal, but in general the distribution of intensity along the CTR is determined by the surface structure. Details such as roughness, vacuum relaxations, absorption, desorption and electro-chemical reactions and/or changes at surface will affect the CTR distribution and are used to determine these changes in surface structure. [5, 8, 9, 10]

Another example in patterns of surface x-ray diffraction is from crystal surfaces with reconstructions. In general, a surface reconstruction is the re-organization of atoms to a different structure from that of the bulk [11]. It is typically associated with the surface structure having a different periodicity from the substrate crystal. This is analogous to having a separate 2D crystal lying atop the surface of ideally terminated crystal. The pattern of diffraction intensity is a combination of surface rods from the reconstruction and CTR's. This will be the case for our experiments on Ge and Si_xGe_{1-x} (001) surfaces, which have the dimer reconstruction and is double the periodicity of the substrate in one direction. In reciprocal space, this results in rods at half the distance between the CTR's along that direction. The notation describing the reconstruction periodicity is to use integer multiples of the substrate's surface units. For example, the Ge(001) dimer reconstruction is represented as (2×1).

The last example is the diffraction of thin films. A thin film has two surfaces which can give complex distributions along rods from the interference of scattered waves. As will be seen in Chapter 4, the summation (Equation 4.4), similar to the ones above, in a direction perpendicular to the film interface, results in a function which oscillates in intensity. This oscillation is then related to the length scale or thickness of the thin film.

To conclude this section, x-ray diffraction is a powerful tool for determining the atomic structure of materials, surfaces, and thin films. The weak Thompson scattering from the

electrons makes the calculation and interpretation of x-ray diffraction patterns easier than most other diffraction tools. Besides the kinematical process, another advantage is that the x-ray diffraction measurements are an average over sample volume or surface. Very dilute and random defects or structures in a sample will scatter weakly, and not effect the accumulative average microscopic picture of the atomic structure.

1.2 Si_xGe_{1-x}: Background and Motivation

Molecular beam epitaxy (MBE) is an important technique for the growth of novel thin film materials and structures. With the MBE growth technique there is an interface between the environment of incoming species for growth and the growing crystal film. The interface is not in thermal equilibrium, but is instead a driven system, driven by the growth process. The resulting film material and its structure depends on a number of growth conditions. The substrate temperature, film thickness, vicinal (miscut angle), and flux rate are examples of parameters which affect the resulting crystal film and therefore, need so to be understood.

Another important growth condition is the structure of the interface. The interface can have reconstructions of surface atoms which can then affect the crystal film growth. Silicon and Germanium (001) surfaces, including their alloy, have the dimer (2×1) reconstruction. This reconstruction is believed to cause the growth of compositionally ordered films of SiGe(001). Figure 1.1 pictures an example of the Si(001) surface and its reconstruction of dimers in form of rows.

SiGe alloy films were at first assumed to be the same as the bulk solid, a completely random solid solution of both elements with the diamond structure. Then Ourmazd and Bean [12] among others [13, 14] found additional Bragg peaks in electron diffraction patterns of alloy layers within Si_xGe_{1-x}/Si(001) super-lattices. Pictures of transmission electron diffraction (TED) patterns show additional peaks at $(\frac{1}{2},\frac{1}{2},\frac{1}{2})$ positions. Meaning there is some

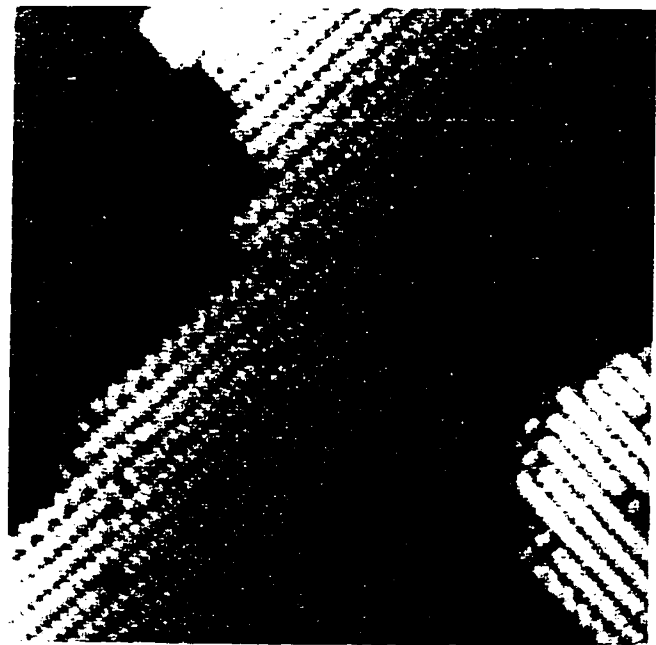

Figure 1.1: Scanning tunneling microscopy image of example Si(001) (2×1) reconstructed surface. Courtesy of D. Cahill

structure with double the bulk's cubic periodicity along the ⟨111⟩ directions. These weak superstructure peaks are due to compositional correlations of the SiGe alloy. This correlation (or ordering) of Si and Ge atoms on the diamond lattice sites has gained considerable attention, since the material's adjustable band gap is of technological importance. The ordering of SiGe is the focus of this section and, in Chapter 3, the experiments performed to detail this structure.

Compositional ordering in semiconductor alloys has also been observed in other material systems besides Si_xGe_{1-x}. This phenomena also occurs within III-V isovalent pseudobinary alloys, $A_{1-x}B_xC$. In some alloys the ordered structure is believed to be a thermodynamically stable phase, namely the chalcopyrite structure [15]. In other systems, with the best studied example being $Ga_{0.5}In_{0.5}P(001)$, the ordering is the CuPt-type structure where the superstructure is along (111) planes [1] . Similar to what will be discussed below for $Si_xGe_{1-x}(001)$,

[1]See Ref. [16], and listed references within it, for a review of compositional order in III-V semiconductor alloys.

the $Ga_{0.5}In_{0.5}P(001)$ ordering is believed to be a meta-stable structure which is stabilized by a ordering within the surface reconstruction during growth by MBE or organometallic vapor-phase epitaxy (OMVPE) [16, 17].

The rest of this section will detail the compositional order in Si_xGe_{1-x}. A review of the thermodynamic and the details of the known meta-stable structure will be presented. The growth conditions needed for ordering is also detailed, and finally, two proposed mechanism will be described.

1.2.1 The Bulk and Thermodynamics

To understand the solids formed by the combination of silicon and germanium, as well as other Group IV elements, one must look at the bulk thermodynamics. That is, the free energy difference between proposed ordered or disordered structures and the separate elements (phase separation) needs to be calculated. This energy difference can be written out in terms as

$$\Delta H = E_{VD}(a_0) + E_{elect}(\alpha) + E_{relax}(\alpha) - T \cdot \sigma \tag{1.23}$$

The first term describes the *volume deformation* energy needed to first expand and then contract the diamond lattices for the smaller and larger species, respectively, for the combined solid with lattice spacing a_0. This elastic term is always positive because both element solids are deformed from equilibrium. With C/Ge and Ge/Sn, this term, and possible positive second term, cannot be overcome and results in phase separation for these compounds. The second term is the *electronic* energy which can include the formation of chemical bonds and the band structure. This term can be negative, as with SiC which forms chemical bonds, or it can be positive. Martins and Zunger have calculated such a small positive bonding energy for Si and Ge [18]. The third term describes the local elastic *relaxations*, which depends on the ordering α, with the diamond lattice. Certain ordered structures can have large relaxation of the bonds between the different species. An example is the zinc blende

structure and its familiar form in GaAs. This cubic structure also occurs for SiC and has been calculated to its lowest energy phase [18, 19]. For SiGe, no bulk ordered phases have been observed[19]. The relaxation term is also important in disordered solids, but it will be higher than a long range ordered solid because of statistical deviations from the average composition and structure. The last term in the energy difference equation is entropy, σ. The negative entropy term is the main reason for the existence of the bulk solid solution formed for alloys of Si and Ge.

For SiGe the small chemical bonding contribution leaves the elastic arguments to predict a structure. This leads to two structures; the zinc blende and the rhombohedral (labeled RS1). In both, the structural degrees of freedom allow them to be intrinsically strain free. All bonds are exactly tetrahedral and bond lengths can be any value. While the zinc blende is an fcc ordered structure, the RS1 has alternating Si/Ge within the (111) double layers noted by (...SiGe-GeSi-SiGe...). This was the initially proposed structure to explain the observed superstructure peaks in the TED patterns [12]. Although the RS1 structure has ordering in only one [111] direction, the (001) surface has four equivalent $\langle 111 \rangle$ directions and so four rotational domains are also proposed to explain all the observed $(\frac{1}{2},\frac{1}{2},\frac{1}{2})$ peaks. As promising as RS1 may be, calculations indicate the disorder-order transition for this structure occurs below room temperature, and therefore, it is kinetically unachievable [18, 20]. This is the case for bulk SiGe where annealing for long periods have not achieved any ordered structures [19].

1.2.2 Compositional Ordered Structures

Other structures that are consistent with the electron diffraction images are discussed next. Another rhombohedral structure (labeled RS2) has the opposite ordering within the (111) double layers, with a sequence of ...SiSi-GeGe-SiSi-GeGe.... This structure is shown in Figure 1.2. Given the arguments above, this structure is energetically unfavorable due to

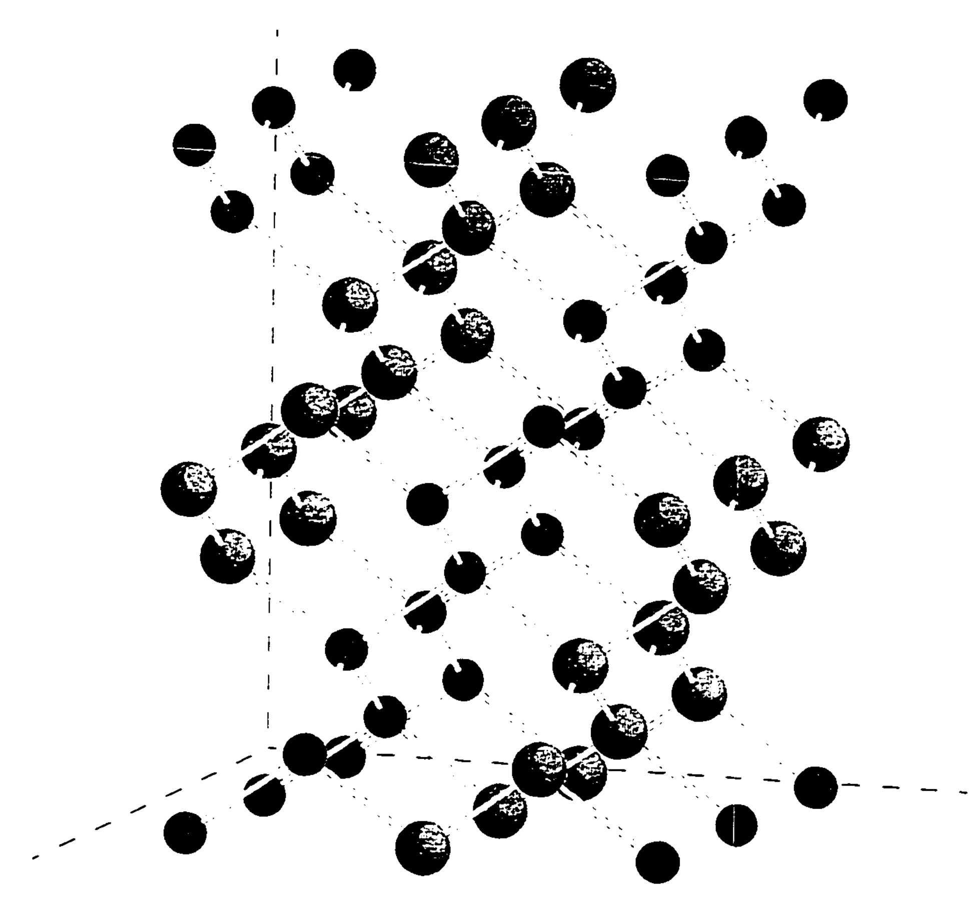

Figure 1.2: The bi-layer rhombohedral structure (RS2) for the compositional ordering of $Si_{0.5}Ge_{0.5}$ epitaxial thin films. The larger and smaller spheres represent sites of higher Ge and Si compositions, respectively.

the microscopic strain between bilayers. The RS2 structure is supported by one of the proposed mechanisms to be discussed below. Another possible structure is a cubic structure (label MS1) which has ordering simultaneously along two ⟨111⟩ directions (i.e the ⟨111⟩, and the ⟨$\bar{1}$11⟩) which are 90° apart about the [001] axis. The stacking sequence along both (111) directions is ...SiMGeMSiMGe... where M represents a mixed plane. This proposed structure was based on another surface mechanism of lateral segregation with single step flow [21]. The last structure considered is a generalized rhombohedral structure (labeled RS3) that is parameterized to be a range of structures between RS1 and RS2. Each of the four (111) layers has a parameter for the probability of composition. This structure's proposed mechanism will also be discussed.

Although all these structures are consistent with the diffraction symmetry for ordered Si_xGe_{1-x} films, only RS2 (and RS3 with parameters close to RS2) is consistent with the *ex situ* x-ray structure factors. The experiment by Tischler *et al.* [22] on a 2800 Åthick MBE $Si_{0.5}Ge_{0.5}$ film on Si(001) provided the quantitative crystallographic analysis to differentiate among the proposed structures. This provides best evidences for the bi-layer ordering of the RS2 structure, shown in Fig. 1.2. For this sample, the degree of ordering was found to be only 14%, while other groups have reported ordering parameters as high as 0.60 [23]. Looking to the arguments above, only the RS2 structure is thermodynamically stable, so different origins for the compositional ordering in SiGe need to be explored next.

1.2.3 Growth Surface and Conditions.

Since bulk equilibrium thermodynamics do not agree with the observed Si_xGe_{1-x} film structure, kinetic processes must be looked at next. The MBE growth surface is clearly the place where kinetics are expected to enter, as the surface is far from equilibrium. A number of experiments have indeed shown the surface to be important. First, the growth conditions under which the ordered structure occurs is only on (001) substrates and always with lower

than usual growth temperature (below 550°C) [12, 13, 14, 21, 22, 23, 24]. Films on (111) substrates are found to be random solid solutions. Annealing the (001) ordered films to over 650°C has reportedly caused an irreversible transition to the disordered (or random) structure [26]. Others report the needed temperature is 800°C [25]. The authors of Ref. [26] also found the transition temperature decreased as the stoichiometry of the films moved away from the 50-50% composition. They proposed a kinetic "phase diagram" of the transition as a function of stoichiometry. Another important detail that was found is the importance of the surface reconstruction on $Si_xGe_{1-x}(001)$ crystal[26].

The effect of doping or covering the growth surface with surfactant type atoms (Sb) removes the (2×1) surface reconstruction. Introducing this change is also found to destroy the compositional ordering. In a dramatic experiment [26], a single $Si_{0.5}Ge_{0.5}$ sample made with only half of the film thickness showing the ordering peaks by TED. Alongside it, the *in situ* low energy electron diffraction (LEED) experiment showed the corresponding switch of the surface structure during the film growth between the (2×1) and the (1×1). This result for Sb doping, has also been seen in some degree for Ga, and H (low temperature gas-source MBE) [26].

One growth condition that does not cause the ordering is epitaxial strain. The compositional ordering has been observed with growth on Si(001) substrates [21, 22, 23] and on Ge(001) substrates (observed in our experiments and in Ref. [24]). Ordering is also observed in films grown on graded buffer layers which are fully relaxed to provide a substrate with the same lattice parameter as $Si_{0.5}Ge_{0.5}$ [26]. The strength of compositional ordering peaks in TED and x-ray diffraction depends on the average composition of the $Si_xGe_{1-x}(001)$ alloy films. In the study by Araki *et al.*, the compositional ordering is a maximum at the 50%-50% alloy composition and decreases symmetrical to both sides of this composition. As expected, this rate of ordering decreases linearly with average alloy composition, to the minimum (no ordering) at either 0 or 100% compositions.

The compositional ordering has also been observed in thin films grown by chemical vapor deposition (CVD) [22, 26]. Although, one difference is the growth temperatures (550°C), which are higher than for MBE growth. This is related to the surface hydrogen coverage during CVD, which decreases with higher temperatures allowing the it to form the (2×1) surface reconstruction.

These details of the growth conditions lead to the conclusion that the SiGe ordering results from locally stable or kinetic structures that form at the growing surface. Once this surface process occurs, the resulting order becomes frozen into the resulting film in the form of the observed meta-stable RS2 (and RS3) structure.

1.2.4 Proposed Mechanisms

To understand the process in forming the $Si_xGe_{1-x}(001)$ ordered structure, a number of theories have been proposed which involve the growth process on the dimer reconstructed surface. I will discuss two proposed mechanisms for the ordering; one by LeGoues *et al.* [26], and the other by Jesson *et al.* [27].

The mechanism proposed by LeGoues *et al.* is based on a direct Monte Carlo simulation of the segregation at the $Si_{0.5}Ge_{0.5}(001)$ (2×1) surface previously carried out by Kelires and Tersoff [28]: Ge segregates to the surface because of its lower free surface chemical energy and drives an oscillation of composition in the alloy within the first four layers below the (2×1) reconstructed surface. This equilibrium structure can be understood in terms of local strain associated with the reconstruction, which is known to cause stresses down to at least six layers below the surface [29, 30, 31, 32]. In the layers below the surface of the alloy, Ge and Si atoms tend to migrate to sites of tensile and compressive stress, respectively. These different sites under the dimers are shown in Figure 1.3(a). This sub-surface ordering can be understood using the simple argument that the smaller Si atoms find the "smaller" sites (under compression) and the larger Ge atoms find the "larger" sites (under tension). The

(A)

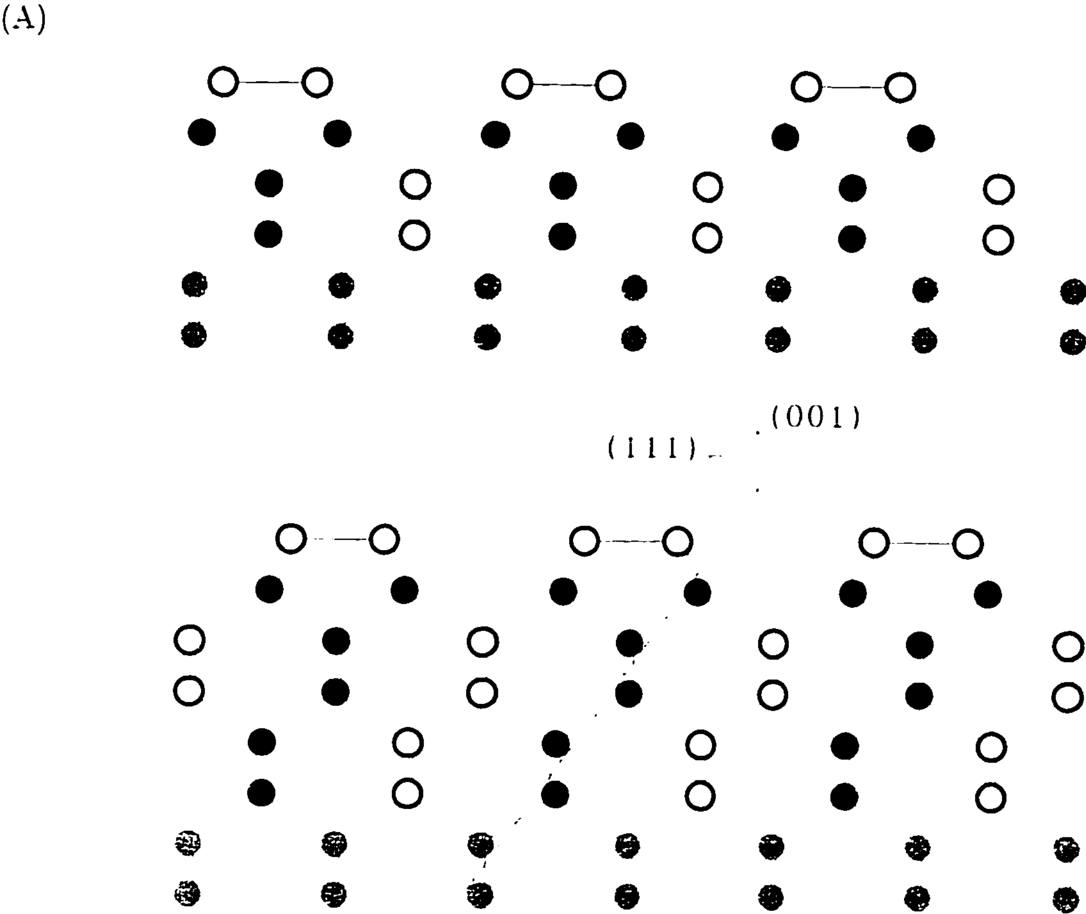

(B)

Figure 1.3: Model of LeGoues *et al.* [26]. (a) The equilibrium structure calculated by Kelires and Tersoff shown in cross section of the $Si_{0.5}Ge_{0.5}(001)$ (2×1) surface, project on a $(\bar{1}10)$ plane. Surface dimers are at the top. The larger open circles correspond to sites under tensile strain, favoring Ge occupancy. The solid circles denote sites under compressive stress, favoring Si. (Dimer sites are favored by surface free energy of Ge.) Grey circles denote sites with little preference for Si or Ge. (b) Proposed mechanism after double layer growth where fifth and sixth layers are assumed immobile, and such ordering is due to kinetics (past history), rather than actual stress or any equilibrium preference.

growth ordering mechanism occurs by this local equilibrium forming on (2×1) reconstructed terraces.

Kelires and Tersoff were able to calculate the temperature dependence of this near surface equilibrium order [28]. The ordering decays strongly with temperature, with the maximum at $T = 0$, but the order parameters are still about 15-5% for the growth temperatures typically used. The subsequent model for the film structure consists of double-height steps propagating across the surface. The ordering becomes frozen in the sixth and fifth layers, while newer layers order to a (2×1) once again, as shown in Fig. 1.3(b). The stacking sequence for the $\langle 111 \rangle$ ordering is maintained by the bilayer steps and the energy cost to forming stacking faults in the compositional ordering. Bilayer steps are reported to be predominant for Si(001) under similar growth conditions [33], and the calculated stacking fault energy of 80 meV per dimer [26] is large considering an entire (2×1) surface domain must switch dimer pairs for the fault to occur.

The other mechanism, proposed by Jesson *et al.*, is a kinetic process that occurs specifically at a double-step kink as it moves across the (2×1) surface, thus growing the crystal film. Figure 1.4(a) shows the top view of a kink on the preferred D_B bilayer step. (The D_B denotes the orientation of the (2×1) dimers to the double step.) The model first assumes the surface is covered by segregated Ge. Then, a Si adatom (in response to the Ge-rich surface) finds the preferred kink site, labeled C in the cross-section view, Figure 1.4(b). While this Si atom may exchange with the Ge atom below (site G), both sites have dangling bonds and therefore have no strong driving force for Ge segregation. Next, another Si adatom arriving from the source finds the next preferred site D. In this case, the Si and lower Ge (site H) do exchange because of the different bonding from the (2×1) dimer. This process has been labeled by Jesson *et al.* as a Ge atom "pump" mechanism [34]. Finally, the second layer of the double step grows over this, again with the assumed Ge-rich surface. With growth of the next double step and kink, flowing in the same direction, the stacking sequence is also

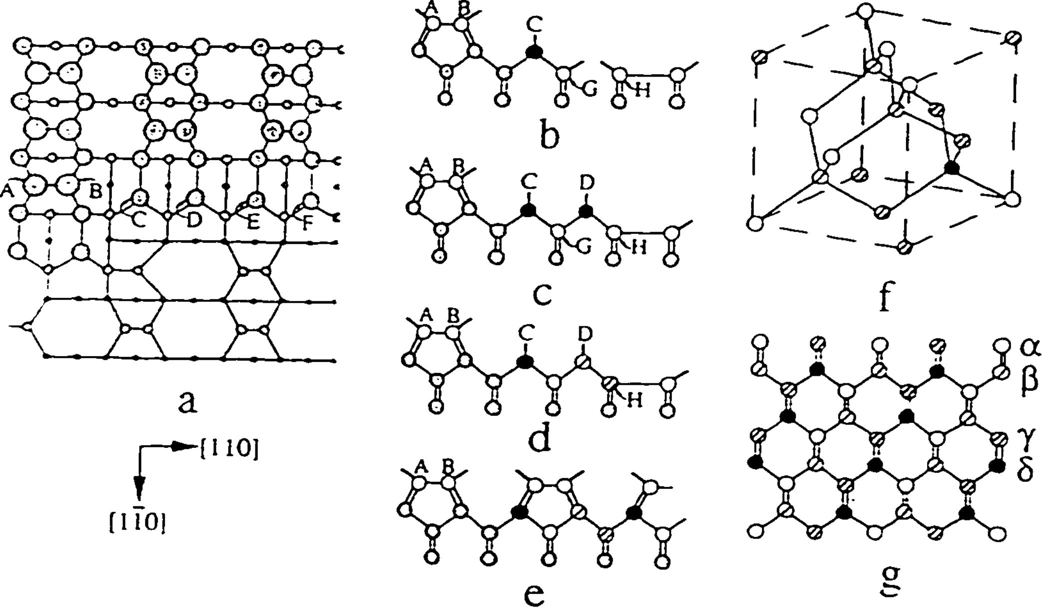

Figure 1.4: Growth-induced compositional ordering by kink flow growth of double steps. In (a) the kink is shown in plan view, the largest circles denoting the topmost atoms, and (b) to (e) show in cross section how the edge atoms (C to F) order during growth. The four projected compositions α, β and γ, δ correspond to specific Ge-rich and Si-rich, respectively, (111) planes defined by key in (g), which is the [1$\bar{1}$0] projection of RS3 structure. Mechanism proposed and figure by Jesson *et al.* [27]

correct for ⟨111⟩ ordering.

According to this mechanism, the ordering is a kinetic process from the step flow and asymmetrical segregation with the (2×1) reconstruction. If one assigns probabilities to the segregation and Ge pump mechanisms, the model gives probabilities for each of the four sites, and then to the four (111) layers. This is how Jesson *et al.* came to the structure RS3 with four parameters of composition. Their x-ray structure factor analysis (Ref. [22]) could determine a 1% relative difference between similar bilayers, i.e. 1% difference to the RS2 structure. Their other evidence for the RS3 structure was the presences of additional Bragg peaks other than the $(\frac{1}{2},\frac{1}{2},\frac{1}{2})$ type, which break the symmetry of the equal composition bi-layers of RS2 structure. Yet, these peaks are very weak.

Other indirect evidence to differentiate the two mechanisms or to elaborate a new one is not conclusive. Jesson *et al.* claim local vicinal surfaces on coherent islands from the 3D or Stranski-Krastanov growth mode [35] are required for long-range ordered domains. They argue it is for the stacking sequence to be maintained within domains where double step kinks grow in the same direction. This is not the case for layer-by-layer growth where steps and kinks flow in all directions as each layer is formed. Although the 3D growth mode may be true for $Si_{0.5}Ge_{0.5}$ grown on lattice mismatched Si(001), ordered films with large domains have been observed on graded buffer layers, where the unstrained film is thought to have a layer-by-layer growth mode [36, 37], and is thus claimed to support the mechanism proposed by LeGoues *et al.*

To conclude, the ordering mechanism observed in $Si_xGe_{1-x}(001)$ films is clearly not related to bulk thermodynamics, but to the surface properties during growth. Two mechanisms have been proposed for the residual compositional ordering, but both are based, so far, on indirect evidence. In Chapter 3, I will discuss my experiments for direct evidence of compositional ordering at the surface.

Chapter 2

Experimental Methods

2.1 Introduction

Surface x-ray diffraction represents a subset of the general techniques of x-ray diffraction and can, therefore, be done with a typical three or four circle diffractometer. But preparing and maintaining a surface structure to analyze in usual ambient laboratory conditions severely limits the experiments possible on surfaces. Another limitation is the small intensities for the diffraction from one to several monolayers of atoms, thus requiring the use other x-ray sources beyond conventional fixed anode generators. This chapter will present the specifics of our new surface diffractometer and vacuum chamber. Besides the operation of the instrument, the next section discusses the diffractometer's alignment, an important procedure. This also helps to detail the particular design of the x-ray optics and diffractometer. The last section presents the calculation for the integrated intensity of surface diffraction from this particular instrument. The resulting Lorentz factor and the presented polarization factor are used to convert measurements to structure factors, the quantity for determining of the surface atomic structure.

2.2 Surface X-ray Diffractometer

In this section, the general description of new apparatus for surface x-ray diffraction experiments will be presented, as well as its particular advantages. The general purpose of the diffractometer is to accurately align a sample in the x-ray beam and position the detector to the angle of the surface weak scattering intensity. This true for all diffractometers, but for surface experiments the environment of a ultra-high vacuum (UHV) chamber is also needed. In our design, the diffractometer motions are coupled to the sample within the UHV chamber through a bellows and rotatable Teflon sealed flange. The x-rays enter and leave the UHV chamber though a large Beryllium metal window, which gives 180° view of the sample. The sample is mounted so the angle of incidence and exit are small and therefore the direction of momentum transfer is near the plane of the surface (the direction of interest). The diffractometer has an additional motion to the detector, called γ, which is perpendicular to the 2θ motion. The 2θ angle is usually renamed δ so it is not confused with $2\theta_B$, the full Bragg scattering angle which is then compound angle from these two motions. The out-of-plane motion γ allows larger range of access to momentum space with the limited motions of the sample within the chamber. The UHV chamber is also equipped with standard surface preparation and characterization tools such as an ion gun for sputter etch and a cylindrical mirror Auger spectrometer. In the future, it will be equipped with a sample heater, enabling typical science surface preparation techniques.

The most important advantage of this equipment is its connection to the Epi Center vacuum transfer system. The x-ray chamber is stationed at one end of the Epi Center's four UHV transfer tubes, which are interconnected at the center. Figure 2.2 is a sketch of the floor plan of the Epi Center. The system allows samples to be prepared in one of seven molecular beam epitaxy (MBE) chambers and then transferred under UHV to the x-ray chamber for analysis. Besides our surface x-ray station, there are analysis stations for scanning tunneling

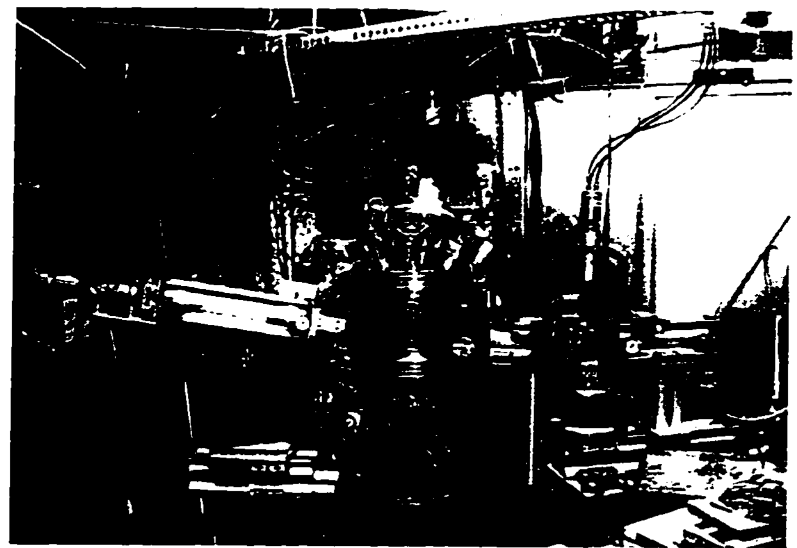

Figure 2.1: Photograph of x-ray diffractometer and UHV analysis chamber. To the left is the beam path and detector at scattering angles γ and δ (or called 2θ). To the right is the rotating anode and monochromator, with its monitor detector and shielding beam paths. In the center is the UHV chamber and its Beryllium x-ray window.

microscopy (STM), and x-ray photoemission spectroscopy (XPS or ESCA). The Epi Center x-ray source is a 18kW rotating anode generator. Although a synchrotron source can provide surface scattering signals 10 to 100 times larger, the Epi Center provides an advantage in being able to analyze sample, *in situ*, of greater complexity or composed of uncommon materials, grown in one of the many MBE chambers.

Another advantage of this diffractometer is the design of the x-ray optics. In order to increase the incident x-ray intensity, a curved highly-oriented pyrolytic graphite (HOPG) monochromator crystal is used. This focuses more of the x-rays from the generator to a point on the sample surface. Although the focusing causes a large angular divergence, resulting in lower resolution, this divergence is directed perpendicular to the surface. The 0.3° mosaic of the graphite crystal then determines the in-plane divergence. The diffractometer is also equipped with a 1D position sensitive detector. This has a large angular acceptance perpendicular to sample surface and narrow acceptance in the plane of the surface. The combination of monochromator and detector gives reasonable in-plane resolution, while the

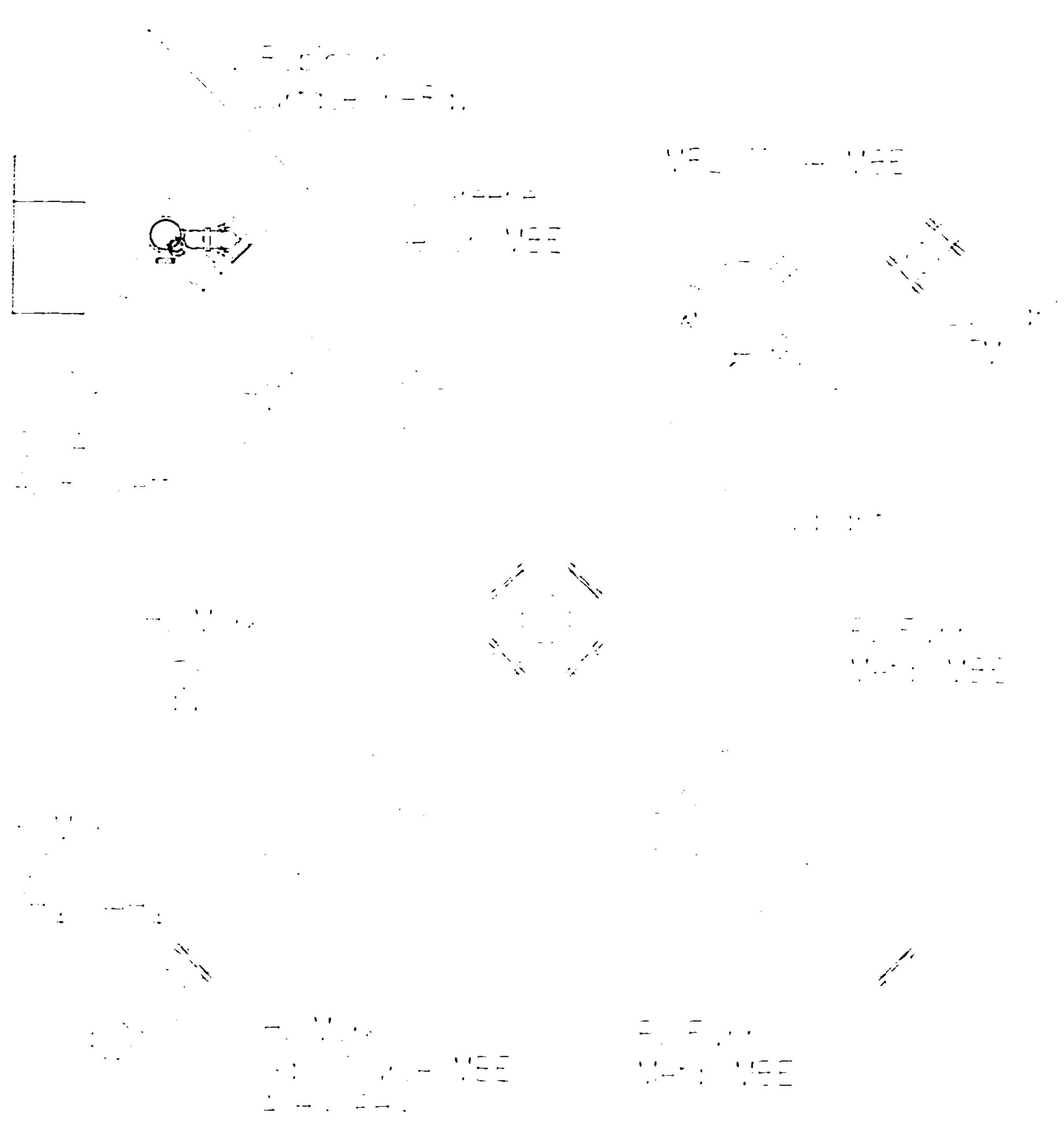

Figure 2.2: Floor sketch of the Epi Center. A collaborative laboratory for research of molecular beam epitaxy.

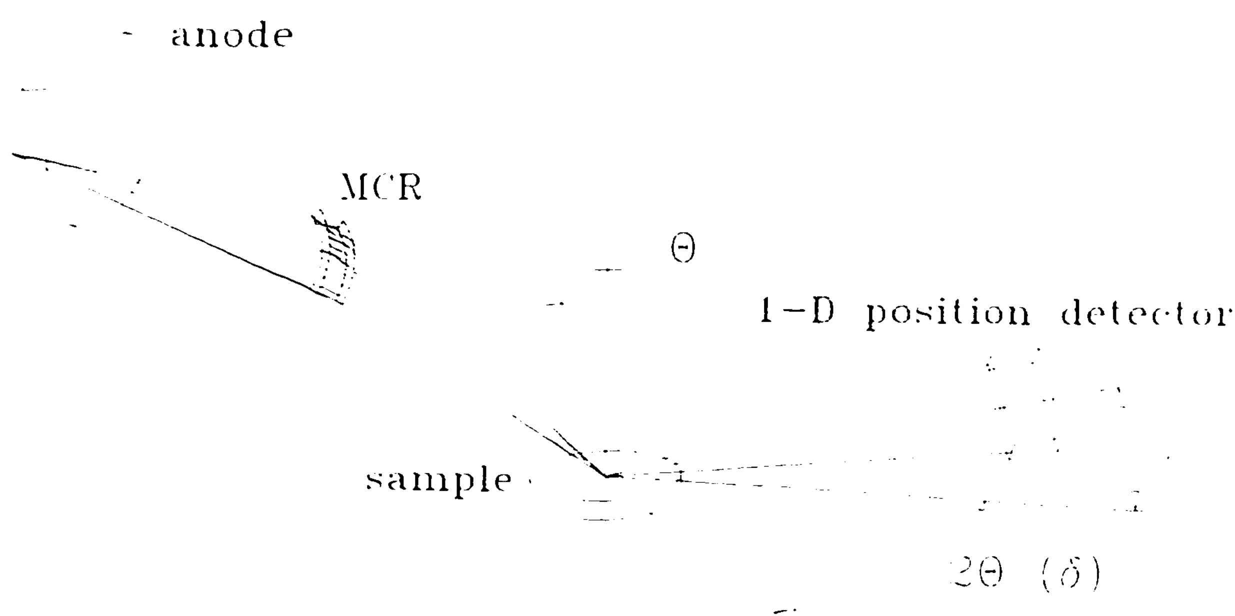

Figure 2.3: Idealized sketch of the components and relative geometry of the surface x-ray diffractometer.

large out-plane divergences allows integration along the surface normal direction, i.e. along the crystal truncation and surface reconstruction rods. In section 2.4 below, this resolution function is calculated in detail to account for the changes it makes as the scattering angles change. Figure 2.3 shows a sketch of the x-ray optics design and a typical surface diffraction condition. This design helps overcome the low intensities when using a rotating anode source, while sacrificing resolution. Measurements on a Ge(001) surface have seen up to 100 counts per second from (2×1) reconstruction rods. The instrument is also equipped with a scintillation x-ray detector, which provides finer energy resolution then position-sensitive gas proportional detector.

One of the particulars in the design of the analysis chamber is the bellows and rotatable

Teflon sealed flange for the sample rotations. This design is common mechanical feedthrough for the motion of a surface diffractometer [40]. Besides the main sample rotation, θ, the bellows allow the tilting of the sample, by the rotations χ and ϕ. The commercially manufactured χ and ϕ arc segment stack is constructed with the center of rotations at 170 mm above its top mounting surface. Ideally this is where the sample surface would be. But for more space, the sample position was design at 15 mm above that (185 mm total). The space is need for electrical and/or mechanical feedthrough flanges attached to the already very compact sample holder and rotatable seal flange assembly. This distance, $d = 15$ mm, causes the displacement of the sample from the diffractometer's axis with rotation of χ or ϕ. Returning the sample to the position where its surface intersects the axis at the same height can be made by the xy-translation stage underneath the arc segment stack using the formula

$$\Delta x = d \cdot \tan(\chi/2)$$
$$\Delta y = d \cdot \tan(\phi/2) \ . \tag{2.1}$$

These translations can be incorporated into the diffraction control program, *Super*. A sample surface is generally translationally invariant, and no problems or systematic errors have been seen from ignoring these displacements and so they were omitted in these experiments.

As mentioned before the diffractometer includes an additional out-of-plane detector rotation γ. This motion, first suggest by Vlieg et al.[38], is exactly the same in the 6-circle surface diffractometer built by Abernathy and Mochrie (MIT)[39, 41]. The six angles to reciprocal space calculation used by these groups was programmed in our control program *Super*. This allows the operator to specify the (hkl) coordinates and two additional constraints for the computer to uniquely calculate, and then control the motion of the instrument to the corresponding five angles. The two additional constraints are usually; 1) fixing the incident angle of x-ray beam to the sample surface and 2) having the diffraction rod align to the vertical divergence of the monochromator. Physically, the last condition means that the surface nor-

mal is held in the vertical plane parallel to this divergence, so that the 2-D diffraction rod is excited simultaneously along its length. The last detail is α, the floor rotation angle for the 6-circle diffractometers mentioned above, is not present for our instrument. Thus it is the last constraint for the full six angle calculation that α is always zero.

Another point for operation of the diffractometer is problems with very small incident and exit angles which are close to beam divergences. This problem at very small angles corresponds to part of the beam having a negative incident angle or part of the detector's acceptance having a negative exit angle from the sample surface. These parts of the beam are strongly attenuated or blocked by the bulk sample crystal or the 3 inch diameter sample holder (the molybdenum puck). This decrease in the diffracted intensity could be corrected for, but its sensitivity to the mis-alignment of beam height (to be discussed further in the next section) makes it difficult to remove such systematic errors. In general, measurement of intensities are not used in these very grazing angle cases.

2.3 Diffractometer Alignment

This section provides a description of how our diffractometer instrument is aligned. The alignment of any diffractometer is important for reliable measurements without systematic errors. The Epi Center's diffractometer is particularly difficult to align because; 1) the curved HOPG monochromator reflects a wide vertically diverging beam and 2) the UHV chamber does not allow one to directly measure the focused incident x-ray beam at the sample position. Another important procedure is accurately centering the beam to the sample's height. This is important because of the relative low angle of incidence for the x-ray beam to the sample. For example, a 10×10 mm square sample titled at an incidence angle of 3.5°means the sample cross-section to the focused 1.5 mm tall incident beam is only 0.61 mm. And finally, the focal spot of the monochromator should be at the sample position for maximum signal.

The first step in the alignment of the diffractometer is to align the monochromator's θ angle and reflect the Cu K_α (and not K_β) x-rays from the rotating Cu anode generator. **WARNING!! Even at the lowest generator power, the full graphite crystal collects and focuses enough x-rays to immediately damage the position sensitive detector (PSD) and possibly scintillation detectors. Many metal foil filters must be used protect the detector from the direct beam.** Once there is a beam, it must be centered at the sample height and be perpendicular to and intersect with the vertical axis of the diffractometer. To accomplish the first two requirements, the surveyor's telescope is set to the sample height, which was designed and measured at assembly to be 185 mm vertical above the face of the ϕ and χ arc segment stack. The leveled telescope is then used to set the heights of the anode source, the monochromator, the vertical slit of the monochromator and detector. The goal is to get the x-ray beam from the source, to the monochromator, and to the detector all within the horizontal plane at the sample height. The reflection from the monochromator is then adjusted by its angle χ to direct the beam to the detector defined by its slits. With the full monochromator giving a wide vertical beam, the detector will be very insensitive to this adjustment. If the vertical slit directly in front of the monochromator (known to the program as MCR-vert slits) is closed to ≈ 2 mm, this restricts the reflection to only a well defined central beam. Figure 2.4 sketches the beam alignment to the sample height and the defined beam from the MCR-Vert slits. Once this χ angle adjustment is made, additional adjustment of θ reflection angle may be needed.

Once the incident x-ray beam is maximized and adjusted to the sample height's horizontal plane, the beam must intersect the diffractometer axis. With most diffractometers, this can be accomplished by using lead foil with a pin-hole, which is centered on the axes and then, the beam adjusted to pass through the pin-hole. This is not possible with our diffractometer, because of the sample position inside the UHV chamber. Instead, we use a lead pin-hole outside the chamber, attached by the magnetic optical stand to the diffrac-

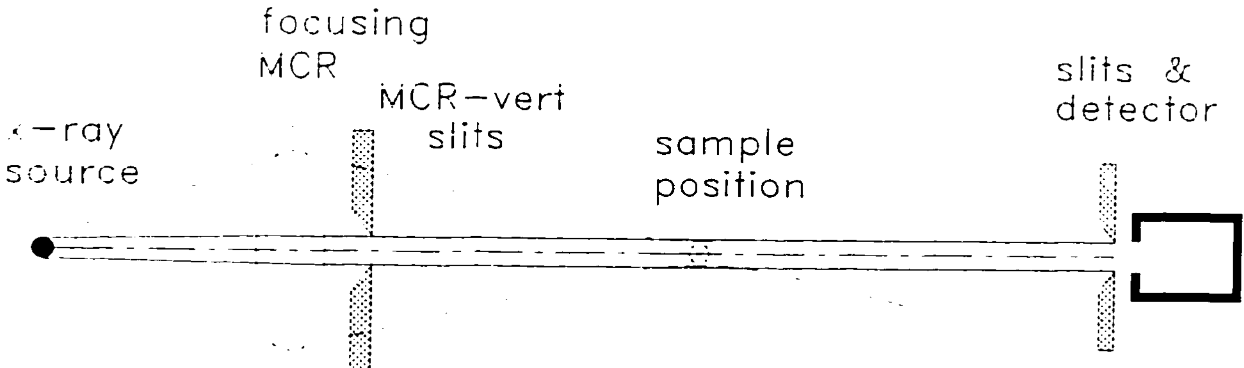

Figure 2.4: Sketch of horizontal view of monochromator's focusing x-ray optics and use of vertical slits "MCR-vert" for alignment of beam height with detector measurement

tometer, to measure beam's position on both sides as it enters and exits of the chamber. The beam will intersect the center once the beam on both sides is separated by exactly 180°. The x-ray beam can be translated by the micrometer at the base of the monochromator stage and beam-path assembly. This sliding stage pivots under the source position, allowing the monochromator reflection angles to be unchanged. For a large translation, the different collection angle from the anode source can either change the source's collected cross section making the beam's horizontal width larger or smaller, or change the collected x-ray intensity because of absorption at grazing angles through the anode.

The last adjustment for the incident beam is the focal spot. The position along the beam where it focuses to its smallest size should be the positioned at the center of the UHV chamber, i.e. the sample position. The beam focal distance can be measured when the UHV chamber is opened, usually by photographs of the beam along its length [1] . The whole source and monochromator stand can be moved to get the focal point to the sample position. This finishes the alignment of the incident x-ray beam, but repeating the process (except the last step) is usually done making finer adjustments and corrections that couple from other

[1]This distance and photographs are documented in the diffractometer's notebook. This measurement is also done by moving the whole generator stand or removing the UHV chamber from the path of the beam reflected by the monochromator

adjustments. Finally, the zeroes of the scattering angles 2θ (or called δ) and γ are set to the incident beam. The zeroes of 2θ and γ should be checked regularly (such as, before each new sample is transferred into the x-ray UHV chamber). This is done to check for an errors in the motor control or lost stepping pulses to 2θ and γ. The rest of the alignment has been found to be stable. For any changes, such as removing the monochromator slits for the UHV chamber bake-out, it is wise to repeat the whole alignment process.

An alternative or additional adjustment is to use diffraction from a small sample crystal. While measuring the total diffracted intensity, the monochromator's χ angle can be finely adjusted for the incident x-ray beam to fully hit the sample. The smaller the sample crystal and incidence angle, the more sensitive the adjustment is. The difficulty is assuring that the total diffracted intensity is measured during this maximization. This means using the MCR-vert slits closed down to 2 mm and the detector slits fully opened. An additional technique is to use a reflection which is close to the surface. The ideal reflection would be at γ a few degrees positive. This type of reflection makes the scattering plane nearly perpendicular to the adjustment of the incident beam (by the monochromators χ), thus making the change a rotation about $\vec{q}$, and thus maintaining the reflection condition. So, using a (111) Bragg peak from a silicon [001] substrate is not a good choice because of the large γ angle, and yet the surface reflections (220) or (400) are also difficult because the substrate being mounted to a molybdenum holder. The alternatives are using higher order reflections with smaller γ angle such as (511), or using a different crystal, such as sapphire, with more near-plane Bragg peaks.

2.4 Integrated Intensity Calculation

2.4.1 Introduction

In an scattering measurement, the measured quantity, usually x-ray photons counted per unit of time, has to be directly transformed into the quantity, structure factors, in order to solving the structure of interest in the experiment. The scattered intensity field is the typically derived quantity in the equation for light waves. But the x-ray intensity is not as directly measurable as one wishes because of four main experimental reasons. First, an intensity has the units of energy per unit of area per unit of time. An x-ray detector has a finite area which integrates a region of phase space for the scattered x-rays. While the detector area is usually constant for each experiment, its collecting volume of phase space changes with its position of scattering angle. For surface diffraction where the intensity is continuous along rods in reciprocal space, the detector area can also vary in its cross section of along this rod, thus changing the integrated intensity. The second experimental complication is the incident x-ray radiation, which is not an ideal plane wave, limited to one incident direction (i.e. an infinitesimally small volume in phase space for the incident x-rays). Instead, all the x-rays in a distribution of directions incident on the sample can be scattered and then measured by the detector. The third complication is that the detector has a limited energy discrimination and integrates over a spectrum of x-rays, from the elastic to the inelastic x-rays. This problem is usually resolved by measuring the broad diffuse inelastic scattering as background, which is then subtracted from the elastic diffraction peak. The four experimental complication relates to the mosaics of real crystals, which can also pose difficulties in measurement of x-ray intensities.

In the simplest of experimental cases, the measured intensity of a single point in reciprocal space should be directly proportional to the square of the intrinsic structure factor of the crystal. In most cases, though, the experimental complications/constraints described above,

combine to make the measure intensity dependent on the constraints instead of on the intrinsic structure factors of the crystal. The remedy of this problem lies in another integration. For each peak, the sample is rotated and the x-ray intensity is measured to give what is usually the integrated intensity. In a conventional three-dimensional crystal measurement, the result is independent of the detector acceptance area or the incident beam convergence, and is therefore an absolute measurement[1]. The similar measurement for a two dimensional lattice (such as a monolayer or surface reconstructed crystal) can be made, except it does not remove all experimental dependencies. What is left is one complex factor (later called the Lorentz factor) which depends on the length or cross-section of the diffracted rod integrated.

In the following sections, the analytical calculation for the integrated intensity for diffraction from a two dimensional lattice will be presented. It begins with diffraction intensity and the initial integration equation, setup similar to Warren [1] and Robinson [5], but will include the additional integrations for the incident beam convergence. This is needed because of the graphite focusing monochromator used in diffractometer. Also presented are the details for the reciprocal space coordinates and change of variable calculations needed to easily perform the integrations. Last will be the resulting formula and discussion of its importance and use.

2.4.2 Integrated Intensity

We begin the calculation for the integrated intensity for the Epi Center's diffractometer with the equation for the diffraction intensity from an ideal 2-D lattice,

$$I(\vec{k}_f, \vec{k}_i) = I_o(\vec{k}_i) \left(\frac{e^2}{mc^2 R^2} \right)^2 |F(\vec{q})|^2 \, S_1(\vec{q}) \cdot S_2(\vec{q}), \tag{2.2}$$

where I_o is the incident x-ray intensity with wavevector $\vec{k}_i$. Next in this equation is the electron cross section and the unit cell structure factor $F(\vec{q})$, the focus of interest, where

$$\vec{q} = \vec{k}_f - \vec{k}_i \, . \tag{2.3}$$

The final terms are in the form of a product of Laue functions (also called slit functions from optical diffraction),

$$S_i(\vec{q}) = \frac{\sin^2\left(\frac{1}{2}N_i\vec{a}_i \cdot \vec{q}\right)}{\sin^2\left(\frac{1}{2}\vec{a}_i \cdot \vec{q}\right)}\,, \tag{2.4}$$

which are the diffraction functions from a 2-D finite crystal with a unit cell defined by $\vec{a}_1$ and $\vec{a}_2$, and the N's representing the crystal size in the number of unit cells along those respective directions[5]. As said before, this represents the ideal intensity field scattering from an ideal crystal with an ideal incident plane wave of x-rays.

Next, is to describe the real measurement of this intensity. The calculation is for the integrated intensity for a particular peak in reciprocal space. The detector has slits and/or optics which determine the area over which the intensity is measured. The sample is also rotated by the angle θ at a constant rate in time with angular velocity ω during the measurement, giving

$$E(\vec{q}) = \int\int_{peak} dA\, dt\, I(\vec{k}_f, \vec{k}_i) \; = \int_{peak} R^2 d\alpha\, d\beta \frac{d\theta}{\omega}\, .I(\vec{k}_f, \vec{k}_i) \tag{2.5}$$

The variables α and β are the solid angles of the detector area, at the distance R from the sample. But this usual starting equation does not include the convergence of the incident beam. This means the incident intensity, $I_o(\vec{k}_i)$ is a distribution where the total power incident on the sample is

$$P_o = \int\int d\eta\, d\rho\, T(\eta, \rho)\; I_o\,. \tag{2.6}$$

In this integration, η and ρ are the angles subtended at the sample from the monochromator representing the convergent incident x-ray beam. The width of the distribution, in terms of solid angles η and ρ, is represented by the transmission function $T(\eta, \rho)$. Combining the incident beam distribution, which is also integrated by the measurement, with Eq. 2.5 and using a similar transmission function $D(\alpha, \beta)$ for the detector angular widths, gives

$$E(\vec{q}_o) = \frac{R^2}{\omega} \int d\alpha\, d\beta\, d\theta\, d\eta\, d\rho\, T(\eta, \rho) D(\alpha, \beta) I(\vec{k}_f, \vec{k}_i). \tag{2.7}$$

This equation is the fully generalized starting point for the integration of the incident beam distribution angles, the exit beam distribution angles, and the sample rotation angle. These five angles represent the total integrations perform when making an integrated intensity measurement.

The construction of the equation is also represented by Fig. 2.5 which shows the variables α and β are the solid angles of the detector area, and η and ρ are the solid angles from the monochromator. These angles are relative to the centered final and incident wavevectors, respectively. The geometry or direction of the detector's solid angles (and volume in momentum space) are dependent on the scattering angles δ and γ which also determine the peak measured in momentum space, $\vec{q}$. The width of angular acceptance of the detector is determine by the function $D(\alpha, \beta)$ and respectively the same is done by $T(\eta, \rho)$ for the incident angles. The form of these functions can be step-like windows, like the physical dimensions of the slits used, but here I will follow calculation by Schamper *et al.*[42] and use Gaussian functions. This better represents the beam profile in some cases, but more importantly, it also makes the calculation tractable because the integrations with variables of an Gaussian gives another Gaussian. The change in accuracy is negligible and more importantly, it does not change the dependence of the volume integrated on the scattering angles δ and γ.

2.4.3 Integrations

Assuming this Gaussian form, the equation to be calculated is

$$E(\vec{q}_o) = \frac{R^2}{\omega} \int d\alpha\, d\beta\, d\eta\, d\rho\, d\theta\, e^{-\alpha^2/a^2} e^{-\beta^2/b^2} e^{-\eta^2/n^2} e^{-\rho^2/p^2} I(\vec{k}_f, \vec{k}_i), \tag{2.8}$$

where the width of the detector acceptances are a and b, which are along the scattering angles δ and γ, respectively. The width of the incident beam convergence, n and p, are along the perpendicular direction to the beam, $\hat{x}_L$ and $\hat{z}_L$. With the incident beam direction along $\hat{y}_L$, this describes the orthonormal coordinate system in the laboratory frame, as shown in Fig.

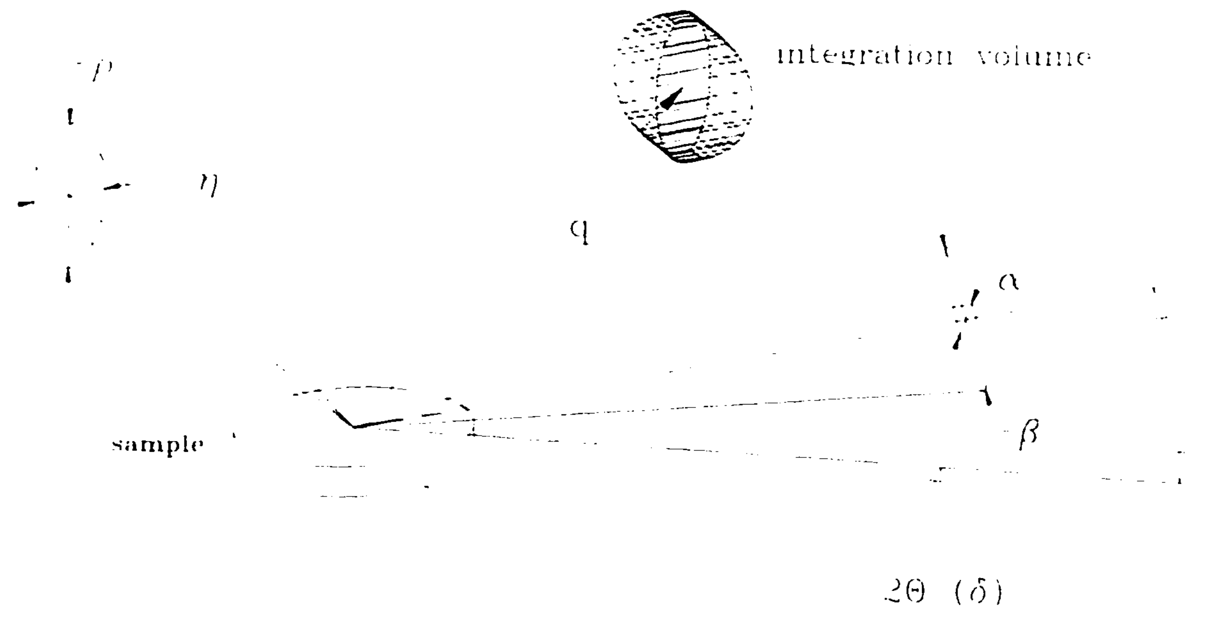

Figure 2.5: Figure of real space divergence and acceptance angles used as variables in the calculation of the integrated intensity. Also shown is an example volume of integration at the end of the vector q.

2.6. This is also the starting coordinate system describing the diffractometer motions (see Ref. [41] and [39] for complete details of diffractometer angle calculations used). Similarly the detector position describes another coordinate system where the final wavevector is along the direction $\hat{y}_f$ and the acceptance widths along $\hat{x}_f$, $\hat{z}_f$. The last variable of integration is θ, a rotation about the axis along $\hat{z}_L$.

The dependence of the wavevectors $\vec{k}_f$ and $\vec{k}_i$ on the five angles of integration is only a change in their directions. This means the additions of small perpendicular vectors along components $\hat{x}$ and/or $\hat{z}$ in their respective frames. For example, the angle α adds the vector $|k|sin(\alpha)\hat{x}_f$ to $\vec{k}_f$. But with the angle being small, the approximation $sin\alpha \approx \alpha$ is used. Similarly for all five angles, the full dependencies are

$$\vec{k}_i = \vec{k}_i^o + |k|\eta\hat{x}_L + |k|\rho\hat{z}_L - |k|\theta\hat{x}_L \tag{2.9}$$

$$\vec{k}_f = \vec{k}_f^o + |k|\alpha\hat{x}_f + |k|\beta\hat{z}_f - |k|\theta\cos(\gamma)\hat{x}_f. \tag{2.10}$$

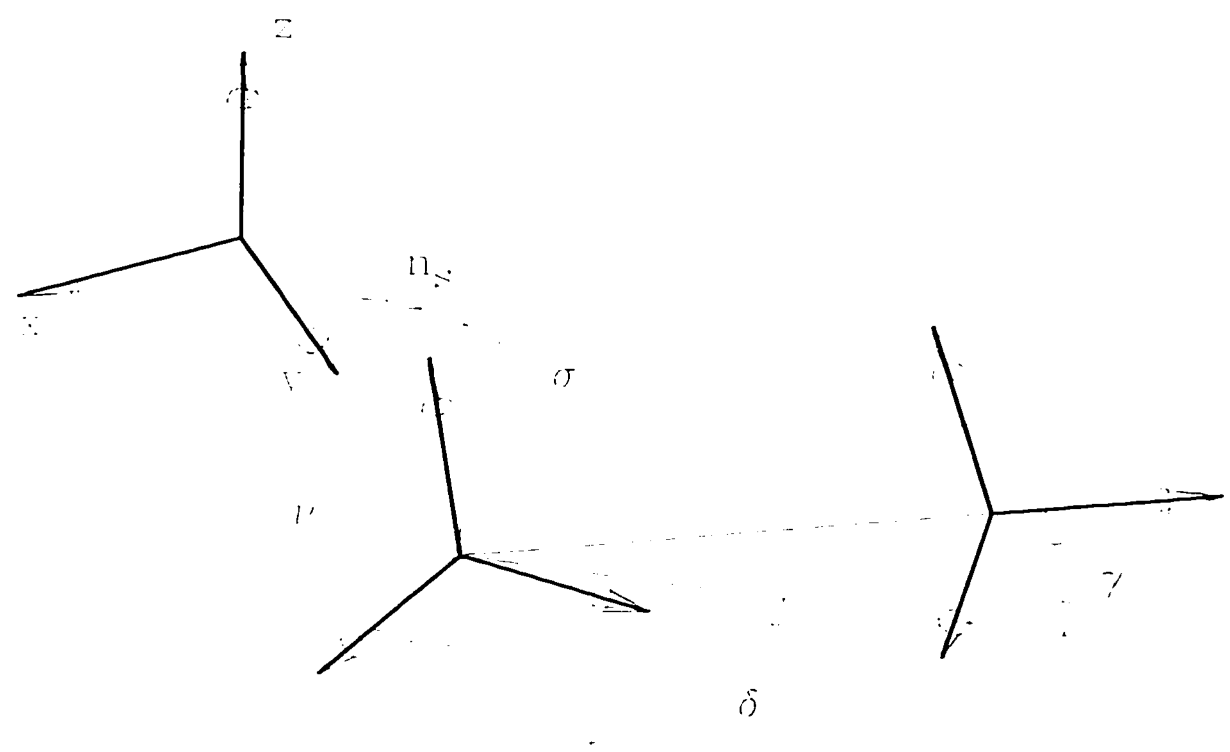

Figure 2.6: Figure of the three different orthogonal coordinate frames used in the calculation. All are related by rotation matrices.

The θ motion really changes the sample position, not the incident and final wavevectors, but in momentum space the effect is the same with respect to the diffraction peak. The momentum transfer is then

$$\vec{q} = \vec{k}_f^o - \vec{k}_i^o + |k| \left[\alpha \hat{x}_f + \beta \hat{z}_f - \eta \hat{x}_L - \rho \hat{z}_L - \theta \left(\cos(\gamma) \hat{x}_f + \hat{x}_f\right)\right] \tag{2.11}$$

$$\vec{q} = \vec{q}_o + \Delta \vec{q} \, . \tag{2.12}$$

Next, it is assumed that the structure factor is slowly changing function over the volume of integration so that it can be removed from the integrand, as

$$|F(\vec{q})|^2 \approx |F(\vec{q}_o)|^2 \, . \tag{2.13}$$

Another simplification is for the Laue functions which are maximum at $\vec{q}_o$ so that

$$S_i(\vec{q}_o + \Delta\vec{q}) = S_i(\Delta\vec{q}) \, . \tag{2.14}$$

(This equality is proven in Warren [1].) The completed equation, with all the substitutions of equations above, is then

$$\begin{aligned} E(\vec{q}_o) &= I_o \left(\frac{e^2}{mc^2R^2}\right)^2 |F(\vec{q}_o)|^2 \frac{R^2}{\omega} \\ &\quad \times \int d\alpha \, d\beta \, d\eta \, d\rho \, d\theta \; e^{-\alpha^2/a^2} e^{-\beta^2/b^2} e^{-\eta^2/n^2} e^{-\rho^2/p^2} S_1(\Delta\vec{q}) S_2(\Delta\vec{q}) \end{aligned} \tag{2.15}$$

with

$$\Delta\vec{q} = |k| \left[\alpha \hat{x}_f + \beta \hat{z}_f - \eta \hat{x}_L - \rho \hat{z}_L - \theta \left(\cos(\gamma) \hat{x}_f - \hat{x}_L\right)\right] \, . \tag{2.16}$$

This set of Gaussian integrals are easy to evaluate, except for the functions $S_i(\Delta\vec{q})$ which are also peaked at $\Delta\vec{q} = 0$. This leads to the next step of the calculation: changing the variables of integration from real space angles to momentum space. The best directions in momentum space to choose are ones that simplify the functions $S_i(\Delta\vec{q})$. These functions are only dependent on $\Delta\vec{q}\cdot\vec{a}_i$, where $\vec{a}$'s are the vectors in the plane of surface. The surface vectors combine to define another orthogonal coordinate system, $\hat{x}_s$, $\hat{y}_s$ in the surface plane and $\hat{z}_s$

is defined as being along the surface normal $\vec{n}$, also shown in Fig. 2.6. The angle between $\vec{a}_1$ and $\hat{x}_s$ (or a rotation about the $\hat{z}_s$ axis) is not important. The typical sample configuration is with the surface normal along the yz-plane in the lab coordinates. As discussed above in section 2.2 and in Ref. [41], this configuration brings the continuous intensity along the surface diffraction rods in close alignment to the divergence of the incident x-ray beam. Alternatively, the experimental condition could be for the surface normal to lie in the plane of the detector, aligned to the large acceptance of the position sensitive detector along the γ diffractometer motion. Then the best angles to describe the sample surface coordinate system's relation to the laboratory coordinate system are σ, the tilt angle from the z-axis, and ν, the angle in the surface plane determining the direction of the tilting [2]. The coordinate transformation is exactly the same as that used between the lab (the incident beam) frame and the final x-ray beam at angles, δ and γ. The transformation matrix is the angle δ is

$$\Delta = \begin{bmatrix} \cos\delta & -\sin\delta & 0 \\ \sin\delta & \cos\delta & 0 \\ 0 & 0 & 1 \end{bmatrix}. \tag{2.17}$$

The matrix for γ rotation about the x-axis is

$$\Gamma = \begin{bmatrix} 1 & 0 & 0 \\ 0 & \cos,\gamma & -\sin\gamma \\ 0 & \sin\gamma) & \cos\gamma \end{bmatrix}. \tag{2.18}$$

The final wavevector in the lab frame using the transformations are

$$\vec{k}_f^\gamma \xrightarrow{\Gamma} \vec{k}_f^\delta \xrightarrow{\Delta} \vec{k}_f^L . \tag{2.19}$$

For surface normal the transformations are similarly

$$\hat{n}_s^\sigma \xrightarrow{\Sigma} \hat{n}_s^\nu \xrightarrow{\mathrm{N}} \hat{n}_s^L . \tag{2.20}$$

[2]The diffractometer control program *Super*, uses different angles to describe the sample surface orientation. The usual reciprocal space to angles calculation mode is with the surface normal held within the lab frames yz-plane and to fix the incident angle, called*beta*. This corresponds to $\sigma = beta$ and $\nu = 0$. See Ref. [41] for more details of this different surface orientation description.

Then, returning to Eq. 2.16 and using the rotation matrices to write out $\Delta\vec{q}$ in the lab frame for the unit vectors

$$\hat{x}_f = \Delta\Gamma\hat{x}_{\mathrm{L}}$$

$$\hat{z}_f = \Delta\Gamma\hat{y}_{\mathrm{L}}$$

giving the result

$$\Delta\vec{q}^{\,\mathrm{L}} = |k| \begin{bmatrix} \alpha\cos(\delta) + \beta\sin(\delta)\sin(\gamma) - \rho + \theta\,(1 - \cos(\delta)\cos(\gamma)) \\ \alpha\sin(\delta) - \beta\cos(\delta)\sin(\gamma) - \theta\sin(\delta)\cos(\gamma) \\ \beta\cos(\gamma) - \eta \end{bmatrix}. \tag{2.21}$$

To describe this same vector in the coordinate frame of the sample surface, we use the inverse transformation

$$\Delta\vec{q}^{\,s} = (N\Sigma)^{-1}\,\Delta\vec{q}^{\,\mathrm{L}} \tag{2.22}$$

where

$$(N\Sigma)^{-1} = \begin{bmatrix} \cos(\nu) & \sin(\nu) & 0 \\ -\cos(\sigma)\sin(\nu) & \cos(\sigma)\cos(\nu) & \sin(\sigma) \\ \sin(\sigma)\sin(\nu) & -\sin(\sigma)\cos(\nu) & \cos(\sigma) \end{bmatrix}. \tag{2.23}$$

This further mixes the variables in linear combinations with trigonometric coefficients from the scattering angles and the relative angles of the sample surface. Now the x and y components of $\Delta\vec{q}^{\,s}$ are the variables we use as the new integration variables. The corresponding angle variables to switch with are chosen to be θ and α. Then solving for these in term of the new integration variables Δq_x, Δq_y, β, η, and ρ

$$\alpha = A\beta + B\eta + C\rho + D\,\Delta q_x + E\,\Delta q_y \tag{2.24}$$

and

$$\theta = F\beta + G\eta + \rho + H\,\Delta q_x + I\,\Delta q_y. \tag{2.25}$$

The full trigonometric expressions for the new coefficients A through I will be displayed later, as only a few are needed in the end. Besides substituting for α and θ in Equation. 2.15,

the Jacobian is needed

$$d\alpha d\theta = J\left|\frac{\partial\alpha\ \partial\theta}{\partial(\Delta q_x)\ \partial(\Delta q_y)}\right| d(\Delta q_x)d(\Delta q_y) = \frac{d(\Delta q_x)d(\Delta q_y)}{\cos(\sigma)\sin(\delta)|k|^2}. \tag{2.26}$$

The result for Eq. 2.15 substituting Equations 2.26 and 2.24 is

$$\begin{aligned} E(\vec{q}_o) &= I_o\left(\frac{e^2}{mc^2R^2}\right)^2 |F(\vec{q}_o)|^2 \frac{R^2}{\omega}\frac{1}{\cos(\sigma)\sin(\delta)|k|^2} \\ &\times \int d(\Delta q_x)\,d(\Delta q_y)\,d\beta\,d\eta\,d\rho\, e^{-(A\beta+B\eta+C\rho+D\,\Delta q_x+E\,\Delta q_y)^2/a^2} \\ &\times e^{-\beta^2/b^2}e^{-\eta^2/n^2}e^{-\rho^2/p^2}S_1(\Delta\vec{q})S_2(\Delta\vec{q}). \end{aligned} \tag{2.27}$$

The Laue functions $S_i(\Delta\vec{q})$ can now be separated because they are now only dependent on the x and y components within the surface coordinates. The integrated intensity can be re-written as

$$\begin{aligned} E(\vec{q}_o) &= \frac{I_o}{\omega}\left(\frac{e}{mc^2}\right)^2 |F(\vec{q}_o)|^2 \frac{1}{\cos(\sigma)\sin(\delta)|k|^2} \\ &\times \iint d(\Delta q_x)\,d(\Delta q_y)\,S_1(\Delta q_x,\Delta q_y)S_2(\Delta q_x,\Delta q_y) \\ &\iiint d\beta\,d\eta\,d\rho\, e^{-(A\beta+B\eta+C\rho+D\Delta q_x+E\Delta q_y)^2/a^2}e^{-\beta^2/b^2}e^{-\eta^2/n^2}e^{-\rho^2/p^2} \end{aligned} \tag{2.28}$$

Now the Gaussian integrals in the angle variables can be performed simply by repeated use of this formula for

$$\int dx\, e^{-x^2/u^2}e^{-(x+y)^2/v^2} = \frac{uv\sqrt{\pi}}{\sqrt{u^2+v^2}}e^{-\frac{y^2}{u^2+v^2}}. \tag{2.29}$$

which results in

$$\begin{aligned} &\iiint d\beta\,d\eta\,d\rho\, e^{-(A\beta+B\eta+C\rho+D\Delta q_x+E\Delta q_y)^2/a^2}e^{-\beta^2/b^2}e^{-\eta^2/n^2}e^{-\rho^2/p^2} = \\ &\frac{(\pi)^{3/2}abnp}{\sqrt{a^2+A^2b^2+B^2n^2+C^2p^2}}\exp\left(\frac{-(D\ \Delta q_x+E\ \Delta q_y)^2}{a^2+A^2b^2+B^2n^2+C^2p^2}\right). \end{aligned} \tag{2.30}$$

Now the final integration of the reciprocal space variables, Δq_x and Δq_y, can be solved analytically with the last Gaussian function. This final integration that is not needed because one can use the general experimental requirement that the detector slits are at least

wide enough to fully integrate the peak. In the formulas above, this means the final Gaussian width is experimentally required to be larger that the peak width determined by the functions, S_1 and S_2. This is strictly the same condition followed by Warren [1] to obtain the equivalent three-dimensional integrated intensity for Bragg peaks. If this where not the case, the resulting integrated intensity would be extrinsically determined by this relationship of relative widths of the peak versus the detector's integration width. More importantly, the experimental measurement would not be robust to slight mis-alignments which could miss the peak maximum and sample different portions of the x-ray intensity, giving results largely dependent on the area of integration through the peak.

With that said, the final Gaussian of Eq. 2.30 is approximated to be unity over the area of the last integrand. The equation for the 2-D integrated intensity then becomes

$$\begin{aligned} E(\vec{q}_o) &= \frac{I_o}{\omega}\left(\frac{e}{mc^2}\right)^2 |F(\vec{q}_o)|^2 \frac{1}{\cos(\sigma)\sin(\delta)|k|^2} \frac{(\pi)^{3/2}abnp}{\sqrt{a^2+A^2b^2+B^2n^2+C^2p^2}} \\ &\times \iint d(\Delta q_x)\, d(\Delta q_y) S_1(\Delta q_x, \Delta q_y) S_2(\Delta q_x, \Delta q_y). \end{aligned} \tag{2.31}$$

Another change of variables is made for the specific reciprocal space vectors, as given by the *Laue conditions*,

$$\Delta\vec{q}_1 \cdot \vec{a}_1 = 2\pi h, \text{ and } \Delta\vec{q}_2 \cdot \vec{a}_2 = 2\pi k \tag{2.32}$$

$$d(\Delta q_x)\, d(\Delta q_y) = \frac{(2\pi)^2}{|\vec{a}_1 \times \vec{a}_2|} dh\, dk \tag{2.33}$$

and then,

$$\iint dh\, dk \frac{\sin^2(N_1\pi h)}{\sin^2(\pi h)} \frac{\sin^2(N_2\pi k)}{\sin^2(\pi k)} = N_1 N_2 = \frac{A_{total}}{|\vec{a}_1 \times \vec{a}_2|}, \tag{2.34}$$

where A_{total} is the total surface area illuminated by the scattering measurement.

2.4.4 Results

Combining this last integration and another simplification for the unit cell area, $|\vec{a}_1 \times \vec{a}_2| = \sigma_{cell}$, we have the final solution,

$$E(\vec{q}_o) = \frac{I_o}{\omega}\left(\frac{e}{mc^2}\right)^2 \frac{|F(\vec{q}_o)|^2}{\sigma_{cell}^2} \mathcal{P}(\delta,\gamma) \frac{\lambda^2 A_{total}}{\cos(\sigma)\sin(\delta)} \frac{(\pi)^{3/2}\, a\, b\, n\, p}{\sqrt{a^2 + A^2 b^2 + B^2 n^2 + C^2 p^2}}. \tag{2.35}$$

This equation includes another factor ignored until now, $\mathcal{P}(\delta,\gamma)$, which accounts for the polarization which is an effect from the monochromator Bragg angle $2\Theta_M$ and the sample's scattering angle,

$$\mathcal{P}(\delta,\gamma) = \frac{(\cos(\gamma) + \sin(\gamma)\sin(\delta)\cos(2\Theta_M))^2 + (\cos(\delta)\cos(2\Theta_M))^2}{2}. \tag{2.36}$$

This expression is just a generalization of the standard expression in Int. Table for Crystallography [3] with the addition of the out-of-plane component from the scattering angle γ. Finally, the trigonometric coefficients in the last term of Eq. 2.35 are

$$A = \cos(\gamma)B + \frac{\cos(\delta)\sin(\gamma)}{\sin(\delta)} \tag{2.37}$$

$$B = \frac{-\sin(\sigma)}{\cos(\sigma)\sin(\delta)}\left[\sin(\nu)\hat{q}_x - \cos(\nu)\hat{q}_y\right] \tag{2.38}$$

$$C = \cos(\gamma) \tag{2.39}$$

$$\hat{q}_x = \sin(\delta)\cos(\gamma) \tag{2.40}$$

$$\hat{q}_y = 1 - \cos(\delta)\cos(\gamma). \tag{2.41}$$

2.4.5 Discussion

For comparison, consider the case where the surface normal is held along the z-axis ($\sigma = 0$ and $\nu = 0$) and the out-of-plane scattering angle, γ is zero. The trigonometric coefficients become, $C = 1$, $B = 0$, and $A = 0$, which gives for Equation 2.35

$$E(\vec{q}_o) = I_o \left(\frac{e}{mc^2}\right)^2 \frac{|F(\vec{q}_o)|^2}{\sigma_{cell}^2} \mathcal{P}(\delta) \frac{\lambda^2 A_{total}}{\sin(\delta)} \frac{(\pi)^{3/2}\, b\, n\, p}{\sqrt{1 + \frac{p^2}{a^2}}}. \tag{2.42}$$

This gives the usual Lorentz factor $1/\sin(\delta)$ (where $\delta = 2\theta$). But, the beam angular widths come from the incident beam normalization of πnp (which is just the integration of the incident power, Eq. 2.6.) and the effective integration width along the crystal truncation or reconstruction rod of $\sqrt{\pi}\, b$. Also, the large detector acceptance, as discussed above, means $p \ll a$ and the square root denominator is a small fixed factor which can be ignored [3]. Compared with Robinson's [5] result, the integrated intensity (equation [10]) is exactly the same with

$$\sqrt{\pi}\, b = \frac{\lambda}{2\pi} \Delta Q_3 \tag{2.43}$$

where ΔQ_3 is the portion of the diffracted rod accepted by the detector silt in reciprocal space.

The final integrated intensity calculated in Eq. 2.35 has a complicated Lorentz factor, which is the geometrical sum of various integration widths along the diffracted rod, which change with the sample orientation and the scattering angles.

$$\mathcal{L}(\delta, \gamma) = \frac{1}{\cos(\sigma)\sin(\delta)} \frac{(\pi)^{3/2}\, a\, b\, n\, p}{\sqrt{a^2 + A^2 b^2 + B^2 n^2 + C^2 p^2}} \tag{2.44}$$

Figure 2.7 is an example plot of the value of this new Lorentz factor used for three surface reconstruction rods of Ge(001) (2×1). In Eq. 2.35, the parameters for angular widths in radians are half the full width of the slits divided by the beam path length. For the example figure, the beam parameters are listed in Table 2.1 and the sample's surface normal orientation is with $\sigma = 3.5°$and $\nu = 0$. These are the typical parameters used in the experiments of chapter 3. Also shown in Figure 2.8 is another example plot of the polarization factor for the same diffraction rods. Here there is only one parameter, the monochromator's $2\Theta_M$ angle, while the scattering angles γ ranges from zero to 30° and δ ranges about 10° to 60° for the lowest to highest indexed rod, respectively.

[3] This denominator is the correlation between the in-plane monochromator's divergence and the detector's acceptance as represented by the Gaussians. This term is similar to the result the last integration, if we did not ignored earlier before Eq. 2.31

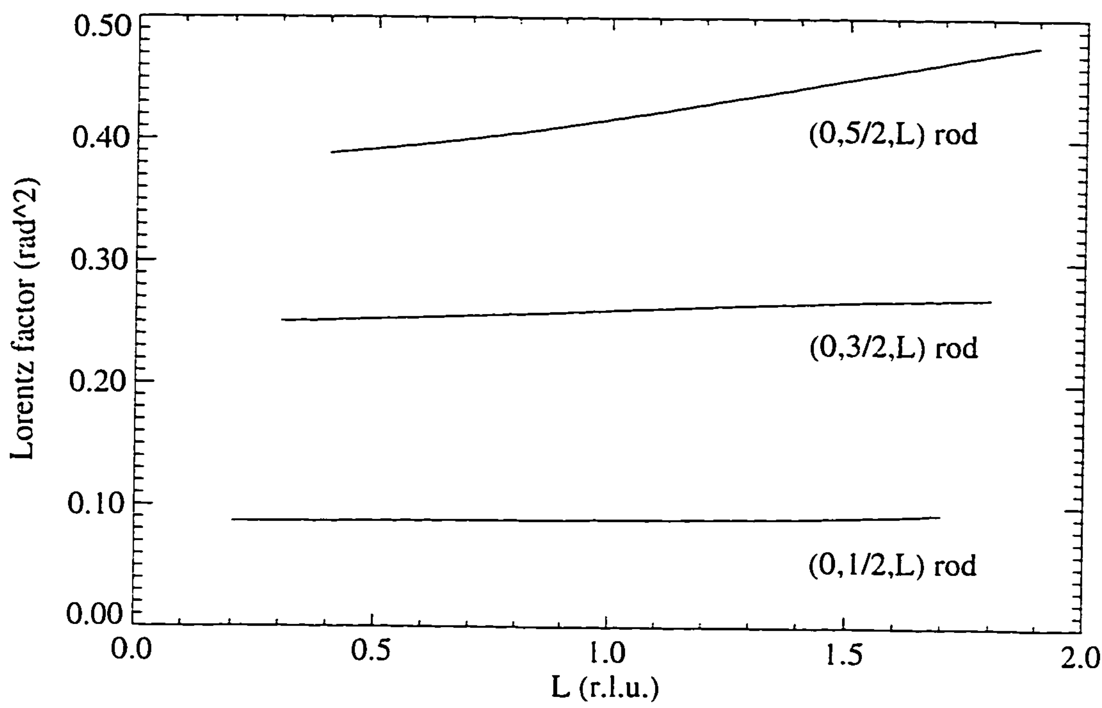

Figure 2.7: The integrated intensity's Lorentz factor as plotted along three different Ge(001) (2×1) surface diffraction rods. The perpendicular momentum transfer, L, is in the reciprocal lattice units for Ge(001).

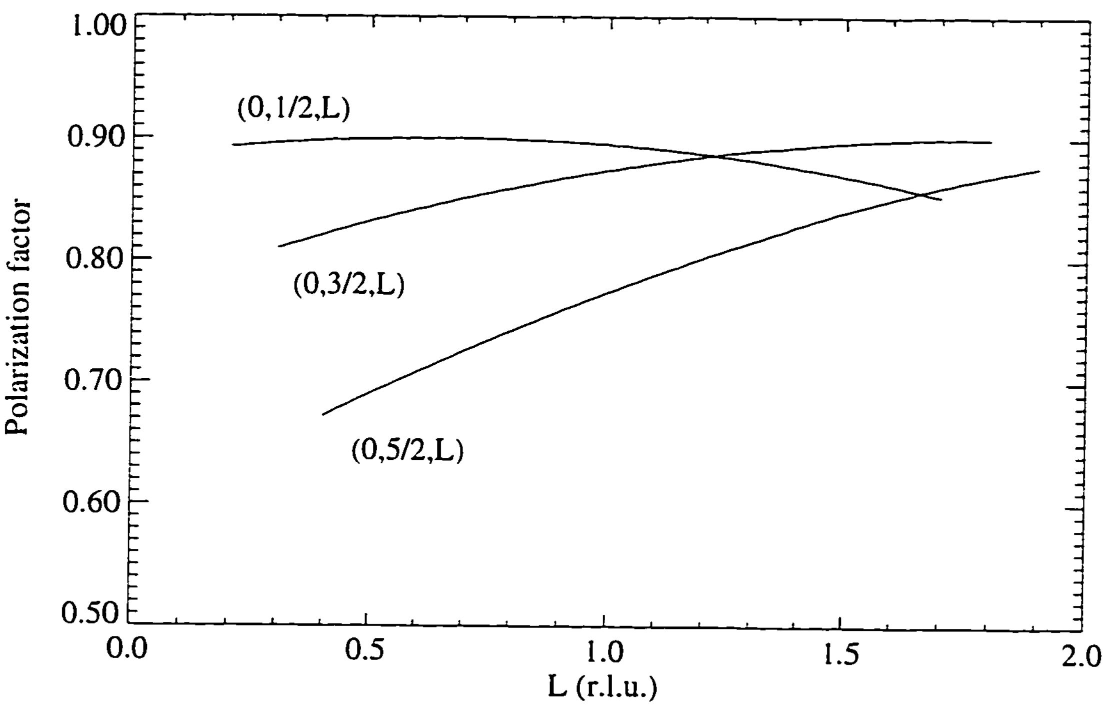

Figure 2.8: The integrated intensity's polarization factor plotted along three Ge(001) (2×1) surface diffraction rods.

Finally, to transform the measured data set of integrated intensities to the values for the structure factors (which are then used to model the crystal structure), we then invert Eq. 2.35 to

$$\frac{|F(\vec{q}_o)|}{\sigma_{cell}} = \sqrt{E(\vec{q}_o)\frac{\mathcal{S}}{A_{total}\mathcal{P}(\delta,\gamma)\mathcal{L}(\delta,\gamma)}} \tag{2.45}$$

Here all the constants, such as the electron cross section, wavelength, and incident intensity are grouped in the arbitrary scaling constant $\mathcal{S}$. The total area A_{total} also changes because the beam profiles across the surface change with in-plane scattering angle δ. This factor has been worked out before by Vlieg and Robinson [5]. For each data point in reciprocal space with its corresponding angles of δ and γ, Eq. 2.45 is used. The various beam widths a, b, n, and p are then parameters to this data set transformation.

This Lorentz and polarization factor formula have been included in our data reduction program *peak*. The exit and incident beam divergences, and the monochromator $2\Theta_M$ angle are menu parameters within program in units of degrees. Similarly, there are menu parameters for the sample area correction factor (exit and incident x-ray beam height and widths, and sample size in unit of millimeters). The program *peak* then sequentially process each scan file from the experiment control program *Super*. The process is to numerically integrate the intensity data of each θ-scan, to give the integrated intensity within respect to the background subtraction and the counting time normalization. Then the program calculates the correction factors (Lorentz, polarization, and sample area) using the scattering and incident

Table 2.1: Incident and exit beam width parameter for the example plot of Lorentz factor shown in Fig. 2.7

		full slit width	radial (mm) distance	full angular width	half angular width (rad)	Lorentz parameter
detector	hor.	8 mm	600	0.3°	0.012	$= a$
	vert.	15 mm	600	1.2°	0.024	$= b$
MCR	hor.	1 mm [a]	350	0.25°	0.005	$= n$
	vert.	12 mm	350	1.2°	0.029	$= p$

[a] No slits define this width, only the size and mosaic of the monochromator crystal.

angles read from the scan file. and the menu parameters. Then using the same equation above, the program calculates the structure factor. This process is repeat on files sequentially for the scan numbers commanded by the user. The results are saved to an output file with the file name suffix ".pk". An information file is also made with a record of the menu parameters, angles, and other information for each of the processed scan files.

2.5 Second harmonic correction

Besides the data reduction and correction factors (Section 2.4) from integration scans to structure factors, an additional minor data correction was needed for the particular experiment on Ge(001) and Si_xGe_{1-x}(001) alloy thin films (Chapter. 3). The correction needed is for second harmonic discrimination leakage. The graphite monochromator reflects primarily the Cu K_α x-rays, but it also reflects integer multiple frequencies from the Bremsstrahlung radiation also coming from the rotating anode. The second harmonic x-rays are a problem for this experiment because their scattering from the sample are at exactly the same angles as some of the ordering and reconstruction peaks. For example, the second harmonic x-rays are reflected by the (111) planes of the Ge substrate at the same angles as the primary x-rays at $(\frac{1}{2}, \frac{1}{2}, \frac{1}{2})$, the position of interest for the SiGe ordered structure. These second harmonic x-rays are usually not a problem with a detector which discriminates between the different photon energies. The scintillation detector used in this experiment is very efficient at this, but the detector and its electronics are not perfect for the high count rates we encountered. Figure 2.9 is an example from the multi-channel analyzer showing the spectrum of pulses measured by the discrimination electronics. The second harmonic reflection, in this case, is the (331) and its intensity is an order of magnitude higher than the primary scattering intensity which coming from the the surface reconstruction of Ge(001). The tail of the second harmonic signal is adding counts to the primary discrimination window. The data was corrected for this

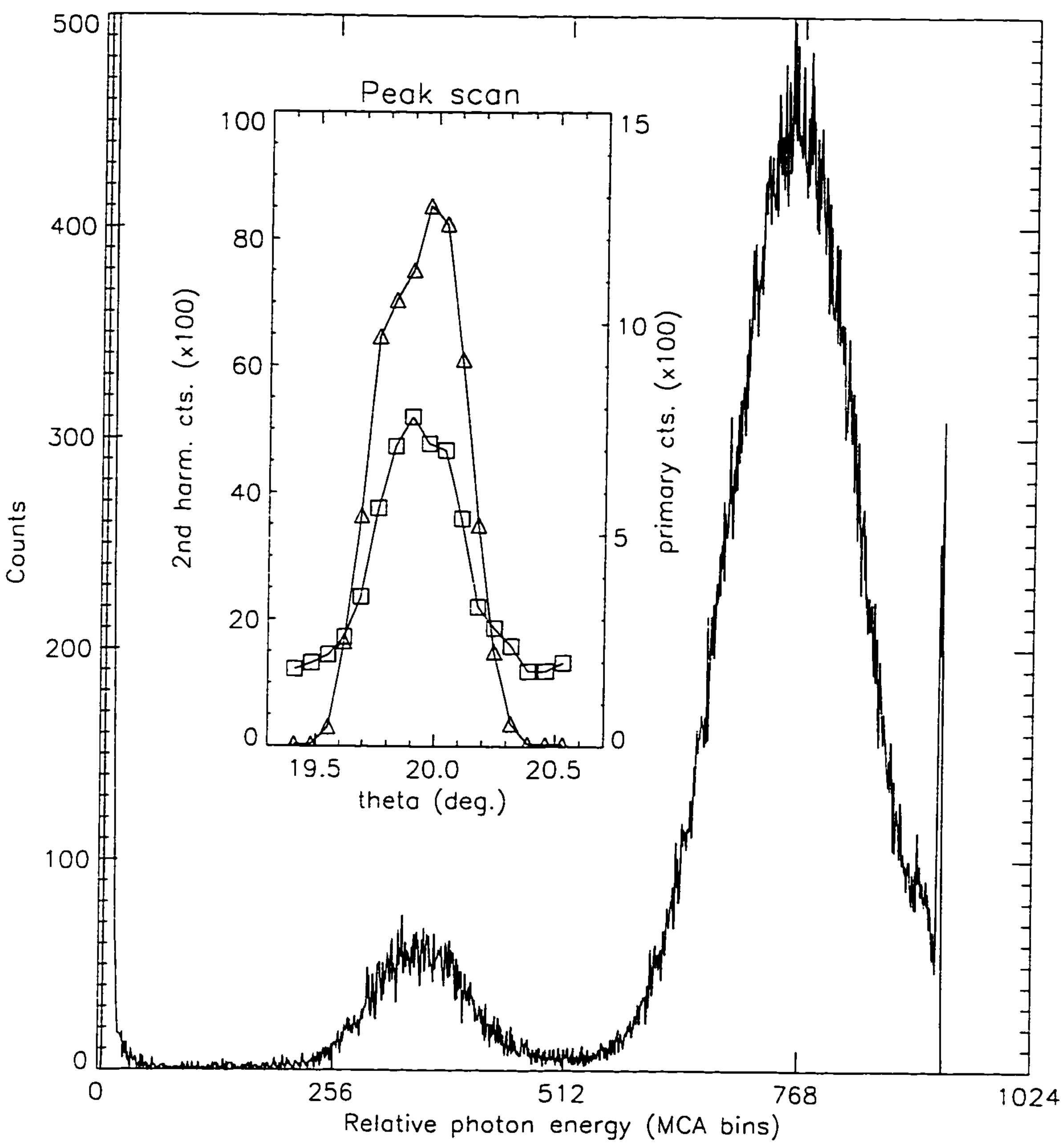

Figure 2.9: Example the of scintillation detector's discrimination between primary and second harmonic x-rays as measured by the multi-channel analyzer (MCA). In this case the harmonic x-rays are from reflection (331) while the primary is ($30\frac{1}{2}$) in surface units. The inner plot shows the usual theta scan for integrations where both the primary (squares) and second harmonic (triangles) counts are measured. The spectrum was taken at the maximum of the this scan.

cross-over from the tails of the distribution by subtracting an amount proportional to the second harmonic intensity. The window plot within Fig. 2.9 shows the integrating scan where both the primary and second harmonic intensity were measured. The proportion factor for the subtraction was measured to be 6×10^{-5} (i.e. 6 counts are subtracted from the primary x-rays for every 10,000 counts of the harmonic x-rays). Alternatively, it was simpler in the data analysis to correct the structure factors by subtracting $\sqrt{6 \times 10^{-5}} = 0.008$ of the second harmonic structure factor amplitude.

Chapter 3

SiGe alloy surface and thin films

3.1 Introduction

Silicon Germanium alloy is an important example of a semiconductor alloy and understanding its phenomena is increasingly valuable as alloys become used in electronic devices today. Part of that understanding is the material's atomic crystal structure, which is then the basis for understanding other properties, such as the electronic band structure, defects, and surface growth morphologies. Silicon and Germanium (001) surfaces, including their alloy, have the dimer (2×1) reconstruction. This reconstruction is believed to cause the growth of compositionally ordered films of SiGe(001). This correlation (or ordering) of Si and Ge atoms on the diamond lattice sites has gained considerable attention, since the material's adjustable band gap is of technological importance. SiGe alloy films were at first assumed to be the same as the bulk solid, a completely random solid solution of both elements with the diamond structure. But, as discussed in Chapter 1, the structure of the compositional order is a meta-stable locally-strain RS2 structure with Ge and Si rich bi-layers along the (111) planes (Fig. 1.2). The ordering of Si_xGe_{1-x} is the focus of this chapter and the experiment performed to detail this structure during the growth process by MBE.

This chapter is organized into three sections. The first section provides a description of the experiments for the sample MBE growth and x-ray diffraction measurements. The second section provides the results, organized by: 1) the results for pure Ge(001) (2×1) reconstruction, 2) the thinnest (8 ML) $Si_{0.5}Ge_{0.5}$ data and resulting model, 3) the Fourier difference map result of the same film, and 4) result of varying film thicknesses and growth temperatures. The final section details the conclusions and some discussion of there results.

3.2 Experiment

The observed compositional order in $Si_xGe_{1-x}(001)$ alloys has been clearly connected to the (2×1) reconstruction of the growth interface. For both Si and Ge (001) (2×1) surfaces, the structure has been accurately determined by surface x-ray diffraction [29, 31]. The experiment we have performed is a generalization of this, designed is to directly observe the ordering within the reconstruction. Surface x-ray diffraction has also been used to observe surface compositional ordering in metal alloys of Cu_3Au and FeAl [43]. A review of this technique is in Ref. [6], but the basic idea is to measure the two dimensional scattering from the periodicity of the surface or truncation of the bulk crystal. Unlike bulk diffraction, in 2D diffraction one of the three Laue conditions is relaxed making the diffraction intensity continuous and perpendicular to the surface (called rods). A surface reconstruction has different periodicity than the bulk and so reconstruction rods are separated from the bulk crystal truncation rods. This allows one to measure an intensity coming only from the surface if it has a reconstruction. The intensity along the various rods is measured and then compared to model of the surface structure, based on the kinematical diffraction theory.

3.2.1 Sample Growth

The samples of Si_xGe_{1-x} thin films were grown on Ge(001) substrates. The substrates were cleaned and prepared by rinsing and sonication with ultra-pure water to dissolve the native oxide and contaminants, then placed in a ultra-violet lamp box for ozone exposure [44]. The ozone is for the rapid regrowth of the germanium oxide and is believed to oxidize any organic contaminants, which combined with the UV radiation, volatilize the contaminants for removal from the surface. This process of ultra-pure water and UV/ozone exposure was repeated several times with the last step being the UV/ozone, performed before the substrate is indium bonded to a molybdenum sample holder. The sample was then immediately introduced into the vacuum system through a loading vacuum-interlock chamber. After pumping down, the substrate and sample holder are transferred into the growth chamber. The epitaxial growth chamber was a Perkin-Elmer 425 equipped with dual electron-beam evaporation system containing Si and Ge sources, with a base pressure of 6×10^{-11} Torr. Once inside the MBE chamber, the sample was slowly heated to desorb any remaining gases. The substrate temperature was increased while the chamber pressure was maintained below 5×10^{-10} Torr. At about 450° C the oxide was removed by thermal desorption, which was confirmed by reflection high-energy electron diffraction (RHEED) showing the (2×1) pattern for the pure reconstructed surface of Ge(001). The final preparation step was the homoepitaxial growth of a germanium buffer layer, usually 1000 Å thick at a deposition rate of 1 Å/s and a substrate temperature of 370°C [45, 46].

The deposition rate from either of the electron-beam evaporation sources was controlled by active feedback obtained from an Electron Ionization Emission Spectroscopy (EIES) flux monitor. The total deposition thickness was also monitored by a quartz crystal oscillator. This and the EIES monitor are part of the Inficon Sentinel III deposition controller. For the growth of the $Si_{0.5}Ge_{0.5}$ alloy layers the EIES monitor allows one to actively control the Si and Ge fluxes individually, to maintain the desired composition of 50%-50%. The final

composition of the films where later confirmed by Rutherford backscattering spectroscopy (RBS) and depth profile Auger electron spectroscopy (AES). AES confirmed the composition to within 10%, while the RBS shows some Si rich stoichiometry 57%-43%. The individual element deposition rates where also confirmed by *ex situ* profilometry on edges of test films, both 1.0±0.3 μm thick. Later, one measurement of the alloy film thickness by x-ray reflectivity found a larger than nominal growth thickness by 20%, consistent with the possible Si rich stoichiometry [47].

3.2.2 X-ray diffraction measurements

Once the sample thin film was prepared, it was then transferred through an ultra-high vacuum transport tube from the MBE chamber to the x-ray chamber for the scattering measurements. The base pressure of this analysis chamber was 3×10^{-10} Torr, which allowed the measurement to last beyond 48 hours before the sample surface became contaminated. Contamination was characterized by a decrease in the scattering intensity from the (2×1) surface. One sample was later transferred to another analysis chamber for x-ray photoemission spectroscopy (XPS) which confirmed the minor surface contamination by carbon and oxygen.

The x-ray source is a 18kW copper rotating anode generator with a highly-oriented pyrolytic graphite (HOPG) curved crystal to select the Cu K_α radiation (λ = 1.54 Å). The curvature of the monochromator focused the x-rays to a 1×1 mm point at the sample position within the UHV chamber. More details of this x-ray analysis chamber are present in Chapter 2. Vertical slits were used to control the monochromator's focusing. Horizontal slits placed half way to the sample, defined and collimated the incident x-ray beam. The spectral lines α_1 and α_2 were not resolved. This system provided a large flux of x-rays at the expense of resolution. The beam divergence from the HOPG monochromator, perpendicular to the focusing direction, was 0.30°. The detector was placed 630 mm from the sample (center of

rotation). At half that distance was a Soller slit box which collimated the diffracted beam in the direction perpendicular to focusing direction (i.e. in the horizontal scattering plane). The final optical elements were vertical and horizontal slits in front of the detector for definition of the exit beam size and/or view of the sample.

First, the sample was aligned by finding and centering on the Bragg diffraction peaks of the substrate. Then the diffraction intensity of the (2×1) rods was measured for each of the samples. Figure 3.1 is picture of reciprocal space along the ⟨110⟩ plane, showing the relative locations of diffraction intensity from the sample. The dark circles represent the bulk Bragg peaks from the substrate and the SiGe thin film, with the open circles showing the missing fcc type peaks. The crystal truncation rods are the continuous intensity lines shown between the bulk peaks. The long range ordered domains within the SiGe films are represented by the grey circles, the first being half the distance to the (111) bulk peak. The superstructure peaks shown, represent the superimposed diffraction from all the domains of the ordering. The surface reconstruction rods, represented by the lines between, also run through the ordering peaks. The dimers and their double periodicity give rise to the surface rods, half way between the bulk crystal truncation rods. The doubling period of the ordering in the (111) bi-layers makes the surface rods overlap the ordering peaks.

The experiments measured the intensity only along the surface reconstruction rods, allowing us to be sensitive only to the surface and ordering structures. For each point along the rod, a θ scan was measured which makes a cross-section of the rod giving the integrated intensity. These scans are just the integrated intensity measurement described in Section 2.4. The length of the rods measurable was not as long as shown in Fig. 3.1, but up to about $L = 1.9$, limited by the angular range of the instrument.

The common cubic indexes of hkl to describe the reflections from silicon or germanium crystals are related to surface indexes, HKL, the ones used to describe the diffraction in

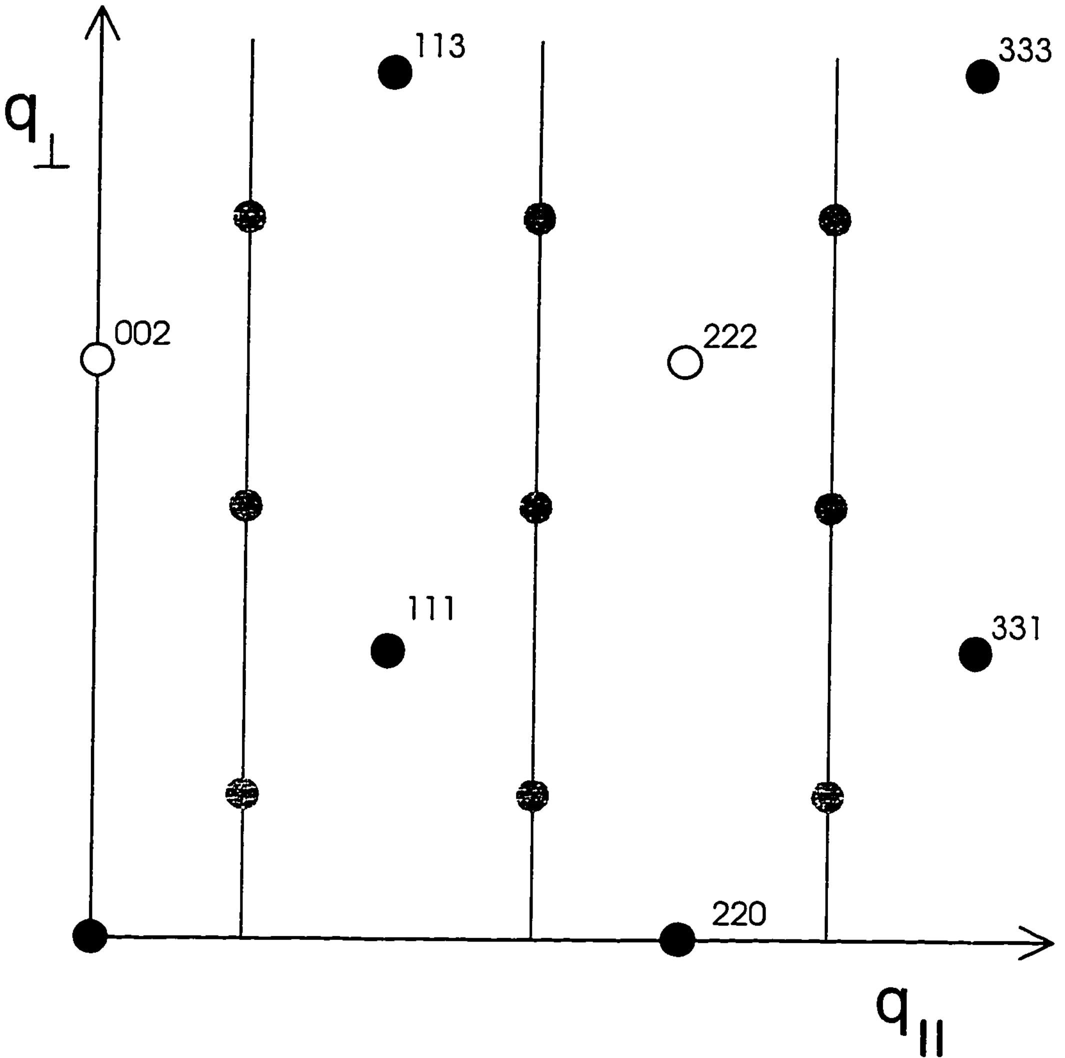

Figure 3.1: Sketch of reciprocal space [110] plane for Si_xGe_{1-x} (001) thin film. The solid circles are bulk Bragg peaks and the crystal truncation rods between them. The grey solid circles are the ordering peaks and the reconstruction rods along through them.

this experiment, by the transformation here:

$$\begin{pmatrix} H \\ K \\ L \end{pmatrix} = \begin{pmatrix} \frac{1}{2} & \frac{1}{2} & 0 \\ -\frac{1}{2} & \frac{1}{2} & 0 \\ 0 & 0 & 1 \end{pmatrix} \begin{pmatrix} h \\ k \\ l \end{pmatrix} . \tag{3.1}$$

The surface coordinate frame is chosen so the momentum transfer perpendicular to the surface is along one of the principal axes, usually being L. Using this, the reflections (004), (111), and $(\bar{1},1,1)$ become in surface notation (004), (101), and (011), respectively. For the dimer (2×1) reconstruction, is the surface unit cell is doubled along one in-plane direction. Correspondingly, the reciprocal space index becomes a multiple of a half integers in that direction. So, the reconstruction rods appear at $(\frac{1}{2},0,L)$, $(\frac{3}{2},0,L)$, $(\frac{1}{2},1,L)$, etc.

The presence of the reconstruction also means the (001) surface breaks its 4-fold rotational symmetry. Yet, because the surface is equally covered by two domains of the reconstruction oriented 90° apart, the reconstruction rods occur in the half-order positions both along the surface H and K directions. In the data reduction, the diffraction rods from both domains are combined together make one data set. The measured half-order rods for the various samples were limited to one half quadrant, the smallest asymmetric volume, and to a maximum in-plane momentum transfer of the $(\frac{5}{2},0,L)$ rod. Test positions were measured to confirm that the symmetry and the related intensities were equivalent.

The final detail is the correction for the leakage of second harmonics, as described in Section 2.5. The multi-channel analyzer output from the scintillation detector was used to correct the imperfect discrimination between the primary scattered x-rays and second harmonic x-rays. The harmonic counting rate was multiplied by 6×10^{-5} and then subtracted from the fundamental. This correction was found to change only structure factors near and at $L = 0.5$ or 1.5 (because $(\frac{1}{2}\frac{1}{2}\frac{1}{2})$ measures also the x-rays with double the energy scattered by the (111) reflection.) The correction ranged from 5% for the larger structure factors, up to 20% for the weakest data points. The weakest primary intensities have the largest corrections

because of the nearly constant second harmonic scattering.

3.3 Results

3.3.1 Ge(001) buffer layer surface

The first experiment performed was to measure the x-ray scattering from the pure Ge surface for later comparison with the SiGe film surfaces. As mentioned above, the Ge(001) substrates were initially grown with a 1000Å buffer layer to obtain the well ordered (2×1) surface. This provided the starting surface for the subsequent growth of Si_xGe_{1-x} thin films. But prior that, the substrates were transferred to the x-ray chamber for measurement of their surface structure.

The structure of the Ge(001) (2×1) surface has been determined before by x-ray diffraction by two groups [29, 30]. The Rossman *et al.* experiment [29] was similar to ours, in that they used a rotating anode x-ray source, but the latest measurement of Torrelles *et al.* [30] at a synchrotron radiation source provided a greater accuracy to the structure, which came mostly from the larger range of perpendicular momentum transfer, L, that could be reached in their experiment. The results from our *in-situ* surface x-ray diffraction experiment on the same Ge(001) surface is plotted in Figure 3.2. This figure shows the complete data set: seven reconstruction rods. Each rod is labeled at the top by its H ($\times$ 2) and K indexes. Each data point for the measured structure factor results from an integration scan through a cross-section of the rod. To sample the continuous rod intensity, the scans were made every $\Delta L = 0.1$. The solid line represents the structure factors calculated for the model by Torrelles *et al.* This model needs only one free parameter to fit the data, which is an over-all scaling factor. This is because we did not attempt to make an absolute measurement. The Torrelles' model fits very well to the data, giving a $\chi^2 = 1.52$. This confirms not only that the published Ge(001) model is correct, but also that our instrument and data analysis is working

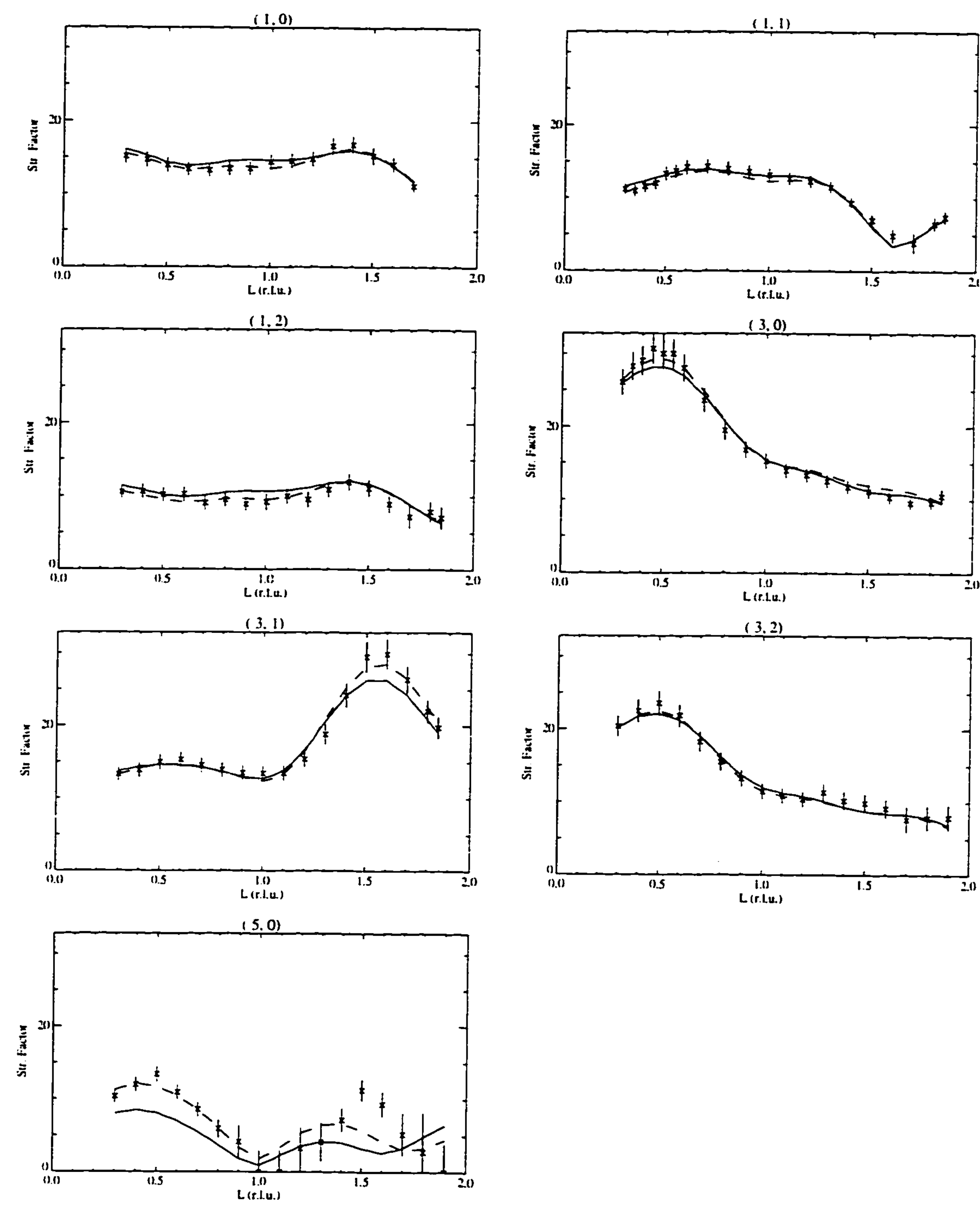

Figure 3.2: Measured structure factors versus index L for seven reconstruction rods. The vertical line of each data point represents its uncertainty. The continuous lines are the curves calculated from Torrelles' *et al.* model. The dashed lines are curves calculated for our model, fit to this data. The H ($\times$ 2) and K indices are labeled at the top of the figure.

properly, which was important because it was the first experiment for our new instrument. A summary of the main structural features of this model and the next is represented in Figure 3.3.

An important detail of the model is that the dimer has an asymmetric tilt angle, but both directions of the tilting are included with equal weight in the amplitude scattering. This disordered buckling dimer structure, proposed by Rossman *al.* [29] allows one to model the changing dimer angle across the actual surface. This dimer tilting is believed to be dynamic in nature, because at lower temperatures there is a transition to another reconstruction with the same dimers but ordered in the tilt directions along the dimer rows. This low temperature c(4×2) reconstruction of the Ge(001) surface is described in Ref. [48]. Another important detail of the Ge(001) (2×1) model is the displacement of atoms down to the eight layer below the surface dimer. This result shows the propagation of strain associated with the strong bond bending in forming the dimer reconstruction.

Next, we tried fitting data by adjusting the same displacement and Debye-Waller parameters, starting from Torrelles' parameters. The result is also plotted in Fig. 3.2 as the dashed curves. Our model did decrease χ^2 to 0.61. The structural parameters for our fit are listed next to Torrelles' model in Table 3.1. Our model fits the data closer, especially the peaks in rods (3/2,0,L) and (3/2,1,L), but it gives bond lengths which are slightly farther from the bulk Germanium bond length of 2.45 Å. Additionally, with the resulting χ^2 being below 1.0, this could mean our model may be fitting the data beyond its uncertainty, but may also imply a discrepancy in the error estimate of the data. Table 3.2 lists the dimer bond length and angle of inclination for our best fit model, the two previous experiments, and other results from Si(001).

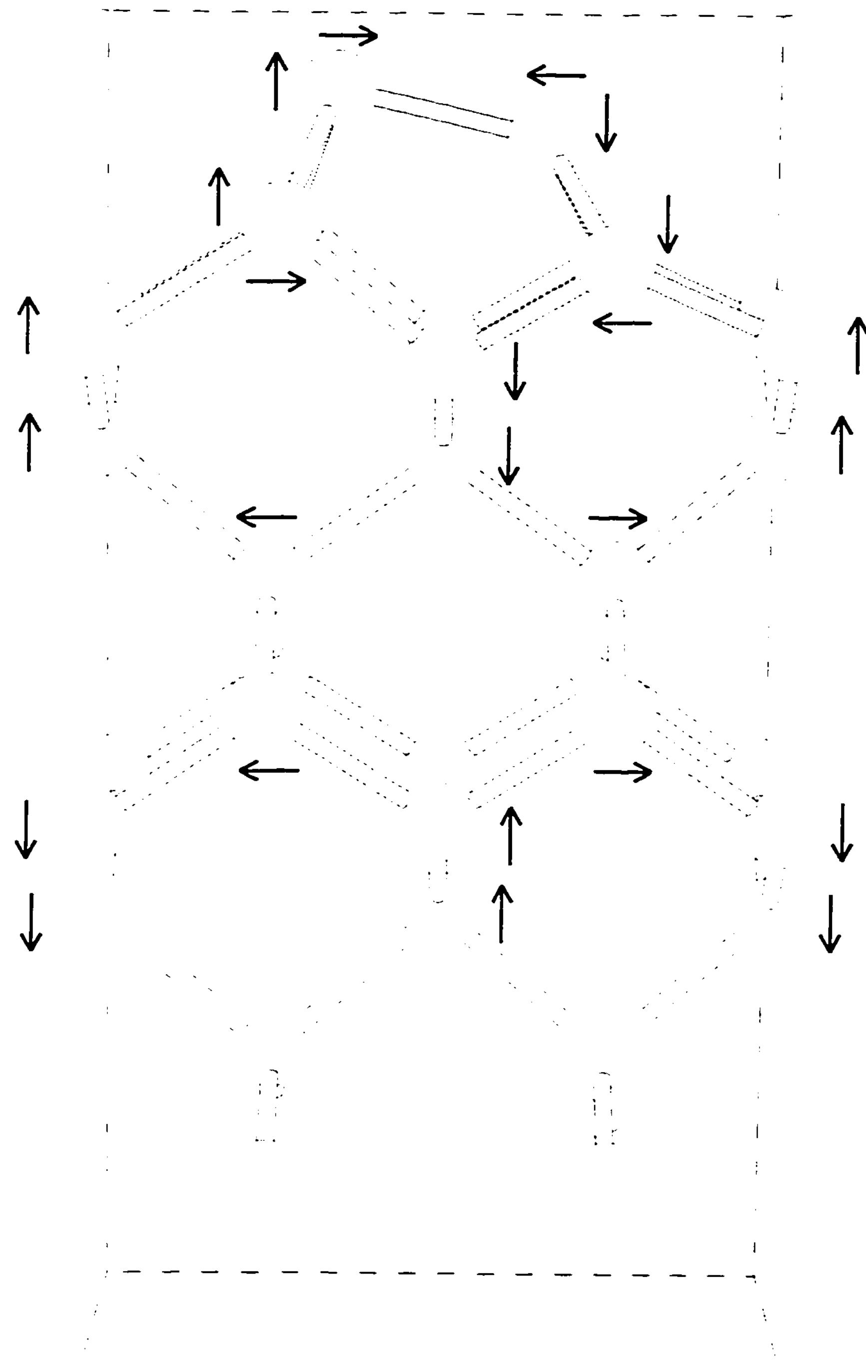

Figure 3.3: Structural model of Ge(001) (2×1) reconstruction with relative displacements of the atoms from their ideal bulk positions. Not shown is the symmetrically equivalent dimer and second layer atoms with the opposite tilt. This structure and its mirror image are combined with equal probability to form the disorder model for the dimer tilting.

Table 3.1: Atomic positions for best fit model and Torrelles *at el.* model [30] to the Ge(001) 2×1 data set shown in Fig. 3.2. The coordinates are normalized to the (2×1) unit cell, i.e. a = 8.000 Å, $b = a/2$, and $c = a_o$ = 5.658Å. Asterisks denote fixed coordinates. The numbers in parentheses are calculated uncertainities in the last digit.

	Best fit model				Torrelles model			
Atom	x	y	z	B(Å)	x	y	z	B(Å)
1	0.308(4)	0.5*	0.027(5)	1.9(2)	0.323	0.5*	0.042	1.8 [a]
2	0.633(2)	0.5*	-0.070(6)		0.630	0.5*	-0.080	
3	0.274(1)	0.0*	-0.245(5)	0.7(5)	0.274	0.0*	-0.235	0.7
4	0.750(1)	0.0*	-0.26(13)		0.749	0.0*	-0.269	
5	0.0*	0.0*	-0.479(2)	0.50 [b]	0.0*	0.0*	-0.479	0.6
6	0.5*	0.0*	-0.517(2)		0.5*	0.0*	-0.517	
7	0.0*	0.5*	-0.732(2)		0.0*	0.5*	-0.730	0.50 [b]
8	0.5*	0.5*	-0.760(2)		0.5*	0.5*	-0.760	
9	0.2438(4)	0.5*	-1.00(2)		0.245	0.5*	-0.999	
10	0.7562(4)	0.5*	-1.00(2)		0.755	0.5*	-0.999	
11	0.2472(4)	0.0*	-1.25(3)		0.248	0.0*	-1.247	
12	0.7528(4)	0.0*	-1.25(3)		0.752	0.0*	-1.247	
13	0.0*	0.0*	-1.503(2)		0.0*	0.0*	-1.504	
14	0.5*	0.0*	-1.491(2)		0.5*	0.0*	-1.492	
15	0.0*	0.5*	-1.754(2)		0.0*	0.5*	-1.751	
16	0.5*	0.5*	-1.747(2)		0.5*	0.5*	-1.747	

[a] Approximate isotropic Debye-Waller factor
[b] Fixed to known bulk factor

Table 3.2: Ge(001) dimer bond length and angle of inclination from our best fit model and models by others. The last two entries are the same parameters for Si(001) dimer reconstruction for comparison.

Model & Ref.	Bond length	Angle
Our best fit	2.66±0.04 Å	12±3°
Torrelles *et al.*[30]	2.55±0.01 Å	15.6±0.6°
Rossman *et al.*[29]	2.44±0.04 Å	17±4°
Si(001): Takahashi *et al.* [31]	2.37±0.06 Å	20±3°
Si(001): Felici *et al.* [32]	2.67±0.07 Å	20±3°

3.3.2 $Si_{0.5}Ge_{0.5}(001)$ very thin film

This section will describe the results for $Si_{0.5}Ge_{0.5}$ thin films at their initial stage of growth. The film was deposited on a 1000 Å buffer layer at 400°C with a thickness of only 8 monolayers (ML). Just as with the Ge(001) experiment, the sample was transferred after growth to the x-ray chamber for diffraction measurements with exactly the same optical configuration. The resulting data set from the very thin film of $Si_{0.5}Ge_{0.5}$ is shown in Figure 3.4, which also shows, for comparison, the fit curves for the pure Ge(001) data. This figure shows the over-all decrease in the structure factors from the alloying of some silicon on the surface. The form factor of Si is less than that of Ge because it has fewer electrons, so scatters fewer x-rays. The surface of this thin film has the similar dimer reconstruction but now it consists of an alloy of Ge and Si atoms. If the alloyed atoms were exactly in the same positions as the Ge(001) reconstruction, the structure factors would be the same as Ge(001), except for the over-all linear decrease from the decreased atomic scattering factor for the alloy. This is clearly not the result shown in Fig. 3.4. There are different modulations and additional peaks for some of the rods. The largest features are still present because the dimers and sub-surface displacements are still an important component of the structure. Another important detail is that the additional peaks occur at or near the positions expected for the alloy (111) bi-layer ordering, i.e. at rod positions of $L = \frac{1}{2}$ and $\frac{3}{2}$ as noted in Fig. 3.1. These initial details confirm that there is some additional structure or order in the $Si_{0.5}Ge_{0.5}$ thin film, beyond the dimer reconstruction.

To quantify the structure, another least-squares refinement was tried. The best model with reasonable bond length and atomic densities, and fit the structure factors well is shown in Figure 3.5.

The solid curves calculated from the model matched most of the features of the data and gave $\chi^2 = 2.1$. Our fit model contained parameters of two types: composition at differing lattice positions, and displacements of the near surface atoms. First, the composition of the

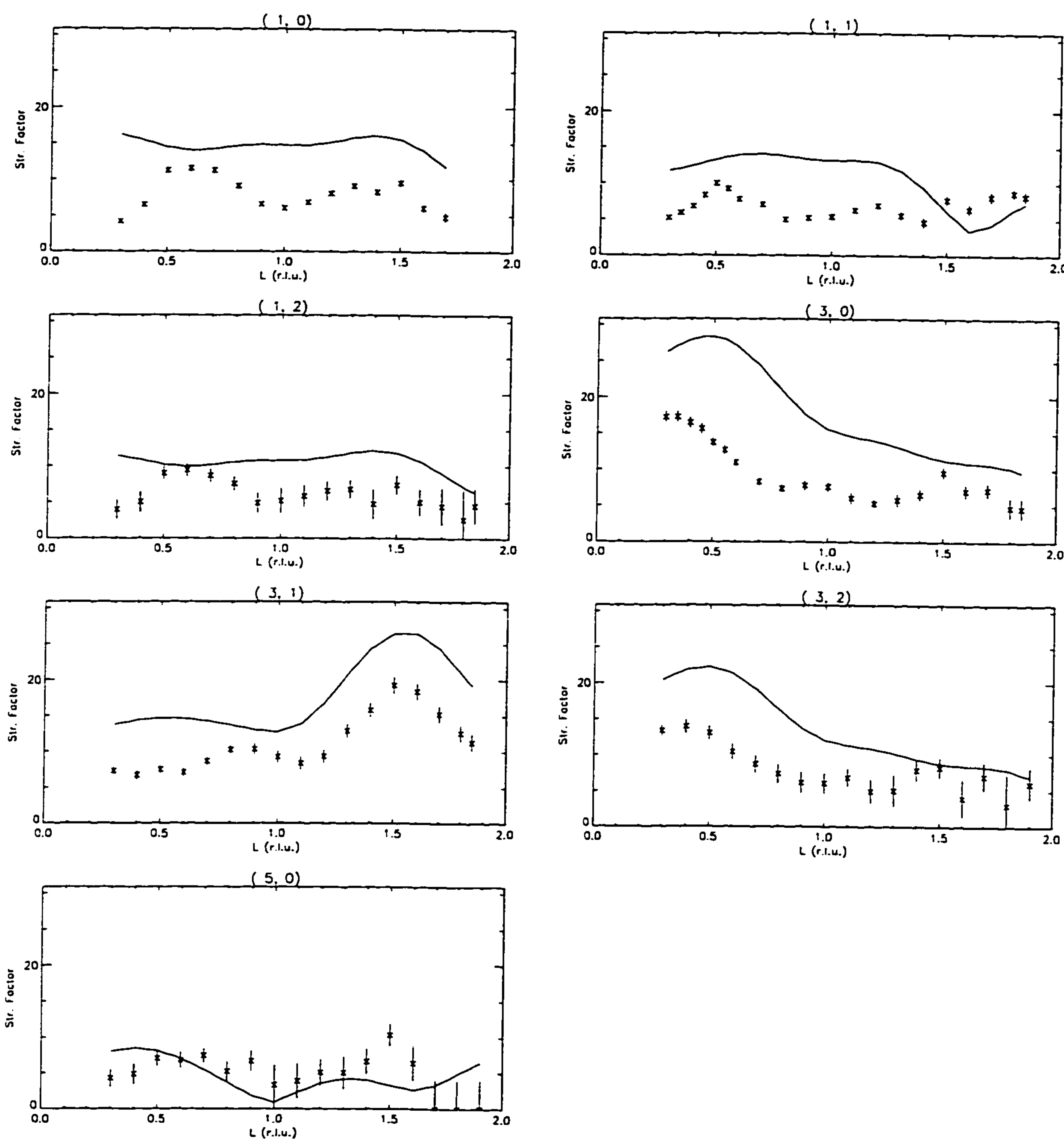

Figure 3.4: Measured structure factors from $Si_{0.5}Ge_{0.5}(001)$ 8 ML thin film versus index L for seven reconstruction rods. The solid curves are the structure factors from Ge(001) for comparison

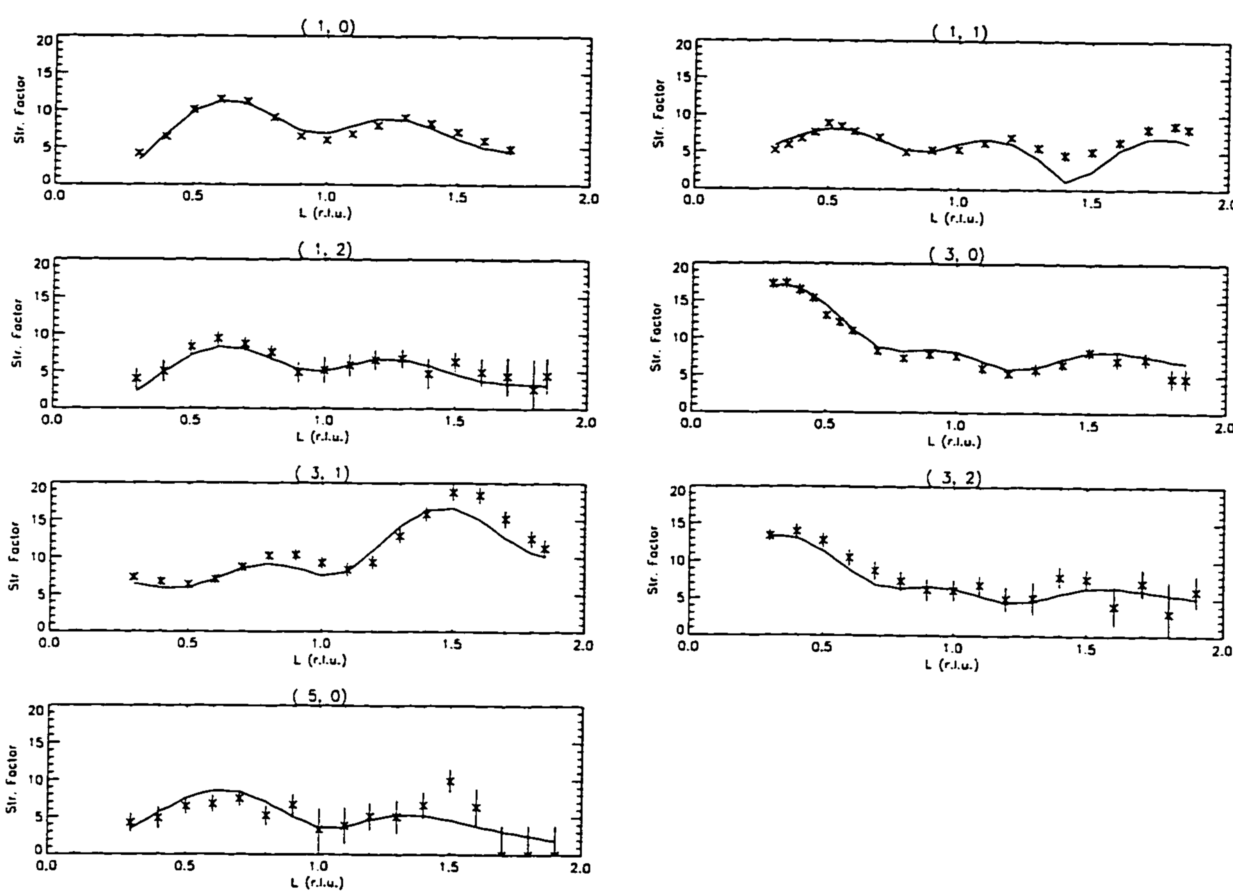

Figure 3.5: Measured structure factors from $Si_{0.5}Ge_{0.5}(001)$ 8 ML thin film versus index L for seven reconstruction rods. The solid curves are calculated from our model.

dimer and second layer atomic sites were allowed to adopt free values. But, both the left and right positions (Fig. 3.3) were constrained to be the same. These top-most sites were free in composition to model the possibility of Ge segregation. Next, the average composition within each of the layers 3 through 8 were constrained to the average composition from the growth condition, i.e. the bulk film composition. Since each layer of $Si_{0.5}Ge_{0.5}$ within the unit cell has only two non-equivalent atoms, the composition is then distributed between these two positions, represented by p, an order parameter within each layer. For example, if $p = 0$ then both positions will have the bulk composition. If $p = 1$ or -1 then one lattice position has only Si and the other only Ge, meaning the layer is completely ordered. The sign definition identifies a specific site. For the values between these two extremes, p is the order parameter for a specific layer where the alloy composition at each different site can be modulated about the film's average. This definition is similar to that used by Kelires and Tersoff [28].

Another constraint placed on the model is that the bi-layers (layers 3 and 4, layers 7 and 8) each have the same order parameter. This ordering of bi-layers is predicted from the bulk ordering structure RS2 (Fig. 1.2) determined by Tischler *et al.* [22].

But, in layers 5 and 6, the lateral ordering within each layer cannot be resolved, just as in the case for the dimers above. A vertical mirror plane through the center of the unit cell is assumed from the symmetry of the data set. Therefore, the atoms within each of these layer were constrained to the film's average composition. This does not mean these layers do not have any ordering. It means that the measured structure factors combined the scattering from both possible domains of (111) and ($\bar{1}\bar{1}1$), and therefore could not resolve the possible ordering within these layer. This is analogous to the case in earlier experiments on Ge(001) (2×1) which could not resolve between a symmetric dimer model and disordered dimers with asymmetric buckling [29].

Besides the density parameters, the model also included displacement parameters. Only the atoms in layers 1 and 2, the dimer and second layer atoms, were allowed move in the

x and z directions during the refinement. All other atoms were fixed at the positions from Torrelles model for the Ge(001) (2×1) structure. These few displacement parameters helped limit the results to the most meaningful model. The result of the refinement with this model is shown in Figure 3.6. The most important conclusion is the ordering in layers 3 and 4 under the dimer and the additional order in layers 7 and 8. The deeper ordering is in the correct registry for either the (111) or ($\bar{1}\bar{1}1$) bilayer ordering. This confirms the structure from experiments on thicker and relaxed $Si_{0.5}Ge_{0.5}$ films (described in our measurements below) by Tischler *et al.*[22]. The resulting structure also has some Ge segregation: the dimers have a higher germanium composition than the bulk film.

Another result is the increased bond length of the dimers to 2.69±0.15 Å. In general, in the incorporation of Si in the Ge lattice, one expects the average bonds to shorten. Some of the bonds from the dimers to second layer atoms and the bonds from second to the third layer did shorten. But this dimer bond length is in agreement within uncertainty with other measurements [32, 30]

Our result agrees with the prediction of Kelires and Tersoff [28] that the Ge compositions in layers 3 and 4 should be 60% at 400°C (our growth temperature). Their study also predicted a large segregation with a dimer Ge composition of 90%. Our model has some increase in Ge segregation, but not quite this amount. Their equilibrium model also predicted some ordering one layer deeper (7), but only to 53% Ge. The resulting compositional order in layers 7 and 8 is in agreement with model of LeGoues *et al.* In this model, these deeper layers are ordered as prior surface layers which are then covered by later deposition.

3.3.3 Electron Density and Difference Map

An alternative analysis of the $Si_{0.5}Ge_{0.5}$ thin film data is by the direct method of Fourier difference maps. The goal is to use the structure factors by an inverse Fourier transformation to directly show the difference between the known Ge(001) (2×1) structure and the unknown

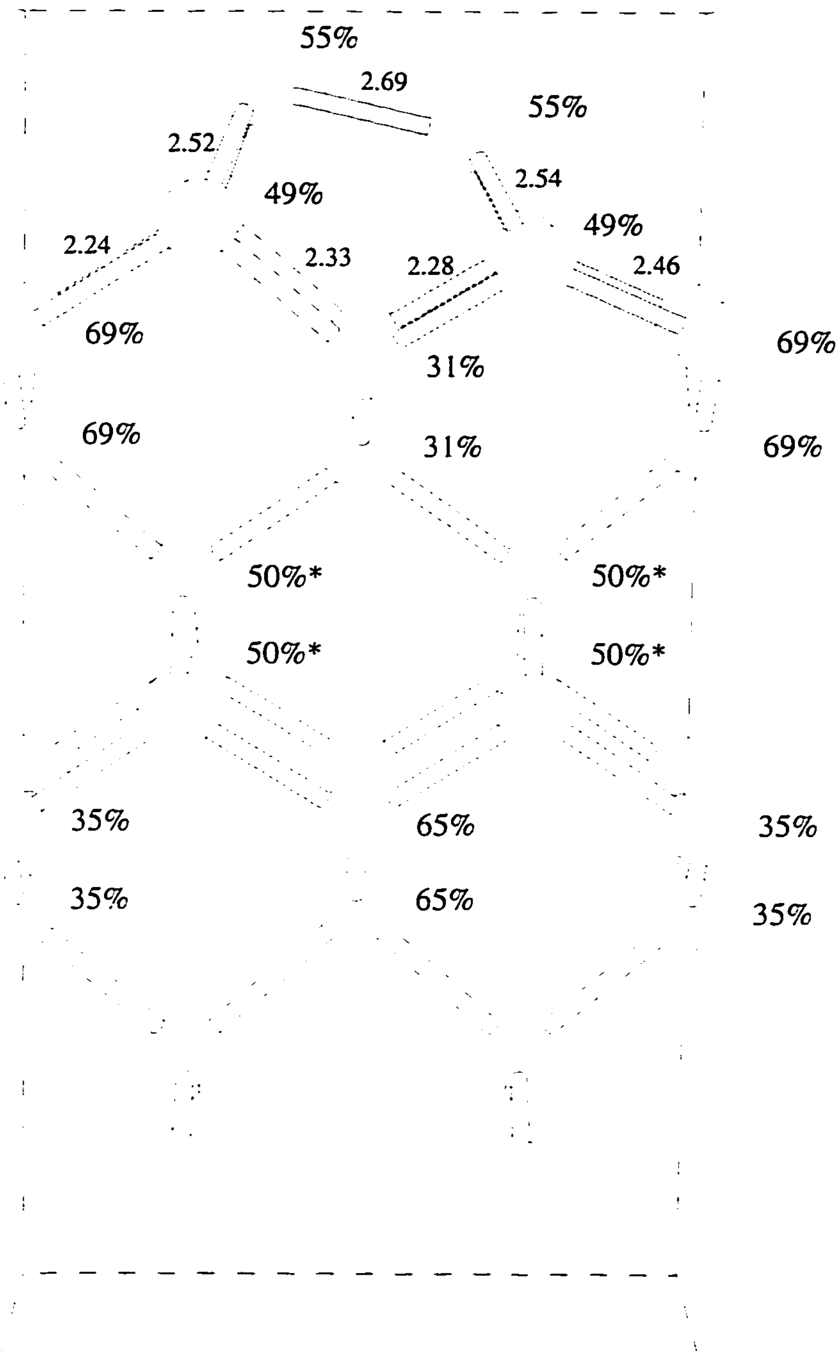

Figure 3.6: Resulting model of the $Si_{0.5}Ge_{0.5}(001)$ 8 ML thick film structure. The composition percentages for Ge are listed for each atomic position. The bond lengths shown (in Å) are the only ones terminated by the least-squares refinement; all others were fixed to Torrelles' model for Ge(001). The uncertainties for the compositions of the first and second layer are ±3% and ±5%, respectively. The rest have uncertainty of ±1%

$Si_{0.5}Ge_{0.5}$ structure. The first detail is to construct the electron density map from the Ge(001) structure factors. Besides the amplitude, the inverse Fourier transformation also requires the phase for each data point. The phases can be calculated from a known model, which in this case is the model of Torrelles *et. al* for Ge(001) (2×1) surface.

Now the resulting electron density map of the unit cell from the surface rods is not itself a direct picture of the atoms. Because the crystal truncation rod and Bragg peaks are not included in the inverse transform, only the "reconstruction density" is given. This is the difference between the ideal unreconstructed surface and the reconstructed one. By transforming only the odd half-integer rods to the doubled (2×1) surface unit, the density pattern is also constrained to have anti-symmetric density. As shown in Figure 3.7, the density map from Ge(001) has equal negative and positive peaks. In fact these features show how the Ge atoms move, i.e. from bulk (symmetric) position to the reconstructed (non-symmetric) position with the anti-symmetric component shown here. The figure shows for the two different y-planes the ideal bulk lattice position as solid circles. As expected, the strongest feature is the dimer, which is cut off in this scale to show the displacements in the deeper layers.

For the $Si_{0.5}Ge_{0.5}$ structure similarly, the inverse Fourier transformation of only the odd half-index rods will give the anti-symmetric density component. This shows where the atoms move from their ideal positions and, (the part of interest) where the chemical composition is ordered. But the phases for $Si_{0.5}Ge_{0.5}$ are of some question. We wish to test the model above, and using phases calculated from it may bias the resulting density map. The alternative is to calculate the Fourier difference map between the $Si_{0.5}Ge_{0.5}$ density and the Ge(001) structure for which the phases are known. The difference map is a common method in crystallography to locate missing components in atomic models[6].

The structure factors and phases from the Ge(001) dimer structure were scaled to the alloy composition. These represent the ideal model with no ordering, for the $Si_{0.5}Ge_{0.5}$(001)

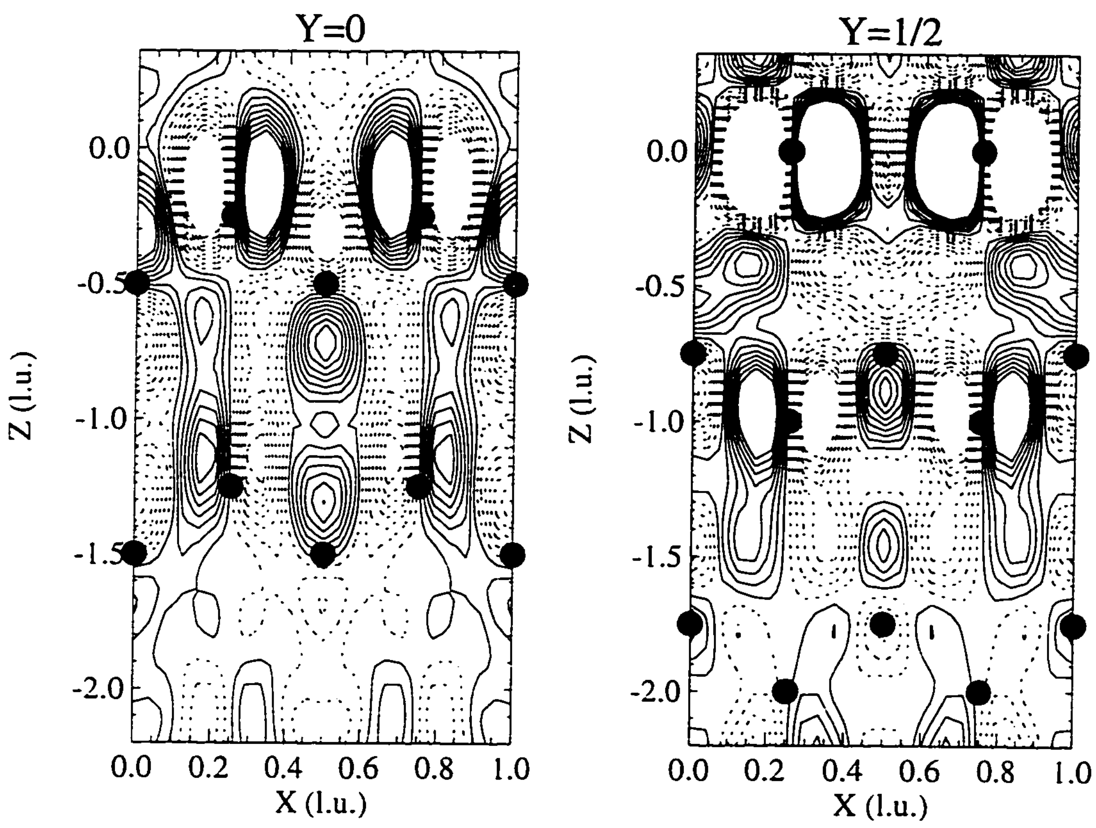

Figure 3.7: Electron density map from surface reconstruction structure factors of Ge(001). Map (a) is the $y = 0$ plane and map (b) is $y = \frac{1}{2}$ plane, which includes the dimer atoms. The solid circles mark the ideal bulk positions. The negative electron density (dashed contours) and positive density (solid contour) represent the displacement of the Ge atoms from their ideal positions.

dimer surface. The structure factors were subtracted from the measured structure factors for the $Si_{0.5}Ge_{0.5}$ film and then Fourier transformed. The result, shown in Figure 3.8, clearly shows the composition ordering to eight layers of the film. The positive densities in layers 3, 4, 7, and 8, correspond to the same locations of higher Ge composition in the refined model. Correspondingly, the negative contours around the opposite lattice site are locations of higher Si composition. Another result is the dipole density pattern at the dimer atoms. This may represent an additional displacement of the dimer atoms, meaning the dimer length bond has shortened from that for the Ge(001). This conclusion is opposite to refinement model above, but agrees with the points discussed above about the average SiGe lattice being smaller than Ge. Although, the Ge segregation observed in the refinement model is not in the difference map. As with the Ge(001) density maps, the reciprocal space cut-off to the data introduces meaningless minor peaks (oscillations) in areas between true atom positions, which can be ignored.

3.3.4 Thicker alloy films and their degree of order

In addition to the thinnest films analyzed above, a series of thicker $Si_{0.5}Ge_{0.5}(001)$ film were grown on Ge(001) substrates. As expected, the amplitude of the compositional order peaks increase with film thickness. Figure 3.9 shows one set of the same surface reconstruction rod, the $(\frac{1}{2}1L)$, for four films, in order of increasing thickness. For the thickest film of 1000 Å, the ordering results in Bragg-like peaks at the $(\frac{1}{2},\frac{1}{2},\frac{1}{2})$ type position. The peaks at half order positions also have the relative amplitudes which confirm the RS2 structure found by Tischler *et al.* [22]. For the data shown Fig. 3.9, the $L = 0.5$ peak is the expected smaller peak, while the $L = 1.5$ is the strongest type reflection according to the structure factors for the RS2 model, discussed in Chap. 1.

Besides the relative magnitudes, our measurements were compared to the pure Ge(001) structure factors, also shown in Fig. 3.9. The Ge(001) structure factors provide an absolute

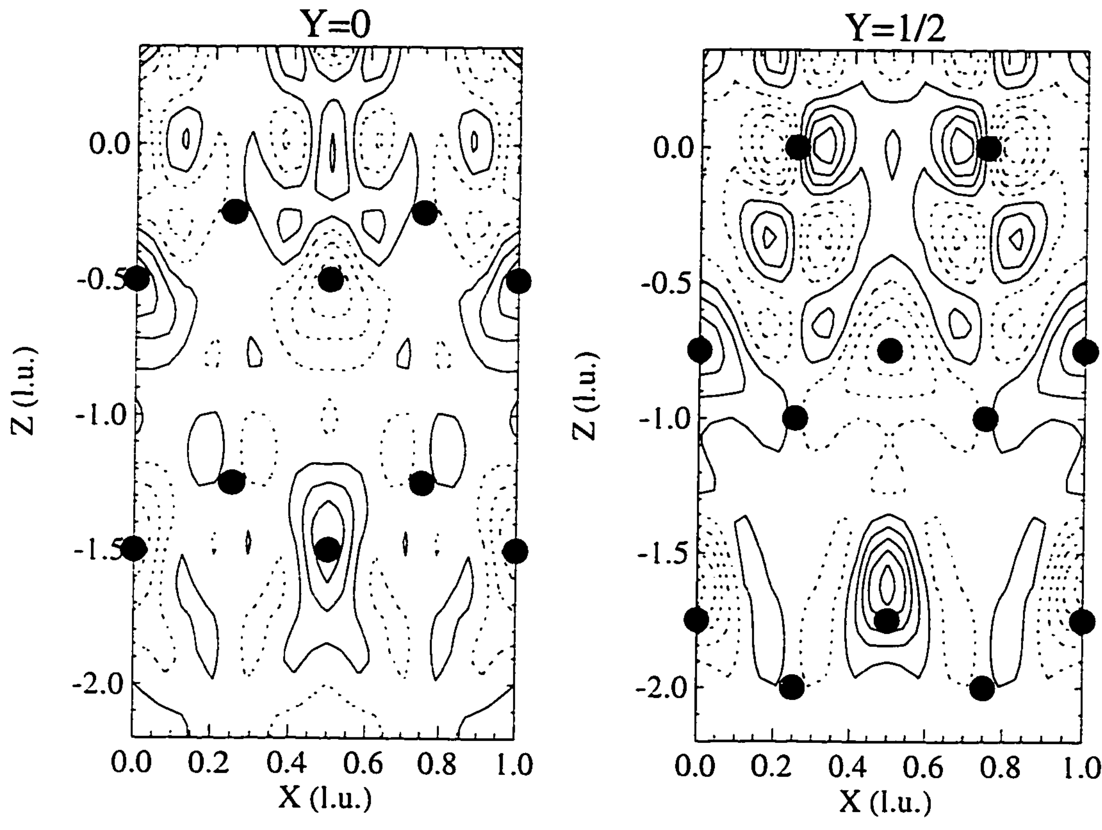

Figure 3.8: Electron difference density map between $Si_{0.5}Ge_{0.5}$ and Ge(001) scaled to the same alloy density. The map of the $y = 0$ plane and map of $y = \frac{1}{2}$ plane show their atoms respective ideal (un-reconstructed) positions as the solid circles. The contour lines are on the same scale as Fig. 3.7

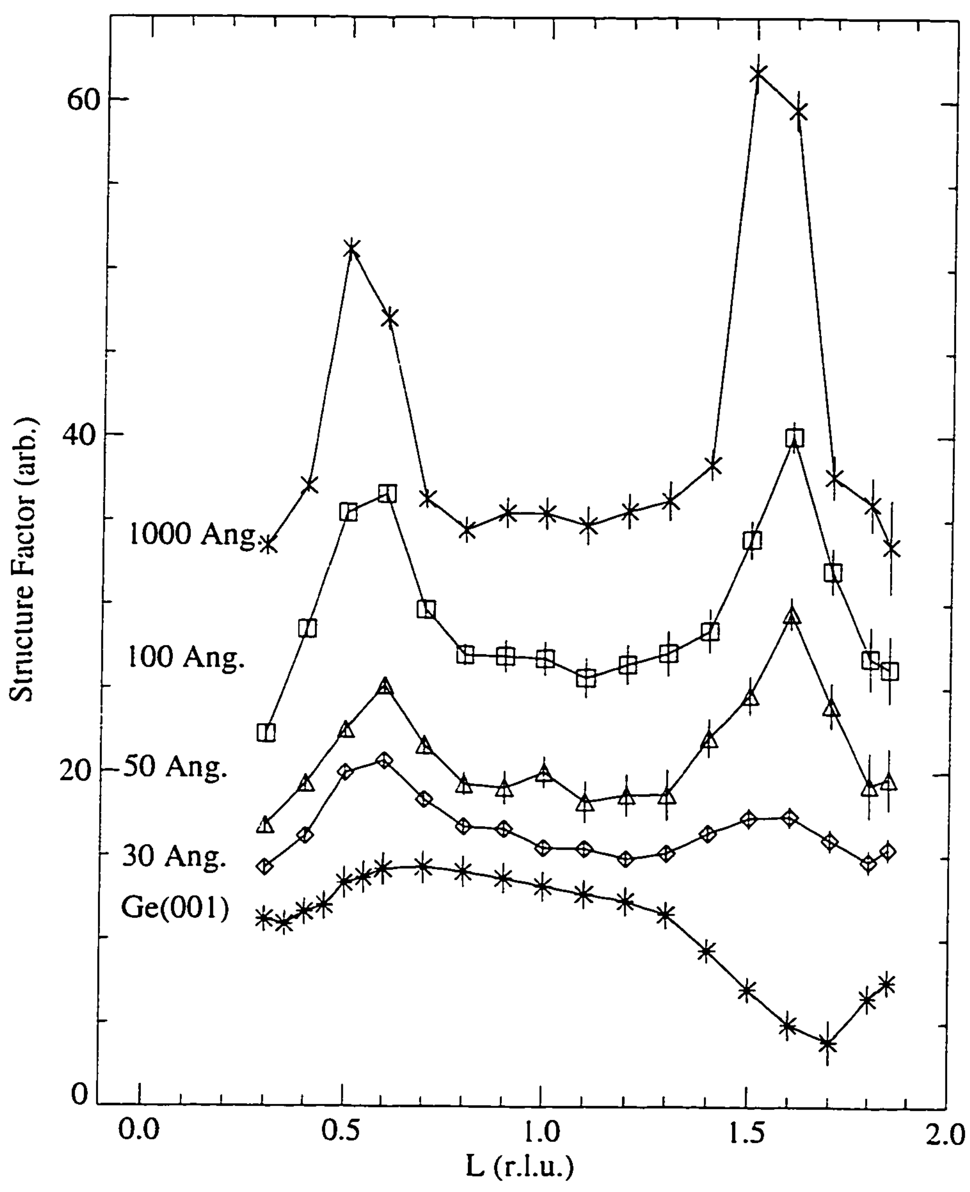

Figure 3.9: Each curve is the same $(\frac{1}{2}, 1, L)$ rod from $Si_{0.5}Ge_{0.5}$ films of various thicknesses. Each curve displaced from the next by +5 with exception of the top most at +15. The alloy film thickness increases from 30 Å, 50 Å, 100 Å and to 1000 Å. The bottom curve is the same for the Ge(001) (2×1) surface.

scale with which to measure the alloy's structure factors. The absolute structure factors can then be used to solve for the average film order parameter. The calculation requires estimating the surface scattering component of the rods, shown in Fig. 3.9 as the intensity between the ordering peaks. This surface component is then subtracted from the specific values at the respective positions $L = 0.5$ and 1.5. This effect is important for the thinnest film of 30 Å where the two sources of the scattering (the surface (2×1) reconstruction and the sub-surface film ordering) are near the same magnitude. This is especially evident for this rod at $L = 1.5$ where the minimum in the surface diffraction signal becomes filled in by the $Si_{0.5}Ge_{0.5}$ ordering peak. This subtracting of structure factor components is an approximation and does not include the possible interference between the surface and film scattering components.

Once the absolute structure factor for the film's compositional ordering was determined, the film's thickness and the intrinsic RS2 scattering factors were used to normalize the values to give the films average order parameter. We used the square root of the thickness for the structure factors because the integrated intensity is proportional to the thickness [1] . This derived average compositional ordering parameter (Table 3.3) is the average throughout the thickness of the film, not the specific ordering within possible individual domains. Table 3.3 lists the measured average order parameter for each film, its thickness and growth temperature. For the thinnest film, the average order parameter from the full model result above is also listed. This was calculated from the model layers 3,4,7, and 8 and assuming the other unresolved layers (5 and 6) have the same average ordering as those measured. The close agreement between the full model and the calculation method for thicker films validates the calculation method for the order parameter from the absolute structure factors.

An interesting result from this table is the increased ordering within the middle thick-

[1] See Warren [1] for a discussion of the bulk integrated intensity and structural order parameter determination

Table 3.3: Average film order parameters of $Si_{0.5}Ge_{0.5}(001)$ for various film thickness and roughly constant growth temperatures. Also, listed are the determined ordering compositions of the (111) bi-layers. The 8 ML thin film modeled above is the last entry (*) where the order parameter is the average from the resolved layers 3,4,7, and 8. The other entry for the 8 ML film is the result using the same method as for the other films.

Thickness	Growth Temp.	Order parameter, p	Ge%-Si%
1000 Å	450°C	0.35±0.09	68%
100 Å	475°C	0.68±0.03	84%
50 Å	400°C	0.71±0.07	86%
30 Å	450°C	0.65±0.05	83%
(8 ML) 10 Å	400°C	0.21±0.05	61%
(8 ML) 10* Å	400°C	0.25±0.02	63%

nesses of the $Si_{0.5}Ge_{0.5}$ thin films. The very thinnest film shows the smallest average order parameter. The thickest film at 1000 Å has the next smallest average order parameter. But in Fig. 3.9, this is the film with largest absolute structure because of the film's bulk thickness. It is possible the ordering is underestimated because of x-ray absorption in this thick of a film. The other films have peaks which are lower in magnitude, and so the subtraction of the surface rod component is a larger factor in the results in Table 3.3. This method of subtracting the surface rod component based on the Ge(001) structure factors, may under estimate the full surface component. This can account for large difference in order parameters between the fully modeled 8 ML film and the 30 Å film. It is satisfying that the largest order parameter is not above the physical limit of 1.0. Ordering parameters as high as 0.64 have been reported by other groups [36, 25].

The results in Table 3.3 does give increased ordering where the film's morphology is changing: from fully strained, pseudomorphic growth at the least thickness, to the relaxed equilibrium $Si_{0.5}Ge_{0.5}$ lattice with misfit dislocations at the thickest film's interface. This result agrees with the proposed model by Jesson *et al.* for the ordering mechanism [21]. Their model suggested that both the increased step density and formation of 3D islands

Table 3.4: Average film order parameters of $Si_{0.5}Ge_{0.5}(001)$ for various film growth temperatures. The last film (*) was annealed *in situ* to 700°C for 5 min.

Thickness	Growth Temp.	Order parameter, p	Ge%-Si%
30 Å	550°C	0.53±0.05	77%
30 Å	450°C	0.65±0.05	83%
20 Å	390°C	0.40±0.06	70%
50* Å	400°C, anneal 700°	0.48±0.05	74%

from strain relaxation and kinetic growth limitations are needed to form the long range order domains. Although, this is not consistent with the thinnest films which are not that rough, or have begun strain relief. This point has been presented before in Ref. [36], which reports continued compositional ordering in films grown by grading the composition to 60% Ge on Si(001) substrate. The grading provided a flat, strain-relieved growth surface, not the morphology supposedly required by Jesson *et al.*

The results from film grown at various temperature and other films that were *in situ* annealed after growth are given in Table 3.4. The maximum in compositional order occurs at about 400–450°C. These results in Table 3.4 are qualitatively the same as present by Ref. [37] and [12]. These $Si_{0.5}Ge_{0.5}(001)$ studies explored a wider range of temperatures, and the films thickness were 7500 Å and 75 Å, respectively.

Kelires and Tersoff's equilibrium model predicts an increased ordering with lower temperatures [28], opposite to the results presented here and in the previous experiments. The presumed causes are kinetic roughening and film disorder as the lowest temperature is near the limits of epitaxial growth of this material. One proposed mechanism by Jesson *et al.*, discussed in Sec. 1.2.4, describes a kinetic process that will limit the lower temperature of ordering. That is, when the step-flow mode of growth is decreased, the step-edge kink propagation (the focus of their proposed mechanism) is also decreased. The decrease at higher growth temperature does agrees with the model of Kelires and Tersoff, where the believed

cause is entropy.

The last film which was annealed to 700°C for 5 minutes shows the compositional ordering decays to almost half the value for the unannealed film (50 Å listed in Table 3.3). Others studies report the annealing removed the compositional ordering completely. But the annealing temperature and time required for the films to disorder, ranged from 700°C for 1 hour [26] and up to 800°C for 2 hours [25]. Our annealing experiment did not reach this highest temperature or length of annealing times.

3.4 Conclusion

Our experiments using surface x-ray diffraction have revealed details of the compositional ordering as it occurs in the growth of thin films of $Si_{1-x}Ge_x(001)$. For the thinnest film of 8 ML (10 Å), our x-ray diffraction measurements show the initial stages of forming the compositional order. The atomic order parameter and the Fourier difference map analyses both show the migration of Ge atoms to the tensile strained sites and Si atoms to the compressive strained sites beneath the surface (2×1) dimer reconstruction. Farther below the surface the compositional ordering is present in the lattice sites consistent with the initial formation of the RS2 $Si_{0.5}Ge_{0.5}$ structure and its bi-layer (111) planes. Although our experiment could not resolve any possible ordering in the symmetric sites below the dimer surface (layers 5 and 6), the results were consistent with the crystallographic experiment by Tischler *et al.* and their results for the RS2 structure [22]. The ordering along the (111) planes may continue through the layer 5 and 6, but the equal distribution of ordering domain across the film obscured this within the resolution of our experiment.

The Fourier difference map of our $Si_{0.5}Ge_{0.5}$ structure factors also provides the evidence for compositional ordering as compared with the Ge(001) dimer reconstructed surface. Unlike model refinement, this method is a direct calculation, independent of any basis, except from

the phases calculated from the model of Ge(001) [30]. Besides the compositional ordering in the layer beneath the dimer, the difference map shows an additional displacement of the dimer atoms to a shorter bond length. This is an opposite conclusion to the refinement model, which found an increased dimer bond length, but with the segregation of higher Ge composition to the surface atoms. This disagreement may be to related to uncertainty in roughness parameters used in both procedures. The surface roughness, which decreases the coherence of the surface diffraction, is implicit within the over-all scale factor for the refinement model, and within the scale factor used to scale the Ge(001) data to same average compositional density as the $Si_{0.5}Ge_{0.5}$. Each of these parameters are refined independently.

The measurement from thicker films of $Si_{0.5}Ge_{0.5}(001)$ provided information on how the strength of the order parameter changes in film thickness and growth temperature. A growth temperature of 400-450°C gave the maximum ordering for film of thickness about 30 Å. A maximum in the ordering occurs at the thickness about 50-100 Å which is 2.5-3 times the magnitude of order found in the initial stages of growth discussed above, or the thickest film measured at 1000 Å. This result affirms the important relationship between the surface structure and the meta-stable ordered structure produced within the film.

This result has some agreement to the calculation by Smith and Zangwill on the relationship between ordering and roughening during growth of an model binary alloy [75]. Their model of thermodynamically favored ordering at the surface only, shows a similar decrease in subsequent film's ordering with increasing film thickness. The change reported is non-trivially related to the model's growing surface morphology. This model quantitatively does not agree we our results, in the rate of decreasing order versus film thickness, but the model system they used was for a simple cubic lattice with epitaxial growth on a lattice-matched fully ordered substrate.

The surface x-ray diffraction experiment has identified features which agree with both proposed mechanisms discussed in Sec. 1.2.4 for the origin of compositional ordering within

$Si_{0.5}Ge_{0.5}(001)$ films. The clearest result is the chemical ordering observed in the sub-surface layers under the dimer reconstruction from the experiment on the thinnest film. This confirms the predictions by Kelires and Tersoff [28] which is the basis for the model mechanism by LeGoues *et al.* [26]. The maximum ordering within the film thickness range of 50-100 Å also supports the model proposed by Jesson *et al.* The increased step density and 3D islanding associated with strain-relaxation at about this thickness would facilitate the proposed asymmetrical segregation across the (2×1) dimer reconstructed surface at the kinks of propagating steps.

To conclude, the ordering mechanism observed in $Si_xGe_{1-x}(001)$ films is clearly not related to bulk thermodynamics, but to the surface kinetics during growth. Two mechanisms have been proposed for the residual compositional ordering within the films and both are strongly related to known (2×1) dimer reconstruction.

Chapter 4

Disordered Structure of Cubic Iron Silicide Films on Si(111)

4.1 Introduction

Iron silicide has recently received increased attention (as with other silicides) as possible materials for advancing today's silicon-based semiconductor industry. The specific interest in iron silicide arises because of the presence of a band gap in the bulk phase β-$FeSi_2$ [53]. This has the promise of being a suitable material for the development of a silicon based electro-optical device. The β phase however is unlike the cubic $NiSi_2$ or $CoSi_2$ which are metallic and have been successfully grown epitaxially on Si; β-$FeSi_2$ has a more complex orthorhombic structure that is believed to be due to a lattice instability explaining the band gap in its electronic structure [54]. In the effort to grow epitaxial iron silicide on Si, new pseudomorphic phases have been discovered, which are not seen in the bulk. Technically, these are not true thermodynamic phases, but are stabilized by the substrate and growth conditions. One such pseudomorphic phase is an iron disilicide, with the fluorite structure, called γ-$FeSi_2$ [55] analogous to $NiSi_2$ and $CoSi_2$ that also have this structure. Another pseu-

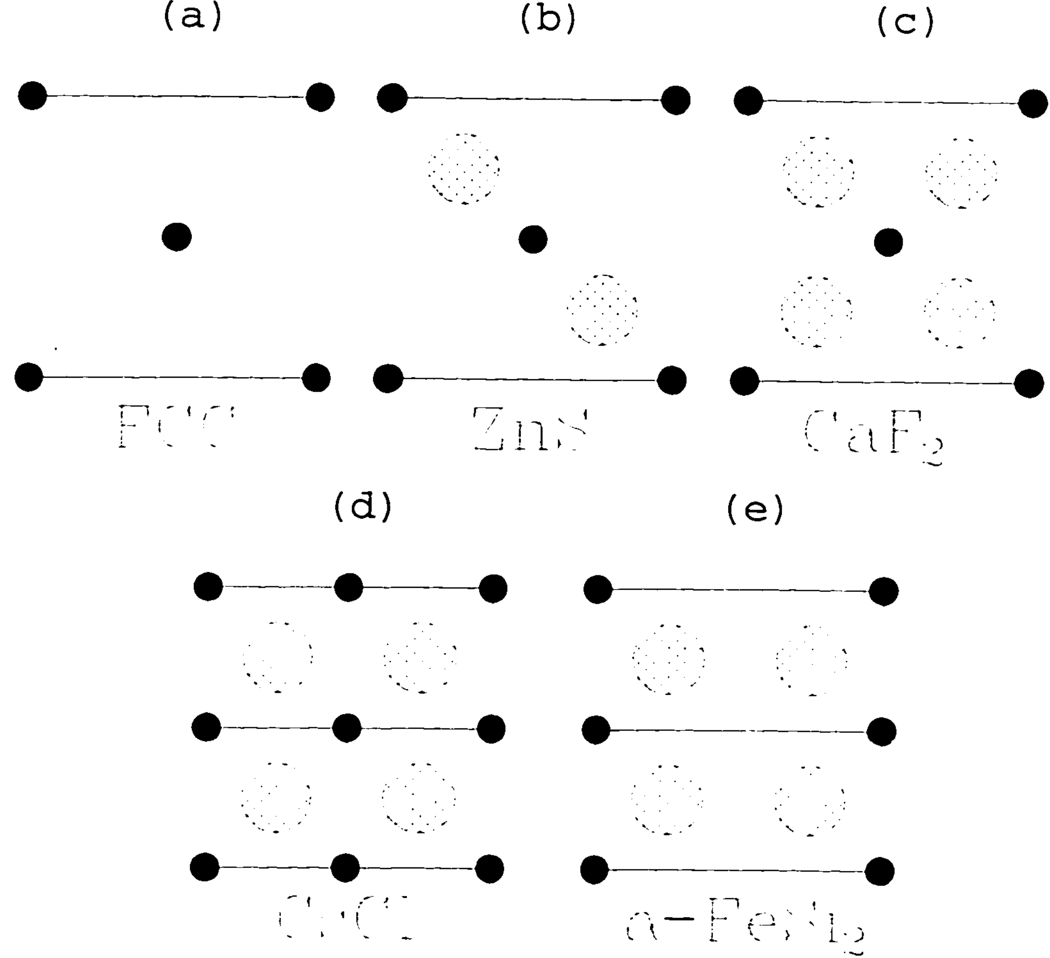

Figure 4.1: Comparison of related cubic structures. Each shows the direct cube face made of type A (metal) atoms as the solid spheres, and a second layer of type B atoms as larger spheres. The structures are: (a) face-centered cubic, (b) zinc blende, (c) fluorite, (d) cesium chloride, and (e) α-$FeSi_2$.

domorphic phase is a CsCl type structured silicide which is characteristic of lower growth temperature [56, 57]. Recently, we proposed that this phase is best described as $Fe_x\odot_{1-x}Si$ with a CsCl type crystal structure where $\odot$ represents iron vacancies [58, 59]. The experiments we report have elaborated on the properties of this new phase. A series of silicide samples with varying thickness and composition was studied with X-ray diffraction and a discussion of their structure will be presented.

The most common bulk phase of cobalt and nickel silicide is the disilicide, $CoSi_2$ or $NiSi_2$, which has the fluorite (CaF_2) crystal structure illustrated in Fig 4.1. The bulk iron silicide

phase diagram is more complex with a variety of phases; including the orthorhombic β-phase mentioned above, the cubic ϵ-FeSi that has a distorted NaCl crystal structure, and the high temperature tetragonal α-$FeSi_2$. The cubic $FeSi_2$ fluorite structure (known as the γ-phase) and the new CsCl phase do not exist in the bulk [60], but only in epitaxial films. The strain induced by epitaxial growth in thin films is a well-known means of favoring a new structural phase over bulk phases, especially when the favored structure is closely lattice-matched to the substrate (an example is bcc Co on GaAs [61]). This is the case for γ-$FeSi_2$, which has a lattice parameter closely matched with Si and is one of the phases observed only in thin films [56]. The case is similar for α-$FeSi_2$ which forms epitaxially far below its bulk formation temperature [62, 63], which we also observe.

When $FeSi_y$ is grown by MBE at room temperature, it does not have the fluorite structure but has the CsCl structure instead. These crystal structures are in fact closely related, as Fig. 4.1 attempts to demonstrate. The figure shows a series of cubic structures viewed directly on the cube face. It starts with the primitive face-centered cubic (fcc) lattice made up entirely of atoms of type A in Fig 4.1(a). By adding a second kind of atom (type B) at four of the $(\frac{1}{4}, \frac{1}{4}, \frac{1}{4})$ positions, this becomes the zinc blende (ZnS) structure shown in Fig 4.1(b). By filling the remaining four $(\frac{1}{4}, \frac{1}{4}, \frac{1}{4})$ positions with B atoms, it becomes the fluorite (CaF_2) structure shown in Fig. 4.1(c). Finally, upon filling the previously empty 8-fold coordinated sites between the B atoms with A atoms, this transforms into the CsCl structure (Fig 4.1(d)) with a unit cell of half the size. From the point of view of diffraction, structures (a) (b) and (c) all have fcc selection rules, but structure (d) is simple cubic, so can be distinguished by the presence or absence of fcc reflections. Structures (a) (b) and (c) can only be distinguished by the relative intensities of their reflections, i.e. by crystallographic analysis. Shown in Fig. 4.1(e), and discussed in Ref. [64], is the α-$FeSi_2$ structure that is also related by removing alternating (100) planes of Fe (type A atoms) within the CsCl structure.

One reason for drawing the structures beside each other in Fig. 4.1 is to illustrate the

role of disorder. If the B (fluorine) sites in the CaF_2 structure are only partially occupied. its diffraction intensities will tend towards the ZnS structure; in the special case of 50% occupation (randomly distributed), we would have the situation of identical stoichiometry and the only distinction between the structures would be small differences in the relative diffraction intensities. The situation for structures (c) and (d) is analogous. Random 50% occupation of the A sites of the CsCl structure in (d) yields a disordered version of the CaF_2 structure in (c), which, since it has identical stoichiometry, can only be distinguished crystallographically. We report here that this random occupation description represents the case of $FeSi_y$ (or more appropriately Fe_xSi) films grown at room temperature on Si(111).

4.2 Method

The various iron silicide samples were grown by room temperature molecular beam epitaxy (MBE) . All samples started on cleaned Si(111) surfaces showing a 7×7 reconstruction. Samples were grown with a range of thicknesses and with two ratios of stoichiometry. Three silicide films were grown by co-deposition of Fe and Si in the ratio of 1:1 after initial deposition of two monolayers (ML) of pure Fe. Another set of four samples was grown in a two step process: the 1:1 co-deposition of a template was stopped after 5 Å of growth and the film annealed to 400-500°C, then additional Fe and Si in a ratio of 1:1 were deposited at room temperature to the desired final thickness. We know from previous XPS and UPS studies that this annealing step results in a template of cubic Fe_xSi [56]. Other studies of the monolayer Fe structure on Si(111) have found the formation of this template CsCl structure and its B-type interface [65, 66]. Using this template, five more samples were grown with a Fe to Si ratio of 1:2. Three of these five were overgrown with Si and later annealed to 630°C. A quartz crystal monitor was used in each case to determine the film thickness. All unannealed samples were sealed with an amorphous Si cap layer about 20 to 100 Å thick to protect them

during transport through air. For the three annealed 1:2 growth samples. the diffraction scans confirmed the Si cap layers to be epitaxial. A more detailed description of the sample growth can be found in Ref. [67]13.

The X-ray diffraction experiments were carried out on beam line X16B at the National Synchrotron Light Source at Brookhaven National Laboratory. The fixed geometry of the beamline provides a focused monochromatic X-ray beam with a wavelength of 1.69 Å. The samples were mounted on a Huber 4-circle diffractometer and the diffraction intensities measured with a scintillation detector. Both the incident and reflected X-ray beams were defined by 1×1 mm slits. The Bragg peaks (111), (113), and (220) of the silicon substrate were used to align the substrate to the diffractometer.

Diffraction from the films was measured by means of 'direct rod scans' selecting the measurement points along straight lines in reciprocal space perpendicular to the sample surface. At selected points, integrated intensities were measured by means of rocking curves (ω-scans), performing a background subtraction and applying corrections for sample area and Lorentz factor. In this chapter the results from the diffraction experiments are organized into four sections: the epitaxial crystal symmetry, the structure factors (or integrated intensities), the film strain, and finally the thickness and uniformity of the silicide films.

4.3 Crystal Symmetry of the Films

We used searches for the points of maximum intensity to determine the locations of film Bragg peaks. This differentiated two groups of samples: the unannealed films with differing stoichiometries, and the 1:2 stoichiometry silicide films annealed to 630°C.

For the unannealed films, the locations of the film Bragg peaks determined the lattice symmetry to be rhombohedrally strained cubic, with the strain axis perpendicular to the interface. The reflections will be indexed in this chapter as simple cubic. However, not all

the Bragg reflections at face-centered cubic (fcc) positions were seen, which immediately rules out the CaF_2 structure found in other silicides such as $NiSi_2$ and $CoSi_2$. So, although the sets of unannealed films were grown with differing stoichiometries, each silicide film has a simple cubic symmetry with a lattice parameter about half that of substrate, implying the CsCl structure for the reasons stated above. Scans in momentum transfer parallel to the (111) interface ($q_{||}$) through the film Bragg peaks determined the quality of the single crystal epitaxy to the substrate crystal Si(111). The film Bragg reflections were found to be commensurate with the substrate reflections, meaning each film's lattice constant parallel to the epitaxial interface is matched to the corresponding substrate lattice constant. Because of the (111) orientation, the Si substrate projection onto the interface is a 2-D hexagonal lattice, which is matched to that of the films. The orientation of the unannealed silicide films to the substrate is $[111]_{film} \parallel [111]_{Si}$ and $[2\bar{1}\bar{1}]_{film} \parallel [11\bar{2}]_{Si}$. The film lattice is not a simple continuation of the substrate, but rotated by 180° along an axis parallel to (111); such a rotation is allowed by the hexagonal symmetry of the interface and is usually called "B-type".

These crystal symmetry results were essentially the same for all the unannealed samples (i.e. all stoichiometries), except to the extent that the strains were different (see below). Because of the B-type orientation, the missing peaks were located in relatively empty regions of reciprocal space, so an upper limit of 0.05 can be placed on the fraction of any ordered fluorite phase that might have occurred.

In contrast for the annealed films, Bragg peaks besides the simple cubic reflection were observed at half-order positions along the three (100) directions. As described in Ref. [62], the tetragonal unit cell of α-$FeSi_2$ with three rotational domains provided a (112) plane and pseudo-hexagonal interface symmetry that is consistent with the observed Bragg reflections. The pseudo-hexagonal symmetry results from the c/a ratio being 1.9, instead of 2.0 (see Fig. 4.1(e)), and thus the additional half-order peaks. $q_{||}$ scans through the Bragg peaks

determined the film domains to be commensurate with the substrate giving an epitaxy orientation of $(112)_\alpha \parallel (111)_{Si}$. The films were also strained along this axis perpendicular to the interface.

4.4 Structure Factors

An immediate problem is presented to us in the fact that a range of unannealed samples, with stoichiometries varying by a factor of two, shows the same CsCl crystal symmetry. As explained in the introduction, this can be due to systematic disorder in the lattice and that quantitative (crystallographic) analysis is needed to measure the behavior.

One sample from each of the 1:1 and 1:2 stoichiometric sets was chosen for crystallographic analysis. To obtain the integrated intensity of a reflection, the sample angle, ω, was scanned with the detector's aperture set wide open (10×10 mm). For each sample, all Bragg reflections up to the diffractometer limit of 5.6 $Å^{-1}$ were measured. Taking the square root of the integrated intensities gives the structure factor for the scattering of a unit cell, to within an overall scale factor for each sample. Symmetry equivalent reflections were combined into an average structure factor for each data set. Fig. 4.2 and Fig. 4.3 display the measured structure factor versus total momentum transfer. Each reflection is labeled in the cubic representation of the silicide. Note that these are pseudo-cubic labels, because the strain actual removes some of the symmetry, as can be seen by the different momentum transfer of the two reflections marked (111) and $(\bar{1}11)$. The (111) reflection is normal to the surface of the silicide film while there are three inequivalent reflections $(\bar{1}11)$, $(1\bar{1}1)$, and $(11\bar{1})$ which are more parallel to the surface.

In each case, the general trend of the structure factors divides them into two groups of reflections according to the selection rules of the cubic CsCl atomic structure of Fig 4.1(d). This structure is similar to a body centered cubic (bcc) lattice except the corner sites and

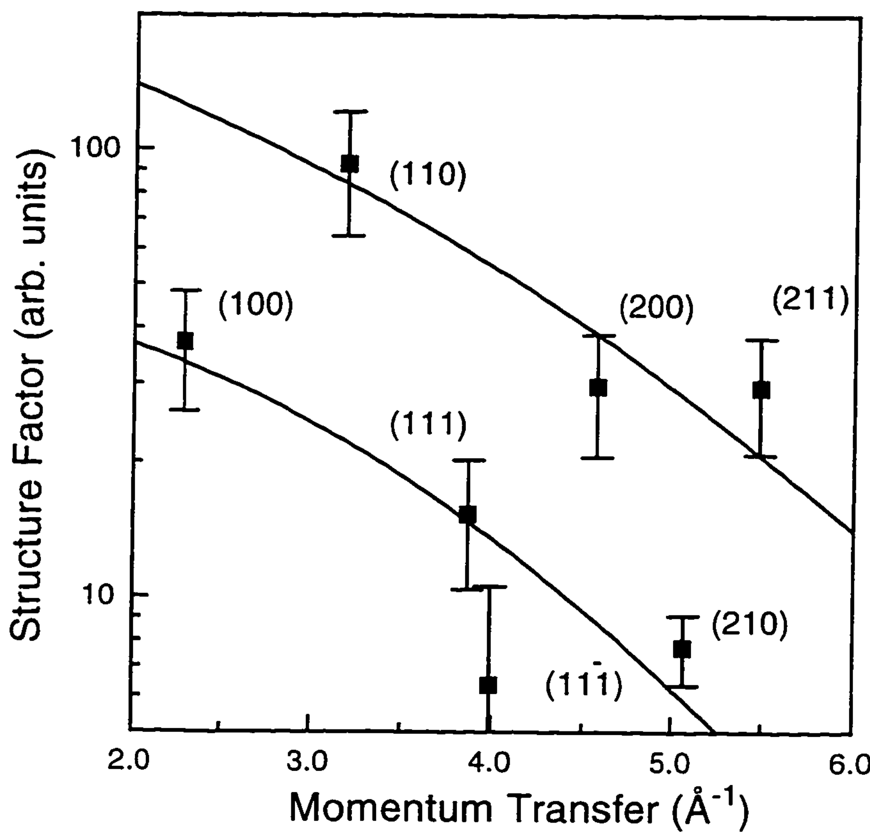

Figure 4.2: Structure Factors vs. total momentum transfer for 1:1 stoichiometric sample, no. 7001. Measured reflections are labeled in the silicide's (strained) cubic coordinates. The top and bottom curve are fits for the CsCl model formulae F_+ and F_-, respectively, with Fe occupation $x = 0.88$, and Debye-Waller factor 0.33 Å.

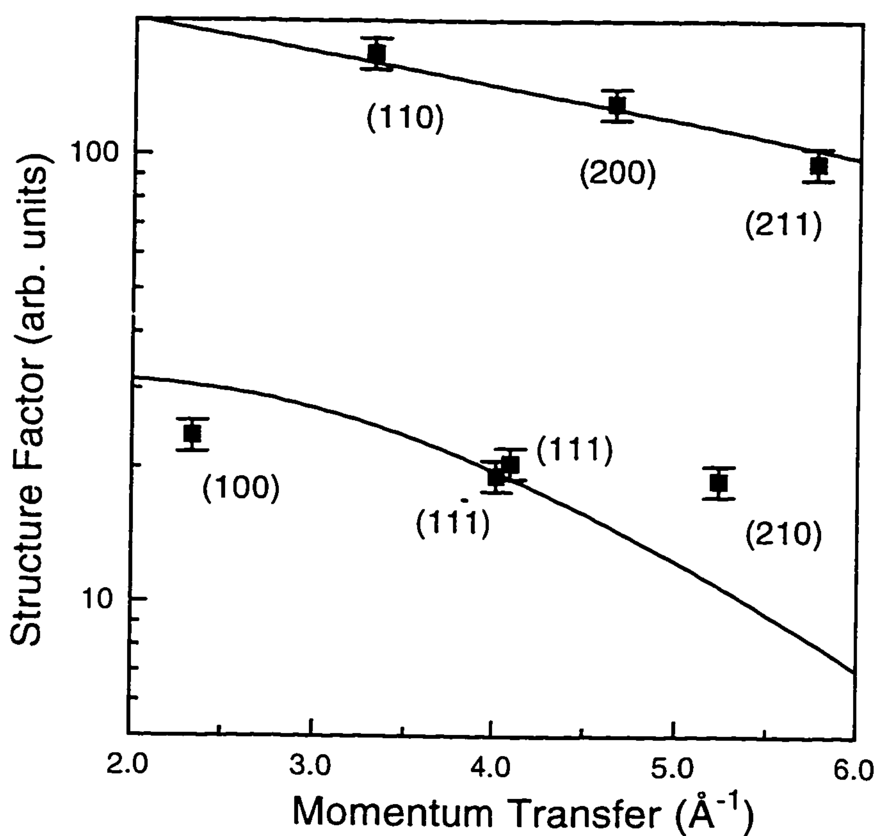

Figure 4.3: Structure Factors vs. total momentum transfer for 1:2 stoichiometric sample, no. 1023. Measured reflections are labeled in the silicide's (strained) cubic coordinates. The top and bottom curve are fits for the CsCl model formulae F_+ and F_-, respectively, with Fe occupation $x = 0.69$, and Debye-Waller factor 0.10 Å.

center sites are occupied by different atoms. Therefore, the larger structure factors correspond to bcc-allowed reflections with all the atoms scattering in-phase. The smaller reflections are due to out-of-phase scattering of the different atoms. In a bcc lattice these latter reflections are absent, but in the CsCl structure the different atomic scattering factors of the Cs and Cl (or Fe and Si) results in a non-zero structure factor. These relative magnitudes of the in-phase and out-of-phase reflections for the two samples are not the same.

To understand why two samples grown with different stoichiometries have the same symmetry, a simple model is constructed for comparison with the observed structure factors. This model is FeSi in the CsCl structure with a stoichiometry dependence modeled by corresponding occupation of the Fe sub-lattice, i.e. Fe_xSi. Only two different formulae for the structure factors are needed as a function of the momentum transfer. The model structure factor for the bcc type or in-phase reflections is

$$F_+ = A\,(x f_{\mathrm{Fe}} + f_{\mathrm{Si}})\, e^{-q^2\langle u^2\rangle/2} \tag{4.1}$$

and for the bcc absent or out-of-phase reflections it is

$$F_- = A\,(x f_{\mathrm{Fe}} - f_{\mathrm{Si}})\, e^{-q^2\langle u^2\rangle/2}. \tag{4.2}$$

To fit the model to the measured structure factors, three parameters are varied: x, the occupation fraction for Fe atoms; $\langle u^2\rangle$, the Debye-Waller rms vibration amplitude for both atoms; and A, an overall scale factor that was not removed from the data. The atomic scattering factors for Si and Fe are accurately known, including a dispersion correction for Fe. The dispersion correction is needed because the fixed X-ray energy of 7.1 keV at beamline X-16B is close (0.4 keV) to the iron K-shell absorption edge.

The curves in the Fig. 4.2 and 4.3 are the least squares fit for the model above. On a logarithmic plot, the scale and Debye-Waller factors are represented as an overall displacement and a parabola, respectively, to the fitted curves. The Debye-Waller parameters for the 1:1 and 1:2 ratio films are 0.33 ± 0.10 Å and 0.10 ± 0.05 Å, respectively, which compares

with 0.075 Å for bulk Si [3] and 0.10 Å for bulk Fe [1]. The larger Debye-Waller factor for the 1:1 grown film is believed to related its large strain and possibly larger lattice disorder. A noticeable difference between the two samples is the ratio (or difference on the log plot) between the in-phase and the out-of-phase structure factors. The spacing between the two curves is accounted for by the occupation parameter, x, for iron. For the 1:1 stoichiometry (Fig. 4.2), the best fit value is $x = 0.88 \pm 0.13$, near the ideal FeSi(CsCl) structure. For the 1:2 stoichiometry (Fig. 4.3), the best fit value is $x = 0.69 \pm 0.08$. This is corresponds to a defect CsCl or $Fe_x\odot_{1-x}Si$ structure with $\odot$ representing statistically random iron vacancies. From the stoichiometry of growth conditions, one would expect the value of $x = 1.0$ and $x = 0.5$, respectively. The structure factor data clearly shows a substantial vacancy presence in the CsCl structure. A possible explanation of the discrepancy to the expected values is a relationship to the film strain which will be discussed below.

We note that the model does not consider the substitution of Fe sites by Si atoms, which could produce similar results, but is considered unlikely because such body-centered Si atoms would need eight nearest-neighbor bonds to the surrounding Si atoms. The strain measurements below also reject this hypothesis for either of the films.

Another model that was consider for the 1:1 stoichiometric film was the substitution of Si sites (the body center sites) by Fe atoms. This structure is suggest by the known bulk alloy of α-Fe and Si concentrations up to 10% [60]. This dilute alloy is known to have the similar structure, where the Si atoms occupy the same bcc 8-fold coordinated site substitutionally. The proposed model is the similar except the Si stoichiometry is up to 50% in an simple cubic sub-lattice, as bcc sites in the Fe matrix lattice. As the Si stoichiometry is decreased, Fe atoms then randomly substitute in for the Si sites. The model structure factors for the same reflection above are

$$F_+ = A\left[f_{\mathrm{Fe}} + ((1 - x^s)f_{\mathrm{Si}} + x^s f_{\mathrm{Fe}})\right] e^{-q^2\langle u^2\rangle/2} \qquad (4.3)$$

[1]calculated from Debye temperature given in Ref. [4]

$$F_{-} = A\left[f_{\mathrm{Fe}} - ((1-x^{s})f_{\mathrm{Si}} + x^{s} f_{\mathrm{Fe}})\right] e^{-q^{2}\langle u^{2}\rangle/2}. \qquad (4.4)$$

where x^s is the faction of Fe atoms substituted in the Si bcc sites. There are no vacancies assumed in any lattice sites. The bulk Fe:Si stoichiometry ratio is $1 + x^s : 1 - x^s$ for this model. The results of fitting this model to the measured structure factors for the 1:1 grown stoichiometric film (no. 7001) are $x^s = 0.19 \pm 0.05$, and $u = 0.33 \pm 0.10$ Å for the Debye-Waller parameter. The Fe:Si stoichiometry from this result is 60%:40% (Fe:Si), which is farther from the nominal growth stoichiometry (50:50%) than the vacancy model's result above of 47%:53%. Although, both models fit the measured structure factors equally well within the uncertainty. The substitution of Fe for Si sites model does have the iron rich stoichiometry, which is in agreement with the Rutherford backscattering spectroscopy result of 58%:42% (Fe:Si) for this film. The iron rich stoichiometry also agrees with the results from conversion electron Mössbauer spectroscopy showing a minority of Fe chemical shifts from 8-fold coordination with Fe nearest neighbors (Si site substitution) [68].

We note this iron substitution model could also produce similar agreement to the measure structure factors from the 1:2 stoichiometry silicide film. But, this is considered implausible since the iron substitution and Fe rich stoichiometry is opposite to the growth condition which are Si rich, and Fe poor. Also, the strain measurement below reject the Fe substitution for the 1:2 films.

4.5 Strain

For strain and film thickness information, scans of the momentum transfer perpendicular to the film, $q_\perp$, were performed. We used index scans following the X-ray scattering intensity between the Si substrate Bragg peaks along the lines perpendicular to the surface. These scans measure contributions from both the (commensurate) film and the substrate crystal: the abrupt termination of the lattice leads to crystal truncation rods (CTR) extending between

Table 4.1: Lists of results, atomic plane spacing, and in-plane coherence lengths . The samples used for the structure factor analysis are listed first. No. 1059 is one sample grown in a two-step 1:1 process. No. 1066 is one of the annealed 1:2 grown samples, with the α-$FeSi_2$ structure. The uncertainty of the last significant digit is in parentheses.

Sample No.	Thickness (Å)	Fe_xSi (CsCl)	$\langle d_{(111)}\rangle$ (Å)	Rhombohedral distortion (%)	In-plane coherence length (Å)
7001	270	$x = 0.88$ (13)	1.630 (3)	3.8 (2)	2300
1023	105	$x = 0.69$ (8)	1.540 (6)	-1.8 (4)	4200
1059	45	x = 1 [a]	1.640 (2)	4.5 (2)	1100
1066	40	n.a. (α-$FeSi_2$)	1.523 (16) [b]	-2.5 (10)	6700

[a]From growth conditions.
[b]d for (112) of tetragonal cell.

the bulk Bragg peaks in this direction [7, 6]. In each sample three or more Bragg reflections from the film were sampled. In the film cubic lattice coordinates, these Bragg peaks are indexed (100), (110), and (111). The Bragg peaks however did not position exactly at these points, but were displaced along the direction perpendicular to the surface. As mentioned above, all unannealed samples were found to have the same general cubic symmetry but differences were present in the form of strain, or distortion from the cube. The annealed α-$FeSi_2$ films are similarly strained if one considers a larger near-cubic unit cell with $a' = 2a$. From the scans in $q_\perp$ the precise position of the Bragg peaks was determined. Their average gave the lattice spacing perpendicular to the interface. Table 4.1 lists the plane spacing d for two samples used for the structure factor analysis and other representative samples. No displacement of the peaks parallel to the interface was detected indicating the lattice spacing parallel to the interface is the same as (half) that of the silicon lattice constant. The rhombohedral distortion can be calculated from this by

$$\varepsilon_R = \frac{a_\perp - a_\parallel}{a} \tag{4.5}$$

where a is an estimated bulk lattice constant. The value of a was estimated from $a_{\perp}$, $a_{\parallel}$, and the elasticity constant of Possion's ratio, σ, taken to be 0.35, a value determined by earlier Brillouin scattering measurements [69]; this is a very small correction however. The resulting values for the rhombohedral distortion are plotted in Fig. 4.4 as a function of film thickness. The drawn lines are only to bring attention to how the samples fall in three classes: compressive strain or positive rhombohedral distortion, and tensile strain or negative rhombohedral distortion for both unannealed and annealed. The tensile strained films are the ones grown at the 1:2 stoichiometric ratio and the compressive strained films were grown at the 1:1 ratio. From the strain calculations, the estimated bulk lattice parameter for the 1:1 films is about 2.78 Å, which in close agreement to a theoretical (T = 0 K) value of 2.72 Å for FeSi (CsCl) in Ref. [70]. For the 1:2 disordered unannealed films the estimated bulk lattice parameter is 2.69 Å.

This difference in strain supports the defect CsCl structure model. As iron vacancies are introduced into the CsCl structure, the average coordination for Si atoms decreases. This generally results in a contraction of the lattice. Such a contraction with the decrease in Fe stoichiometry would result in the compressive to tensile strain difference as shown for the 1:2 grown films. The opposite would be expected if Si were substituting for the Fe atoms. Silicon in iron sites of CsCl structure would produce an expansion from the increased coordination of the Si, in contradiction to the measured results. As mentioned above the strain could explain why the determined Fe stoichiometry (from the structure factor analysis) was different from the expected growth stoichiometry: large stoichiometry extremes would result in larger extremes in strain. Partial adjustment of the stoichiometry (maybe involving the substrate) to relieve strain would cause the final value to be closer to the (nominal) intermediate value of a completely relaxed film. More experiments are needed to answer this hypothesis and questions it raises, such as, how stoichiometry and strain are related in these systems.

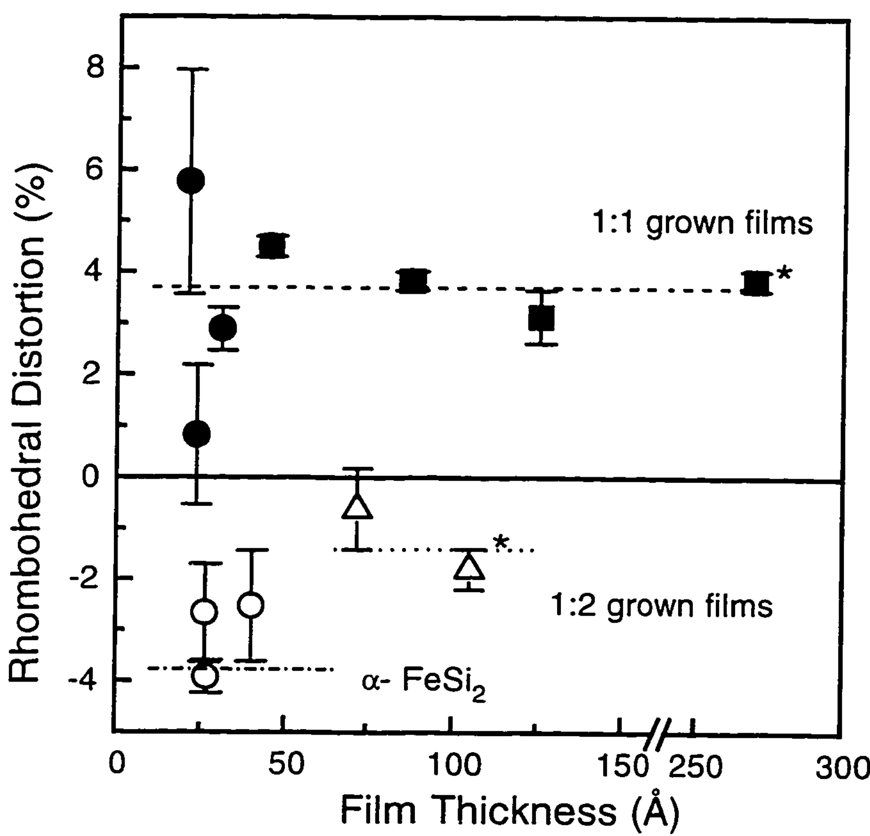

Figure 4.4: Rhombohedral distortion of silicide films vs. film thickness. The solid squares are for films grown with 1:1 Fe to Si stoichiometry. The solid circles are for the two step 1:1 grown films. The open triangles are unannealed 1:2 grown film. The open circles are for annealed films grown with 1:2 stoichiometry (and found to be α-$FeSi_2$). A positive distortion corresponds to compressive strain. The lines are drawn only to aid the eye. The two samples used for the structure factor analysis are marked with asterisks.

With regards to the other model (Fe substitution in Si sites) for the 1:1 grown film. the strain results also agree. Again the Fe substitution forms a familiar bulk α-iron complex. The bulk bcc Fe lattice constant is 2.87 Å[4], larger but close to the estimated lattice constant for the 1:1 FeSi (CsCl) film. This small Fe substitution in the 1:1 FeSi film is expected to increase the average lattice constant of the film, agreeing with the observed compressive strain. But for the 1:2 film, Fe substitution would have the similar effect as the Si substitution argued above, and opposite the observed tensile strain.

The third set of points on Fig. 4.4 show that the effect of annealing is apparently to increase the strain in the 1:2 grown films. This is understood to be due to the c/a ratio of 1.9 instead of 2.0, however. These annealed films have a tetragonal structure so they no longer have a simple rhombohedral strain. Taking the bulk α-$FeSi_2$ lattice parameters [2] , the near-cubic unit cell volume is 7.3% smaller than Si, consistent with the -3.7% linear contraction observed.

4.6 Thickness and Uniformity of the Films

The $q_\perp$ scans also show thin film oscillations (Laue fringes) to the sides of the Bragg peaks. A least squares fit to the oscillations from some of the samples was possible using a theory described in Ref. [72]. The theory considers a discrete distribution of film domains with thickness Nd. The total scattered amplitude is then the sum of the individual domain amplitudes over this distribution:

$$A = \sum_N P_N F(q) \frac{1 - e^{iq_\perp Nd}}{1 - e^{iq_\perp d}} \tag{4.6}$$

. The structure factor $F(q)$ includes the atomic structure of the film and therefore the transverse momentum dependence. Assuming a binomial distribution for P_N, the sum can be performed analytically. The sum is analogous to the moment generating function for

[2] $a = 2.69$ and $c = 5.13$ Å. [71]

this statistical distribution. A binomial distribution can be justified since it approaches a Gaussian distribution in the continuum limit. Squaring the amplitude gives the intensity function as

$$I = |F(q)|^2 \frac{\frac{1}{4}(1-\alpha)^2 + \frac{1}{4}\alpha \sin^2\left[\tilde{N}d\left(q_\perp - \zeta\right)/2\right]}{\sin^2\left(q_\perp d/2\right)} \tag{4.7}$$

where we have used the following definitions:

$$\alpha = \left[1 - 4\epsilon(1-\epsilon)\sin^2\left(q_\perp d/2\right)\right]^{\frac{\tilde{N}}{2}}, \tag{4.8}$$

$$\zeta = \frac{1}{d}\arctan\left(\frac{\epsilon \sin(q_\perp d)}{\epsilon \cos(q_\perp d) + (1-\epsilon)}\right), \tag{4.9}$$

$\tilde{N} = M/1-\epsilon$, and $\epsilon = s^2/M$. These quantities relate to physical quantities describing the films: the mean film thickness is Md and the roughness is sd. Thus from the fringe spacing, an accurate determination of thickness is obtained as well as an estimated roughness or variation of the film thickness. An example of the data is given in Fig. 4.6 where the curve is the best fit for a film thickness of 89 Å and a roughness of 7 Å. The growth conditions indicated a thickness of 70 Å. Some silicide samples had more complicated peak shapes probably due to strain gradients that could not be fit by this simple model.

Table I lists the in-plane coherence length for some of the film samples. Using cross-section scans through the film Bragg peaks along a direction parallel to the interface, the in-plane coherence length was determined from the peak's full width at half maximum (FWHM) by

$$L = \frac{2\pi}{\Delta q(\mathrm{FWHM})} \tag{4.10}$$

For all samples the coherence perpendicular to the interface is limited to the thickness of the films, as demonstrated above.

4.7 Conclusions

We have determined the structure of iron silicide films grown at room temperature on a Si(111) substrate. The films grow pseudomorphically and commensurate in the (111) plane.

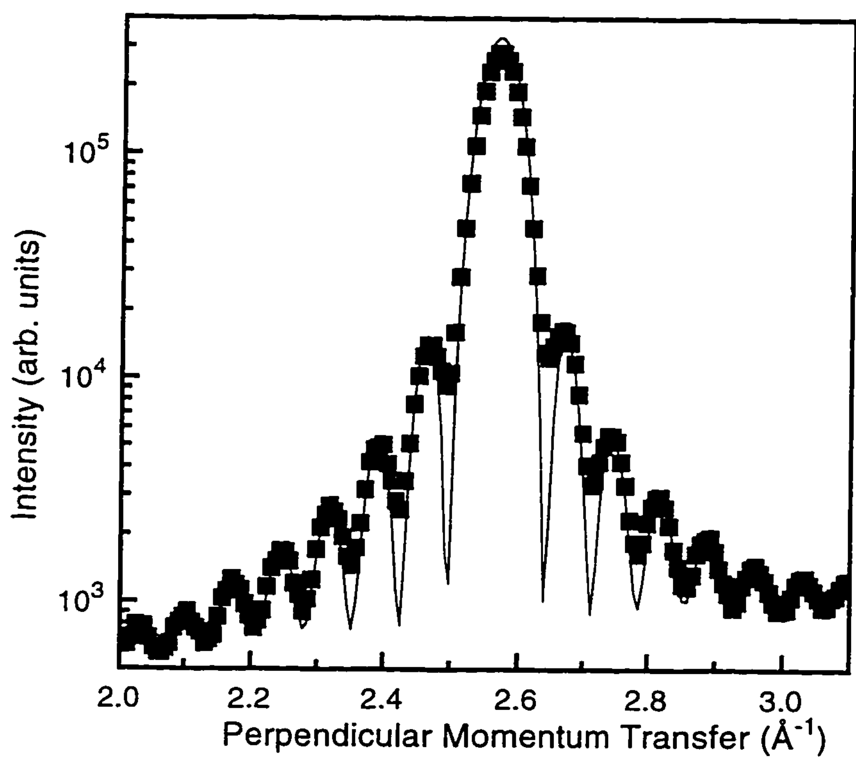

Figure 4.5: Example scan of silicide film Bragg peak (110) vs. momentum transfer perpendicular to the surface, $q_\perp$. The solid curve is a least squares fit for a thin film of thickness 89 Å and a roughness of 7 Å.

The film Bragg peak positions and the absences of other peaks determine the film structure to be that of the cubic CsCl structure (space group $Pm\bar{3}m$) with about half the unit cell of the Si substrate for all the unannealed samples. The total absence of peaks at the positions of a fcc lattice informs us that there is no CaF_2 phase (space group $Fm\bar{3}m$) even for 1:2 stoichiometric samples. The CsCl structure agrees with TEM diffraction and RHEED experiments [55, 56].

Although unannealed samples show exclusively the symmetry of the CsCl structure, there is a pronounced strain effect as the stoichiometry is varied, as seen in the figure of rhombohedral distortion. The rhombohedral distortion changes sign between the different extremes of stoichiometries. This is correlated will a clear change in structure factors. Unlike the previous TEM and RHEED experiments, our structure factor measurements allow us to determine the atomic occupation within the lattice. This constitutes the strongest proof so far of a vacancy model with partially occupied Fe sites in the CsCl structure. Therefore, a better notation for the composition of this silicide would be $Fe_x\odot_{1-x}Si$ with $0.5 \leq x \leq 1$ for the fraction of Fe. The iron vacancies are represented by open circles in the disordered CsCl structure in Fig. 4.5. By randomly removing up to half of the Fe from the CsCl silicide, the average local symmetry is not changed, but change is clearly seen in the comparison between structure factors, and is also consistent with the rhombohedral distortion data. If the Fe vacancies were in fact ordered at $x = 0.50$, the resulting structure would be the CaF_2 structure (Fig. 4.1(c)). Although not present in any of our samples, this has been seen with TEM on thin films of 1:2 ratio iron silicide that are annealed slowly and transformed to islands of γ-$FeSi_2$ (CaF_2 structured) phase [55]. This chapter's conclusions are consistent with the idea suggested by the TEM experiment, that the as-grown 1:2 stoichiometry films are a disordered, but can become ordered upon annealing.

Other recent studies confirming the Fe vacancy model for the 1:2 stoichiometric films have been from x-ray absorption and Mössbauer spectroscopy experiments. Both methods probe the local structure around specific atoms. The conversion electron Mössbauer spectroscopy

(A)

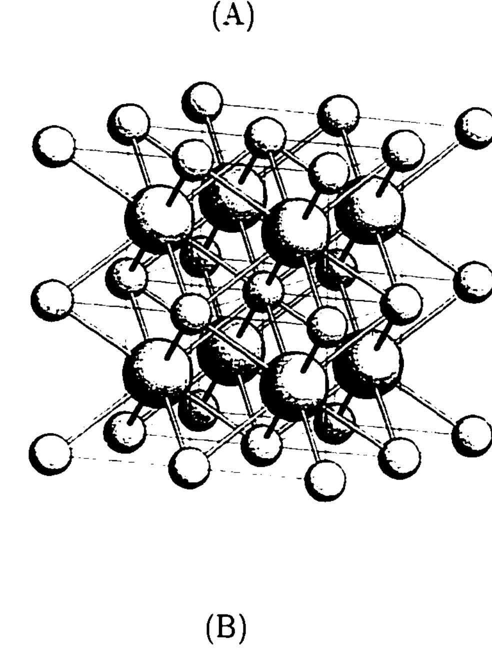

(B)

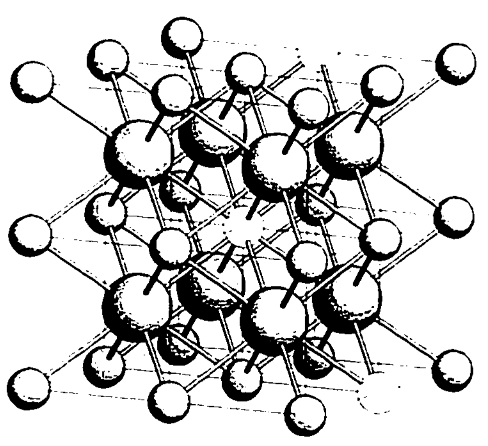

Figure 4.6: Lattice representations for (a) FeSi (CsCl structure), and (b) $Fe_x\odot_{1-x}Si$ (disordered CsCl structure). The smaller and larger spheres represent Fe and Si atoms, respectively. The open circles in (b) represent disordered Fe vacancies.

study by Fanciulli *et al.* reports a series of 6 chemical shifts for the 6 different possible coordination sites of Fe atoms and the surrounding second nearest neighbor shell of Fe atoms and/or vacancies [73]. Similar, a x-ray absorption fine structure (XAFS) study found lowered coordination numbers for the Si and Fe atoms then the expect bonding coordination in an ideal CsCl structure. [74]. Again confirming the model of vacancies in the Fe sites surround the Si atoms, not Si substitution for the 1:2 stoichiometric iron silicide films.

References

[1] B. E. Warren, *X-ray Diffraction*, (Addison-Wesley, Massachusetts, 1969).

[2] J. J. Sakurai, *Advanced Quantum Mechanics* (Addison-Wesley, New York, 1967).

[3] *International Tables for X-ray Crystallography*, 2nd ed., edited by C. H. MacGillavry and G. D. Rieck (Reidel, Dordrecht, 1983), Vol. III,

[4] N. Ashcroft and N. D. Mermin, *Solid State Physics* (Saunders, Philadelphia, 1976).

[5] I. K. Robinson, in *Handbook on Synchrotron Radiation*, Vol. 3, ed. by G. Brown and D. E. Moncton, (Elsevier, Amsterdam, 1991), Chap. "Surface Crystallography".

[6] I.K. Robinson and D.J. Tweet, Rep. Prog. Phys. **55**, 599 (1992).

[7] I.K. Robinson, Phys. Rev. B **33**, 3830 (1986)

[8] R. Feidenhans'l, Surf. Sci. Rep. **10**, 105 (1989).

[9] H. Hong, R. D. Aburano, K.-S. Chung, D.-S. Lin, E. S. Hirschorn, and T. C. Chiang, J. Appl. Phys. **79**, 6858 (1996).

[10] Yong Song Chu, Ph. D. thesis, University of Illinois at Urbana-Champaign (1997).

[11] A. Zangwill, *Physics at Surfaces* (Cambridge University Press, Cambridge, 1988).

[12] A. Ourmazd and J.C. Bean, Phys. Rev. Lett. **55**, 765 (1985).

[13] D. J. Lockwood, K. Rajan, E. W. Fenton, J. M. Baribeau, and M. W. Denhoff, Solid State Commun. **61**, 465 (1987).

[14] E. Müller, H.U. Nissen, M. Ospelt, and H. von Känel, Phys. Rev. Lett. **63**, 1819 (1989).

[15] J. E. Bernard, L. G. Ferreira, S.-H. Wei, and A. Zunger, Phys. Rev. B **38**, 6338 (1988); J. E. Bernard, R. G. Dandrea, L. G. Ferreira, S. Froyen, S.-H. Wei, and A. Zunger, Appl. Phys. Lett. **56**, 731 (1990).

[16] J. E. Bernard, S. Froyen, and A. Zunger, Phys. Rev. B **44**, 11178 (1991).

[17] S. Froyen and A. Zunger, Phys. Rev. B **53**, 4570 (1996).

[18] José Luis Martins and Alex Zunger, Phys. Rev. Lett. **56**, 1400 (1986).

[19] M. Hansen, *Constitution of Binary Alloys* (McGraw-Hill, New York, 1958), 2nd ed.

[20] B. Koiller and M. O. Robbins, Phys. Rev. B **40**, 12554 (1989).

[21] D.E. Jesson, S. J. Pennycook, J.-M. Baribeau, and D.C. Houghton, Phys. Rev. Lett. **68**, 2062 (1992).

[22] J.Z. Tischler, J.D. Budai, D.E. Jesson, G. Eres, P. Zschack, J.M. Baribeau and D.C. Houghton, Phys. Rev. B **51**, 10947 (1995).

[23] F.K. LeGoues, R.M. Tromp, V.P. Kesan, and J. Tsang, Phys. Rev. B **47**, 10012 (1993).

[24] T. Araki, N. Fujimura, T. Ito, A. Wakahara, and A. Sasaki, J. Appl. Phys. **80**, 3804 (1996).

[25] J. C. Tsang, V.P. Kesan, J. L. Freeouf, F.K. LeGoues, and S.S. Iyer, Phys. Rev. B **46** 6907 (1992).

[26] F.K. LeGoues, V.P. Kesan, S.S. Iyer, J. Tersoff, and R.M. Tromp, Phys. Rev. Lett. **64**, 2038 (1990); V.P. Kesan, F.K. LeGoues, and S.S. Iyer, Phys. Rev. B **46**, 1576 (1992).

[27] D.E. Jesson, S.J. Pennycook, J.Z. Tischler, J.D. Budai, J.M. Baribeau and D.C. Houghton, Phys. Rev. Lett. **70**, 2293 (1993).

[28] P.C. Kelires and J. Tersoff, Phys. Rev. Lett. **63**, 1164 (1989).

[29] R. Rossman, H. L. Meyerheim, V. Jahns, J. Wever, W. Moritz, D. Wolf, D. Dornisch, and H. Schulz, Surf. Sci. **279**, 199 (1992);

[30] X. Torrelles, H. A. van der Vegt, V. H. Etgens, P. Fajardo, J. Alvarez, and S. Ferrer, Surf. Sci. **364**, 242 (1996).

[31] M. Takahashi, S. Nakatani, Y. Ito, T. Takahashi, X. W. Zhang, and M. Ando, Surf. Sci. Lett. **338** L846, (1995).

[32] R. Felici, I. K. Robinson, C. Ottaviani, P. Imperatori, P. Eng, and P. Perfetti, Surf. Sci. **375**, 55 (1997).

[33] A. J. Hoeven, J. M. Lenssinck, D. Dijkkamp, E. J. van Loenen, and J. Dieleman, Phys. Rev. Lett. **63**, 1830 (1989).

[34] D.E. Jesson, S.J. Pennycook, and J.M. Baribeau, Phys. Rev. Lett. **66**, 750 (1991).

[35] Suresh C. Jain, *Germanium - Silicon Strained Layers and Heterostructures* (Academic, Boston, 1994), Supplement 24 of series Advances in Electronics and Electron Physics.

[36] F.K. LeGoues, J. Tersoff, and R.M. Tromp, Phys. Rev. Lett. **71**, 3736 (1993).

[37] F.K. LeGoues, V.P. Kesan, and S.S. Iyer, Phys. Rev. Lett. **64**, 40 (1990).

[38] J. S. G. Taylor, C. Norris, E. Vlieg, M. Lohmeier, and T. S. Turner, Rev. Sci. Instrum. **67**, 2658, (1996).

[39] M. Lohmeier and E. Vlieg, J. Appl. Crystallogr. **26**, 706, (1993).

[40] I. K. Robinson, Rev. Sci. Instrum. **60**, 1541 (1989).

[41] D. Abernathy, Ph. D. thesis, Massachusetts Institute of Technology, 1995.

[42] C. Schamper, H. L. Meyerheim, and W. Moritz, J. Appl. Crystallogr. **26**, 687, (1993).

[43] H. Reichert, P.J. Eng, H. Dosch, and I.K. Robinson, Phys. Rev. Lett. **74**, 2006 (1995); A. P. Baddorf and S. S. Chandavarker, Physica B **221**, 141 (1996).

[44] X. J. Zhang, G. Xue, A. Agarwal, R. Tsu, M.-A. Hasan, J. E. Greene, and A. Rockett, J. Vac. Sci. Technol. A **11** 2553 (1993).

[45] J. E. Van Nostrand, Ph. D. thesis, University of Illinois at Urbana-Champaign (1996).

[46] J. E. Van Nostrand, S. J. Chey, M.-A. Hasan, D. G. Cahill, and J. E. Greene, Phys. Rev. Lett. **74**, 1127 (1995).

[47] D. G. Cahill, private communication.

[48] S. Ferrer, X. Torrelles, V. H. Etgens, H. A. van der Vegt, and P. Fajardo, Phys. Rev. Lett. **75** 1771, (1995).

[49] P. M. J. Marée, J. C. Barbour, J. F. van der Veen, K. L. Kavanagh, C. W. Bulle-Lieuwma, and M. P. A. Viegers, J. Appl. Phys. **62**, 4413 (1987)

[50] E. P. Kvam and R. Hull, J. Appl. Phys. **73**, 7407 (1993)

[51] K. Eberl and W. Wegscheider, in *Handbook on Semiconductors* (Elsevier, Amsterdam, 1994), Chap. 8, "Si/Ge and Si/SiGe Heterostructures and Superlattices."

[52] J. E. Van Nostrand, D. G. Cahill, I. Potrov, and J. E. Greene, J. Appl. Phys. to be submitted (1997).

[53] C.A. Dimitriades, J.H. Werner, S. Logothetidis, M. Stutzmann, J. Weber, and R. Nesper, J. Appl. Phys. **68**, 1726 (1990); C. Giannini, S. Lagomarsino, F. Scarinci, and P. Castrucci, Phys. Rev. B **45**, 8822 (1992).

[54] N.E. Christensen, Phys. Rev. B **42**, 7148 (1990).

[55] N. Onda, J. Henz, E. Müller, K.A. Mäder, and H. von Känel, Appl. Surf. Sci. **56-58**, 421 (1992).

[56] H. von Känel, K. A. Mäder, E. Müller, N. Onda, and H. Sirringhaus, Phys. Rev. B **45**, 13807 (1992).

[57] U. Kafader, C. Pirri, P. Wetzel and G. Gewinner, Appl. Surf. Sci. **64**, 297 (1993); U. Kafader, M. H. Tuilier, C. Pirri, P. Wetzel, G. Gewinner, D. Bolmont, and O. Heckmann, Europhys. Lett. **22**, 529 (1993).

[58] N.Onda, H. Sirringhaus, S. Goncalves-Conto, C. Schwarz, E. Müller-Gubler, and H. von Känel, in *Evolution of Surface and Thin Film Microstructure*, edited by H. A. Atwater, E. Chasen, M. Grabow, and M. Lagally, MRS Symposia Proceedings No. 280 (Material Research Society, Pittsburgh 1993), p. 581.

[59] H. Sirringhaus, N. Onda, E. Müller-Gubler, P. Müller, R. Stalder, and H. von Känel, Phys. Rev. B **47**, 10567 (1993).

[60] O. Kubaschewski, *Iron - Binary Phase Diagrams* (Spring-Verlag, Berlin, 1982).

[61] G. A. Prinz, Phys. Rev. Lett. **54**, 1051(1985).

[62] J. Chevrier, P. Stocker, Le Thanh Vinh, J. M. Gay, and J. Derrien, Europhys. Lett. **22**, 449 (1993).

[63] M. Sauvage-Simkin, N. Jedrecy, A. Waldhauer, and R. Pinchaux, Physica B **194**, 48 (1994).

[64] J. Derrien, J. Chevrier, Le Thanh Vinh, I. Berbezier, G. Giannini, and S. Lagomarsino, App. Surf. Sci. **73**, 90 (1993).

[65] M. Sauvage-Simkin, N. Jedrecy, A. Waldhauer, R. Pinchaux, Physica B **198**, 48 (1994).

[66] A. Mascaraque, J. Avila, C. Teodorescu, M. C. Asensio, and E. G. Michel, Phys. Rev. B **55**, 7315 (1997).

[67] N. Onda, H. Sirringhaus, E. Müller and H. von Känel, J. Cryst. Growth **127**, 634 (1993).

[68] M. Fanciulli and H. von Känel, private communication.

[69] H. von Känel (unpublished).

[70] K. A. Mäder, H. von Känel, and A. Baldereschi, Phys. Rev. B **48**, 4364 (1993).

[71] W. B. Pearson, *A Handbook of Lattice Spacings and Structures of Metals and Alloys* (Pergamon Press, New York, 1967), Vol. 2.

[72] P.F. Miceli, C. J. Palmstrom, and K. W. Moyers, Appl. Phys. Lett. **61**, 2060 (1992); P. F. Miceli, in *Semiconductor Interfaces, Microstructure, and Devices: Properties and Applications*, edited by Z. C. Feng (Hilger, Bristol, 1992).

[73] M. Fanciulli, C. Rosenblad, G. Weyer, H. von Känel, and N. Onda, Thin Solid Films **275**, 8 (1996).

[74] C. Pirri, M. H. Tuilier, P. Wetzel, S. Hong, D. Bolmont, G. Gewinner, R. Cortes, O. Heckmann, and H . von Känel, Phys. Rev. B **51**, 2302 (1995).

[75] J. R. Smith, Jr. and A. Zangwill, Phys. Rev. Lett. **76**, 2097 (1996).

Vita

Kevin Lloyd Whiteaker was born June 24th, 1969 in Madison, Wisconsin to the parents Gary and Kathleen Whiteaker. He graduated from McNary High School in Keizer, Oregon on May 29, 1987. Next, Kevin attend for four years Oregon State University in Corvallis, Oregon. While there, he was a summer (1989) intern at the Albany Research Center, in Albany, Oregon, one of U.S. Bureau of Mines materials research laboratories (but now with Department of Energy). Kevin was an invited participant at 6th Summer Institute in Applied Physics at Lawrence Livermore National Laboratory, Livermore, California in August 1990. On June 8th 1991, he graduated with a Bachelors of Science in Physics and with the awards of Graduating with Highest Scholarship and completion of the University Honors Program. Kevin worked with Professor William Hetherington, his honors advisor, in a non-linear optics laboratory. His honors thesis was titled *Laser studies of adsorption on cooled silicon surfaces.*

Next, Kevin Whiteaker attended the University of Illinois at Urbana-Champaign as a graduate student within the Department of Physics. From August 1991 to May 1992, his was a graduate teaching assistant for lab and discussion sections of introductory physics courses. On January 1993, Kevin received the Masters of Science in physics from the University of Illinois. Since June 1992, Kevin has been a graduate research assistant for Professor Ian K. Robinson within the Materials Research Laboratory studying surface science, x-ray diffraction, and molecular beam epitaxy of materials. Also during this time, Kevin was award a Graduate Assistance in the Area of National Need (GAANN) fellowship from the

Department of Physics for January 1994 to May 1996. Mr. Whiteaker's work with Prof. Robinson has been on many experiments and projects, include experiments at the National Synchrotron Light Source, Brookhaven National Laboratory, New York. A list of published articles and papers presented at conferences is listed below.

Publications

I. K. Robinson, K. L. Whiteaker, and D. Walko, Cu island growth on Cu(110), Proc. of the Fourth International Conference on Surface X-ray and Neutron Scattering. Physica B, vol. 221, pg. 70 (1996).

K. L. Whiteaker, I. K. Robinson, C. Benson, D. M. Smilgies, N. Onda, and H. von Kanel, Disordered structure of cubic iron silicide films on Si(111), Physical Review B, vol. 54, no. 15, pg. 9715, April 15 (1995).

I. K. Robinson, K. L. Whiteaker, and R. Schuster, Scaling of island distributions during growth of Cu on Cu(110), National Synchrotron Light Source, Activity Report, BNL 52455, pg. B-104 (1994).

Conferences

K. L. Whiteaker, I. K. Robinson, J. E. Van Nostrand, D. G. Cahill, Atomic ordering of SiGe within 2x1 surface reconstruction, Bull. Amer. Phys. Soc., vol. 42, no. 1, (Kansas City, MO, March 17-21, 1997).

K. L. Whiteaker, I. K. Robinson, C. Benson, D. M. Smilgies, N. Onda, and H. von Kanel, Vacancy disorder in cubic FexSi thin films on Si(111), Fourth International Conference on Surface X-ray and Neutron Scattering (Lake Geneva, WI, June 25-30, 1995).

I. K. Robinson, K. L. Whiteaker, and D. Walko, Cu island growth on Cu(110), Fourth International Conference on Surface X-ray and Neutron Scattering (Lake Geneva, WI, June 25-30, 1995).

I. K. Robinson, K. L. Whiteaker, R. Schuster, Island Distribution Scaling during growth of Cu/Cu(110), Bull. Amer. Phys. Soc., vol. 40, no. 1, pg. 601 (San Jose, CA, March 20-24, 1995).

K. L. Whiteaker, I. K. Robinson, C. Benson, D. M. Smilgies, N. Onda, and H. von Kanel, Disordered structure of cubic iron silicide films on Si(111), Bull. Amer. Phys. Soc., vol. 39, no. 1, (Pittsburgh, PA, March 21-25, 1994)